Development of an Automated Microfluidic System for the Loading and Unloading of Cryoprotectants from Mammalian Oocytes

by

Raphael Matan Zonis

B.Eng., McGill University (2018)

Submitted to the Department of Mechanical Engineering
in partial fulfillment of the requirements for the degree of

Master's of Science in Mechanical Engineering

at the

MASSACHUSETTS INSTITUTE OF TECHNOLOGY

May 2020

Author .....
Department of Mechanical Engineering
May 15, 2020

Certified by .....
Linda Griffith
School of Engineering Professor of Teaching Innovation, Biological Engineering, and Mechanical Engineering
Thesis Supervisor

Certified by .....
Scott Manalis
Professor of Biological and Mechanical Engineering
Associate Head, Department of Biological Engineering
Thesis Supervisor

Accepted by .....
Nicolas Hadjiconstantinou
Chair, Graduate Program Committee

Development of an Automated Microfluidic System for the Loading and Unloading of Cryoprotectants from Mammalian Oocytes

by
Raphael Matan Zonis

Submitted to the Department of Mechanical Engineering
on May 15, 2020, in partial fulfillment of the
requirements for the degree of
Master's of Science in Mechanical Engineering

Abstract

Oocyte cryopreservation is an assistive reproductive procedure that has allowed women to overcome infertility and enjoy increased reproductive freedom. Despite a rapid increase in oocyte cryopreservation cycles over the past seven years, success rates both between and within clinics remain highly heterogeneous, negatively impacting clinical outcomes. This is because the clinical gold standard in oocyte cryopreservation, manual vitrification, is a technically challenging procedure that's success is strongly dependent on the experience, training, and attentiveness of the operator.

In this thesis, the development of an automated platform for the introduction and removal of cryoprotective agents (CPAs) to and from the oocyte is described. By combining microfluidics, automation, and optical measurement systems, the proposed system aims to overcome the challenges inherent to manual vitrification, and improve upon other existing platforms designed to perform these tasks. Development and fabrication of the microfluidic component of this proposed system is described, and is validated through a proof-of-concept experiment. This work marks the first step towards a completely automated vitrification platform, capable of removing the uncertainty in success currently plaguing clinics and their patients.

Thesis Supervisor: Linda Griffith
Title: School of Engineering Professor of Teaching Innovation, Biological Engineering, and Mechanical Engineering

Thesis Supervisor: Scott Manalis
Title: Professor of Biological and Mechanical Engineering
Associate Head, Department of Biological Engineering

Acknowledgments

I would like to thank both my wonderful supervisors, Professors Linda Griffith and Scott Manalis, for providing the personal and academic guidance that I needed to succeed in this degree. Their input was invaluable in the advancement of this project and the writing of this thesis. I would also like to thank Joseph O'Brien Doyle and his wife, Nicole Doyle, for generously providing funding for me to contribute to this exciting and important work, and helping me understand the basics of oocyte vitrification. Thank you to Duncan Allison O'Boyle, Pierre S.Phabmixay, Victor Hernandez-Gordillo, Marianna Sofman, and the rest of the Griffith lab for providing crucial materials, expertise, and camaraderie over the course of my Master's thesis. Thank you to Max Stockslager for being a valuable member of the oocyte vitrification team. Thank you Prof. Nicholas Fang for providing me access to his lab and the UV DLP setup that was used for the fabrication of hydrogel microwindows, and thank you to Xinhao Li for teaching me how to operate this setup, and for helping me with these experiments over the course of my thesis. Thank you to Prof. Paula Hammond for loaning me much needed syringe pumps for this project.

Thank you to my sister, brother, father, mother, and girlfriend for loving and supporting me throughout the course of my Master's thesis. Thank you to the friends that I have made over the course of my time in Boston/Cambridge for helping make this new city feel like a home. Thank you to my old friends from Montreal and New Jersey for being a constant source of support, and helping remind me of who I am and where I come from.

Contents

List of Figures

List of Tables

Chapter 1

Introduction: The current state of oocyte vitrification

1.1 Oocyte vitrification: a historical and social perspective

Oocyte vitrification is one of a suite of services offered to women and couples within the field of assisted reproductive technologies (ART). According to the Centers for Disease Control website, ART is defined as "all fertility treatments in which either eggs or embryos are handled" [1]. Prior to the advent of oocyte vitrification, ART had offered women and couples a variety of services aimed at overcoming the challenges involved in conceiving a child. One of the first of these technologies, known as in-vitro fertilization (IVF), was achieved in 1978 by the team of Robert Edwards and Patrick Steptoe [2]. IVF, as its name denotes, allowed for fertilization to occur outside the body, permitting thousands of couples suffering from infertility to conceive a child. Today, IVF, along with its more recent counterpart intracytoplasmic sperm injection (ICSI), remain cornerstones of ART, and are commonly used in conjunction with oocyte vitrification and other ART services.

Long term storage of cells was soon after shown possible by Alan Trouson and Linda Mohr with the successful cryopreservation, warming and reimplantation of the first human embryo in 1983 [3]. This, along with prior advancements in the cryopreservation of sperm [4], the advent of embryo donation [5], and the increased number of sperm banks and sperm donors throughout the 1970s and 1980s, completely revolutionized the landscape of reproductive medicine. The conspicuous missing item from this list of expanding reproductive technologies is the ability to safely store, warm, and donate oocytes.

The first birth from a frozen human oocyte occurred in 1986 [6]. The method by which this oocyte was frozen was by a process called "slow freezing", whereby the egg is brought down to below freezing temperatures at defined cooling rates. This method, borrowed directly from embryo cryopreservation, remained the gold standard in cryopreservation for the next 25 years. Vitrification fundamentally differs from slow freezing in that the goal of vitrification is to cool the cell/s to sub-freezing

temperatures as fast as possible. Despite work done since the 1980s validating the potential of vitrification as a viable cryopreservation technique [7], including the first births from vitrified oocytes in 1999 [8, 9], it would not be until the turn of the millennium that the superiority of oocyte vitrification in terms of cost, efficiency, and clinical outcomes would become widely accepted [10–12]. This change in attitude was then codified in 2013 when the American Society for Reproductive Medicine (ASRM) removed the "experimental" label from oocyte vitrification, inviting fertility clinics across the country to add oocyte vitrification to their repertoire of services [13]. This change in attitude by the ASRM has also been accompanied by the rise of commercial oocyte banks in the past decade [14, 15]. This described history of reproductive medicine is summarized in **Figure 1-1**.

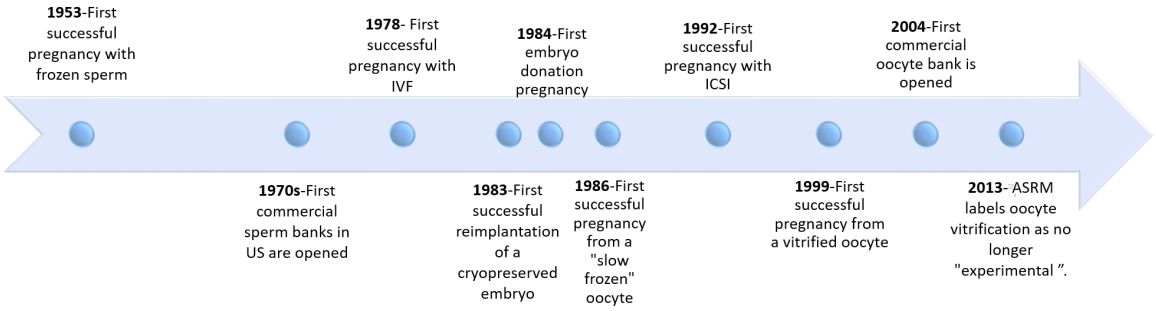

Figure 1-1: A brief history of reproductive medicine [2–6, 8, 9, 13–15].

Today, oocyte vitrification is the most commonly used technique for the cryopreservation of oocytes. This technology has allowed women to take ownership of their reproductive freedom, while circumventing the thorny legal, ethical, and religious controversies linked to embryo cryopreservation and storage [16, 17]. For 20% of patients, oocyte vitrification helps them escape the devastating reproductive consequences of medical indications such as chemotherapy, radiation therapy, invasive gynecological surgeries, and genetic disorders. For a rapidly growing proportion of women, oocyte vitrification has afforded the opportunity to delay childbearing until one is more professionally and financially established [18](a solution, for the record, this author believes is a partial remedy for a much larger, gendered issue in our society that merits more discussion than is currently afforded to it.). This reality has been acknowledged by companies like Facebook, Apple, and Google, who, in the past six years, have added oocyte vitrification to their respective corporate insurance plans [19].[1] The push for oocyte vitrification has been further spurred by the pop up of fertility start ups, such as Prelude and Extended Fertility, that are attempting to "disrupt" the world of reproductive medicine by providing quality ART services at reduced costs. These compounding factors have resulted in a more than doubling

[1]For an interesting conversation on the ethics of corporate subsidies for oocyte cryopreservation (reproductive freedom vs. reproductive coercion) see the discussion at the conclusion of Dr. Ruth Bunker Lathi's talk at the 2018 Open Endoscopy Forum.

of the number of oocyte vitrification cycles performed between 2014 and 2018, the last year for which data is available (**Figure 1-2**). While this marked rise in oocyte vitrification indicates a clear increase in patient demand, the quality of service being provided to these women, as will be elaborated on in the coming section, leaves much to be desired.

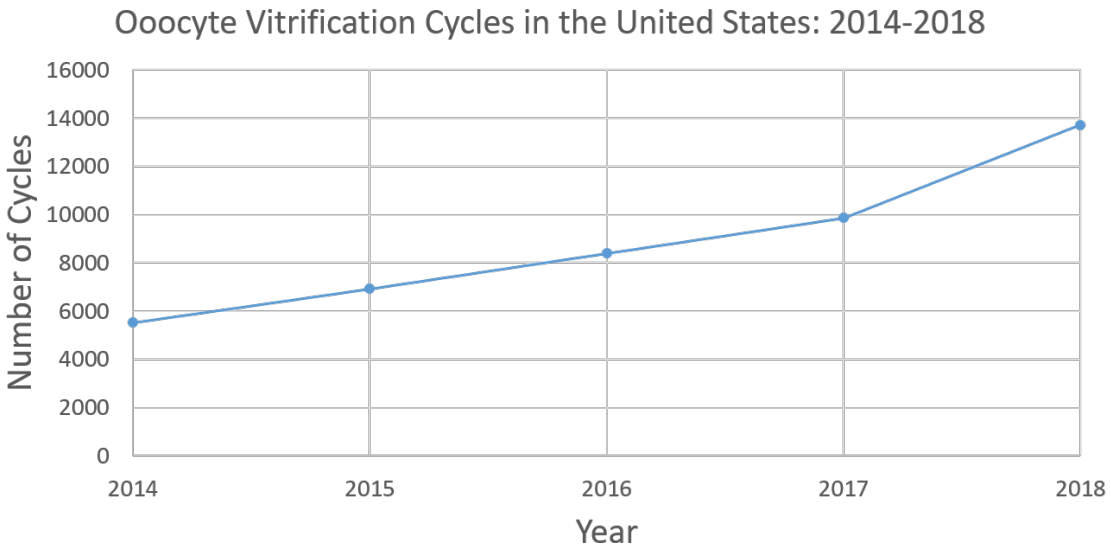

Figure 1-2: Rise in oocyte vitrification cycles over time in the United States. Data was collected from the five most recent Society of Assisted Reproductive Technology's (SART) "National Summary Report[s]", filtering to "Include Only" "Frozen egg" cycles [20].

1.2 Manual vitrification and its clinical challenges

Manual vitrification, as it's name denotes, is vitrification performed by a manual operator. This manual operator is usually a clinician or medical technician. While there exists a variety of manual vitrification protocols and kits [21–23], each containing their own proprietary equipment, instructions, and solutions, all vitrification protocols share a common set of steps. These steps, in order of occurrence, are cryoprotectant (CPA) loading, cooling and storage, warming, and CPA unloading. To better understand the technical challenges of manual vitrification, the manual manipulations and time frames involved in each step of the vitrification process must be described. The author has chosen to use the Cryotop method as this representative example because of its excellent, publicly available documentation and its widespread use across the clinical world [24].

It should be noted that, prior to vitrification, oocytes are retrieved from a patient's ovaries. From this set of oocytes, only oocytes that have reached the metaphase II

(MII) stage of meiosis are selected to proceed to vitrification.[2] These oocytes may or may not be denuded of cumulus cells through the use of hyaluronidase, depending on the protocol and clinical conventions [27]. Oocytes are then placed in culture medium in preparation for cryopreservation.

Cryotop oocyte cryopreservation protocol

Materials

- **Repro plate**-polystyrene plate with six wells for storage of solutions (**Figure 1-3a**)
- **Basic solution (BS)**
- **Equilibration solution (ES)**
- **Vitrification solution (VS)**
- **Thawing solution (TS)**
- **Diluent solution (DS)**
- **Washing solution (WS)**
- **Pasteur pipette**
- **Cryotop sheet**-thin (100 microns thick, 700 microns wide) polypropylene cantilever, with thick plastic attachment, used for handling the oocyte outside of solution (**Figure 1-3b**) [28].
- **Stereomicroscope**
- **Tweezers**
- **Stopwatch/Timer**-to be used for all steps involving timing
- **Liquid nitrogen**
- **Micropipette**

CPA Loading Protocol

1. Pipette 20 microliters of BS into one well of the repro plate, and 300 microliter of VS into two separate wells of the repro plate respectively. These two wells will then be arbitrarily denoted as VS1 and VS2 respectively.

[2]Traditionally, this has been done because of the challenges in performing in vitro maturation (IVM) [25]. However, in Februrary 2020, a new milestone in ART was achieved when the first child from an IVM matured oocyte (followed by vitrification) was born [26]. Thus, in the foreseeable future, it is possible that immature oocytes traditionally discarded prior to vitrification can in fact be used, further improving patients' chances of conceiving a child and reducing their financial burden.

(a) Repro plate from Cryotop protocol

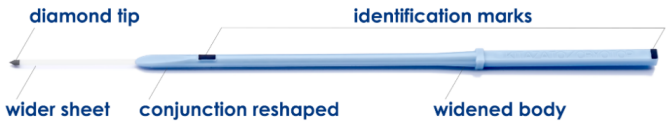

(b) Cryotop sheet from Cryotop protocol. The width of the tip is 700 microns, and its thickness is 100 microns [28].

Figure 1-3: Images of materials used in the Cryotop vitrification protocol.

2. Using the pasteur pipette, remove oocyte residing in culture medium and deposit it in the bottom of the BS well. Be sure to blow out from the pipette so that the oocyte resides at the pipette tip. Bring the oocyte into focus on the stereomicroscope.

3. Gently add 20 microliters of ES to the top of the BS. Leave for 3 minutes.

4. Repeat the previous step.

5. Add 240 microliters of ES gently to the top of the BS and leave for 6-9 minutes. Completion of this step is marked when the width of the perivitelline space (space between the oocyte and the zona pellucida) becomes equal to the width prior to immersion in ES.

6. Remove the oocyte from the BS/ES mixture, and blow out until the oocyte resides at the pipette tip. Place oocyte at the center of VSl. Make sure to blow out only enough such that the oocyte enters VS1 with a minimal volume of accompanying ES. Bring the oocyte into focus on the stereomicroscope.

7. Blow out the ES remaining in the pipette outside VS1. Fill the pipette with VS and blow out outside VS1 to wash the pipette.

8. Fill the pipette with VS. Suck the oocyte into the tip of the pipette. Blow the oocyte out to a new location in VS1. Use the pasteur pipette to quickly stir five times around the oocyte.

9. Repeat the previous step two additional times. Note that this step and the previous step are to be completed within 30 seconds. Also note that, as the position of the oocyte changes, the focus of the stereomicroscope must also change.

10. Blow the VS out of the pipette. Aspirate the pipette with VS from VS2.

11. Repeat steps 6, 7, and 8, replacing the "BS/ES mixture" with "VS1", and "VS1" with "VS2".

12. Repeat the previous step one more time. This step and the previous step are to be completed within 30 seconds.

13. Aspirate the oocyte from VS2, being sure to blow out enough VS such that the oocyte resides at the pipette tip.

Cooling and Storage Protocol

1. Put the Cryotop sheet in the hand not being used to handle the pasteur pipette. Bring the black mark at the tip of the Cryotop sheet into focus.

2. Carefully blow the oocyte out of the pipette and onto the Cryotop sheet near the black tip, ensuring to refrain from blowing out an excess amount of VS. A maximum of 0.1 microliters of excess volume is recommended.

3. Aspirate any excess VS using the pasteur pipette.

4. Plunge the Cryotop sheet into a liquid nitrogen tank, being sure to swirl the sheet around in the liquid nitrogen to avoid accumulation of nitrogen vapor around the oocyte.

5. Using tweezers, place a plastic cap on the Cryotop sheet, ensuring that the oocyte does not leave the liquid nitrogen at any point. Twist the cap onto the Cryotop sheet to ensure a tight fit between the two.

6. Without leaving liquid nitrogen, transfer the now vitrified oocyte to a storage tank until the patient wants the oocyte to be warmed.

Warming protocol

1. Place sealed TS vial into a Petri dish. Place the Petri dish into incubator set to 37 °C. Wait at least 90 minutes.

2. Bring DS and WS to room temperature (25 °C– 27 °C).

3. Pipette 300 microliters of DS into one well of the repro plate, and 300 microliters of WS into two separate wells of the repro plate respectively. These wells will be arbitrarily named WS1 and WS2 respectively.

4. Bring the Cryotop sheets with the patient's oocyte on them near the stereomicroscope. Note that at no point should the oocyte leave the liquid nitrogen.

5. Remove the Petri dish with TS vial from the incubator. Empty the contents of the vial into the Petri dish and place near the stereomicroscope.

6. Adjust the focus of the steromicroscope to the Petri dish with TS.

7. Carefully untwist and remove the plastic cap placed on the Cryotop sheet, while leaving the oocyte in liquid nitrogen.

8. Quickly remove the Cryotop sheet from liquid nitrogen and submerge it in the TS Petri dish. The recommended time limit for this step is one second.

9. Quickly bring the oocyte into focus on the stereomicroscope.

10. One minute from the time the oocyte was submerged in TS, aspirate the oocyte into the pasteur pipette, being sure to aspirate enough TS such that the oocyte resides 2 mm from the tip of the pipette.

CPA unloading protocol

1. Gently blow out the TS and oocyte from the pasteur pipette into the bottom of the DS well. Wait three minutes.

2. Aspirate the oocyte into the pasteur pipette, as well as enough DS such that the oocyte resides 2 mm from the pipette tip.

3. Blow out the DS and oocyte from the pipette into the bottom of WS1. Wait five minutes.

4. Aspirate the oocyte into the pasteur pipette with minimum residual WS. The oocyte should be positioned at the tip of the pipette.

5. Blow out the oocyte onto the top center of WS2. Once the oocyte falls, aspirate the oocyte from the bottom of WS2 and repeat this process once more.

6. Transfer the oocyte to a culture dish containing the appropriate culture medium. Place the culture dish in an incubator at 37 °C for at least two hours in preparation for fertilization.

The above protocol is summarized in **Figure 1-4**. The author also recommends reviewing the following protocol animation provided by Cryotop, if the reader is confused about any of the protocol's steps.

From a description of this protocol, it is clear that the success of manual vitrification relies heavily on operators' subjective judgment (evaluation of the perivitelline space), technical experience, and training (performing many, delicate, time constrained oocyte manipulations while adjusting the microscope focus). Operator fatigue is also a major factor determining whether a given vitrification cycle will be successful. The influence of all these factors then get amplified when one considers that an operator is seldom vitrifying only one egg at a time. The most able technicians are expected to vitrify one cycle of patient oocytes (~10-15 oocytes) in a span of 30 minutes. This means that they are performing the above protocol with multiple oocytes at once; for the Cryotop protocol specifically, a single Cryotop sheet can accommodate a maximum of four oocytes at once [24].

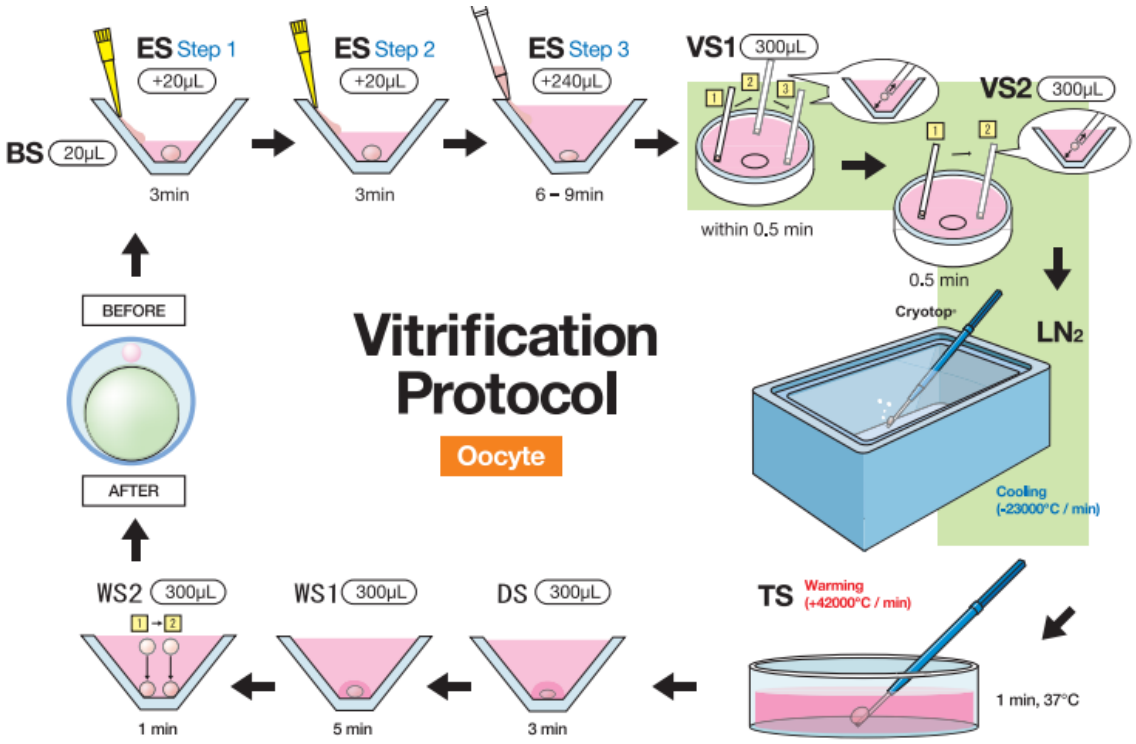

Figure 1-4: Summary of the Cryotop oocyte cryopreservation protocol. The figure was taken from the document entitled "Vitrification protocol" available at [24].

The consequence of these technical challenges, coupled with the lack of a standardized protocol, is a large heterogeneity in clinical outcomes for patients wishing to vitrify their oocytes. For oocyte vitrification, the success of a given cycle is measured by the "post-warm survival rate", which is the ratio of viable oocytes after warming to the total number of oocytes vitrified. It should be noted that viability is measured after warming, and not during storage, because clinicians are currently unable to evaluate an oocyte's viability while it is in a vitrified state. This means that a patient does not know whether the oocytes they have vitrified are viable until they wish to use them, at which point they may no longer be able to produce healthy oocytes. The magnitude of the heterogeneity can be observed by acknowledging that the most successful vitrification cycles are reported to have post warm survival rates of >85% [29, 30]. Compare this to [31], which describes the individuals involved in cryopreserving and warming a 36-year old patient's oocytes, and the ultimate success of this process. The results are summarized in **Table 1.1**. Note that warming of all oocytes was performed by the same embryologist.

The patient was 43 at the time of oocyte warming, and was ultimately not able to achieve pregnancy. The reason why this is the case, despite having 24 viable oocytes after warming, is because of the steps that follow oocyte warming in the process of achieving pregnancy. Fertilization, blastulation, and implantation all must occur in order to convert a warmed oocyte into a clinical pregnancy. The probability of achieving at least one birth for a given number of vitrified MII oocytes, categorized

Table 1.1: Summary of vitrification success for [31]. Note that warming of all oocytes was performed by the same embryologist.

Operator	**Experience Level**	**Number of oocytes vitrified**	**Number of oocytes that survived following warming**	**Post warm survival rate**
Embryologist A	senior	14	10	71.4%
Embryologist B	senior	12	2	16.7%
Embryologist C	junior	17	12	70.5%
Total		**43**	**24**	**55.8%**

by age at which oocytes were retrieved from the ovaries, is shown in **Figure 1-5** [32].

It should be noted that a single vitrification cycle, as verified in **Table 1.1**, yields ~10-15 MII oocytes, a number that decreases slightly with age. Thus, for a single vitrification cycle, it is not guaranteed that a woman of any age will produce enough MII oocytes to eventually become pregnant, with the chance of pregnancy decreasing with age at the time of retrieval. It is for this reason, as was done with the previously described patient, that it is advised that patients undergo multiple vitrification cycles in order to increase their chances of pregnancy. These cycles, between hormonal treatments, ultrasounds for ovarian stimulation, oocyte retrieval, and oocyte vitrification, generally cost a patient $10,000-$15,000 per cycle [33]. Patients must also pay storage costs amounting to $275-$1000 per year. As oocyte cryopreservation is often deemed an elective procedure (except in certain cases where there is a medical indication), these costs are usually paid 100% out of pocket.[3]

To summarize, the success of the manual vitrification process depends heavily on the experience, training, and attentiveness of the operator. This inevitably leads to errors being made in the vitrification process, which adversely impacts vitrification success. These errors translate to an increased financial burden on patients and heterogeneous clinical outcomes that can take an incalculable emotional toll on patients who had dreams of bearing a child. **The goal of this project is to ameliorate these problems by creating a fully automated vitrification system that simultaneously standardizes the protocol for vitrification and removes inter-operator variability**.

[3]For a distressing article that discusses the irony of how the medical professionals trained to provide services in assisted reproduction often cannot, during their peak reproductive years, afford the out of pocket expenses these procedures incur, read [34].

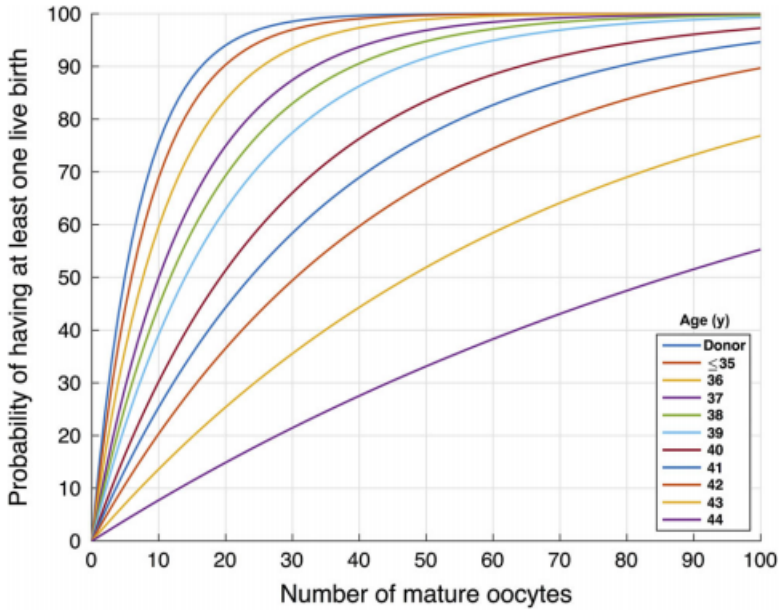

Figure 1-5: Probability of achieving at least one birth for a given number of vitrified MII oocytes, categorized by age at which oocytes were retrieved from the ovaries [32].

1.3 Ideal clinical system

In order to effectively design a solution for the problems described in the previous section, it is important that an ideal clinical system is defined. This ideal clinical system cannot simply resolve the issues inherent to manual vitrification, but must do so in a way that makes it seamlessly integratable into the current clinical workflow. With these considerations in mind, the ideal clinical system is defined as a system that is:

- **Comprehensive**-handles all steps from the introduction of a fresh oocyte to the delivery of a ready-to-fertilize warmed oocyte
- **Easy to operate**-requires minimal technical experience to run and troubleshoot
- **High fidelity**-all patient oocytes must be successfully recovered for fertilization. To ensure this, the platform must produce consistent, repeatable results across many vitrification cycles.
- **High throughput**-processing time per vitrification cycle should be as fast, or faster, than through manual methods. This means that the system must process one vitrification cycle's worth of oocytes every 30 minutes.
- **Space efficient**-the system must be compact enough to fit in a conventional clinic. Additionally, vitrified oocytes must be able to be stored individually and compactly for long (>10 years) periods.

1.4 Theory of cryopreservation

1.4.1 Intracellular ice formation (IIF) and the role of CPAs

Vitrification is defined as increasing an amorphous (molecularly disordered) material's viscosity to a value below 10^{13} Poise through rapid cooling [35]. In the case of an oocyte, this "substance" is an aqueous suspension of proteins and organelles. Assuming the properties of this suspension roughly match those of water, this means that, to successfully vitrify an oocyte, one must increase the viscosity of the intracellular suspension by **15 ORDERS OF MAGNITUDE**. For reference, bitumen, considered to be one of the most viscous known liquids, has a viscosity of 2.3×10^9 Poise.

The utility of vitrification is that it allows for biological viability and molecular stability to be maintained for long periods of time [36]. And, while there are some naturally occurring mechanisms that are able to achieve this long term preservation through strategies like drying alone [37, 38], much of the research on the matter has focused on vitrification by rapid cooling. The primary issue in performing vitrification with water and other aqueous solutions is that water is a crystalline solid that freezes, meaning that it changes from a liquid to a molecularly ordered solid at a well-defined temperature. Additionally, water, unlike most materials, expands upon freezing. These two observations lead to the concept of harmful intracellular ice formation (IIF), whereby the conversion of water to ice inside the cell leads to extraordinary changes in the solute concentration within the cell's liquid phase, and mechanical damage to intracellular structures and membranes [35].

To reduce the chances of IIF, researchers conceived the concept of cryoprotective agents, or CPAs [36]. In the context of oocyte cryopreservation, there are two types of CPAs: permeating CPAs (pCPAs) and nonpermeating CPAs (npCPAs). pCPAs are small (MW ~70 Da) molecules that's purpose is to cross the cell membrane and partially disrupt hydrogen bonding between water molecules inside the cell. This disruption of hydrogen bonding increases the mean distance between water molecules, making the formation of ice upon cooling slower and less energetically favorable. This latter effect physically translates to a depression of freezing point (**Figure 1-6**). In order to cross the cell membrane by diffusion, pCPAs are chosen to have no net charge. However, though nonpolar molecules do cross the cell membrane faster than polar ones [39], in order to disrupt hydrogen bonding within the cell, pCPAs need to be highly polar. pCPAs are also chosen for their ability to remain in aqueous solution at ultra low temperatures. Typical pCPAs include dimethyl sulfoxide (DMSO) **Figure 1-7a**, ethylene glycol (EG) **Figure 1-7b**, and propylene glycol (PG) **Figure 1-7c**.

npCPAs are high molecular weight molecules (MW>100 Da) that help control the concentration gradient across the cell membrane. Prior to cooling, these molecules can be used to draw more water out of the cell, which serves to decrease the amount of water that can potentially turn into ice, and to increase the intracellular pCPA concentration. Typical npCPAs include polyethylene glycol (PEG), sucrose, trehalose, and polyvinylpyrrolidone (PVP). This class of molecules is also used during the CPA unloading step of the cryopreservation process (see sec. 1.2) to control the concen-

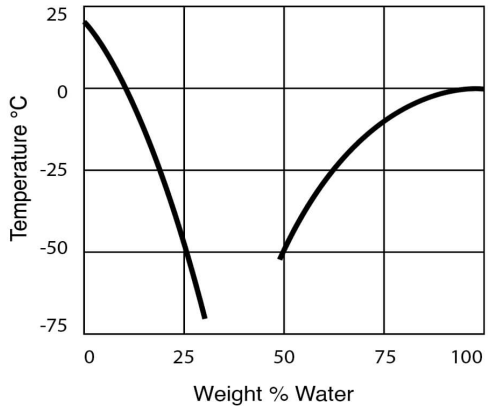

(a) Freezing point depression of DMSO in water [40].

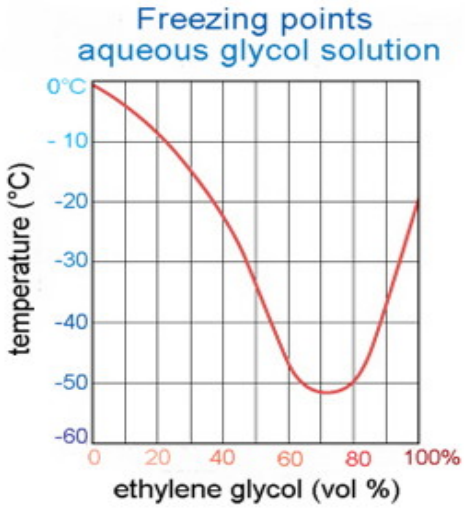

(b) Freezing point depression of EG in water [41].

Figure 1-6: Freezing point depression induced by common pCPAs in aqueous solution.

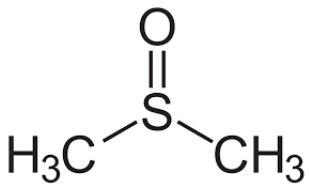

(a) Structural formula of dimethyl sulfoxide (DMSO)

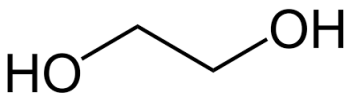

(b) Structural formula of ethylene glycol (EG)

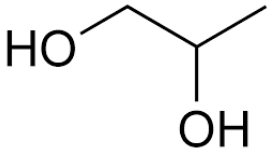

(c) Structural formula of propylene glycol (PG)

Figure 1-7: Structural formulas of common pCPAs. Note the high polarity and small size of each molecule.

tration gradient across the cell membrane.

While CPAs make it easier to avoid IIF, they introduce other problems that can affect cell viability. By dehydrating the cell, npCPAs increase the concentration of not only pCPAs, but also of salts native to the cell. This can drastically alter the intracellular pH, resulting in disruption of protein structure and function. Additionally, pCPAs have been shown to have a variety of toxic effects on cells [42], the severity of which increases with concentration, temperature, and time for which the cell is at biologically relevant temperatures. Thus, balancing the risk of IIF and "CPA effects" is at the heart of the challenge of cryopreservation.

As a point of clarification, oocytes are not exposed directly to CPAs. They are instead exposed to vitrification solutions (see sec. 1.2), which are aqueous mixtures of CPAs and other constituents such as salts, proteins, and antibiotics. The non-CPA portion of the vitrification solution is termed the carrier solution, which is the physiological support medium designed to limit non-CPA related injury to the cell.

1.4.2 Slow freezing vs. vitrification: a theoretical comparison

To understand the importance of rapid cooling (and, as will be explained later, rapid warming) in vitrification, it is instructive to better understand why vitrification has outperformed "slow freezing" (see sec. 1.1) in the context of oocyte cryopreservation. Slow freezing operates on the observation that, because of native intracellular solutes, it is straightforward to design a relatively dilute extracellular CPA solution that will have a higher freezing point than that of the intracellular solution. The idea is to allow a small amount of pCPA to diffuse into the cell initially and then lower the temperature to the point that the extracellular solution will freeze while the intracellular solution will not. This freezing reduces the volume of liquid phase outside the cell, which results in a gradual rise of extracellular CPA concentration. This, in turn, will lead to increased diffusion of pCPAs into the cell and water out of the cell. Then, when the intracellular CPA concentration is deemed optimal, the temperature will be dropped drastically in order to transition the cell into a cryopreserved state. If this drastic temperature drop happens too early, then the risk of IIF will be increased, and if it happens too late, then the risk of deleterious CPA effects will be increased.

Vitrification, on the other hand, does not attempt to strike this perfect balance between these two forms of damage. Instead, it attempts to achieve the fastest possible cooling and warming rates, while using the minimum amount of pCPAs needed to ensure IIF does not occur given these rates. The rationale behind this is that deleterious pCPA effects are inevitable, but they can be mitigated by introducing a smaller amount of pCPAs into the oocyte. The only way this can be achieved without risking IIF is by operating with very high cooling and warming rates. The differences in these two cryopreservation protocols is illustrated in **Figure 1-8**.

There are a few key reasons why vitrification outperforms slow freezing. With regards to IIF and CPA effects, the primary advantage of vitrification is that CPA effects are reduced relative to slow freezing. This conclusion is actually not obvious, and the belief that vitrification protocols required higher intracellular CPA concentrations relative to slow freezing protocols was a major concern of the method for decades [44]. This is because the extracellular solutions for slow freezing had much lower concentrations of pCPA (~1.5 M) than those of used for vitrification (~6 M) [27]. This argument is misleading because, as discussed previously, the extracellular solution becomes more concentrated over the course of the slow freezing protocol as the extracellular liquid phase shrinks. Moreover, it has been shown that CPA loading in vitrification is a process where diffusional equilibrium across the oolemma is not reached (recall the time scales for the final steps of CPA loading from sec. 1.2), with the true intracellular CPA concentration being less than ~33% of the max extracellular pCPA concentration [45].[4] These two observations explain why it has been shown that, for the same cooling and warming rates, oocytes loaded with CPAs using a slow freezing protocol are **LESS LIKELY** to have IIF than oocytes loaded with CPAs

[4]The 33% value accounted for the presence of CPAs and intracellular solutes native to the cell. The contribution of each component was never quantified.

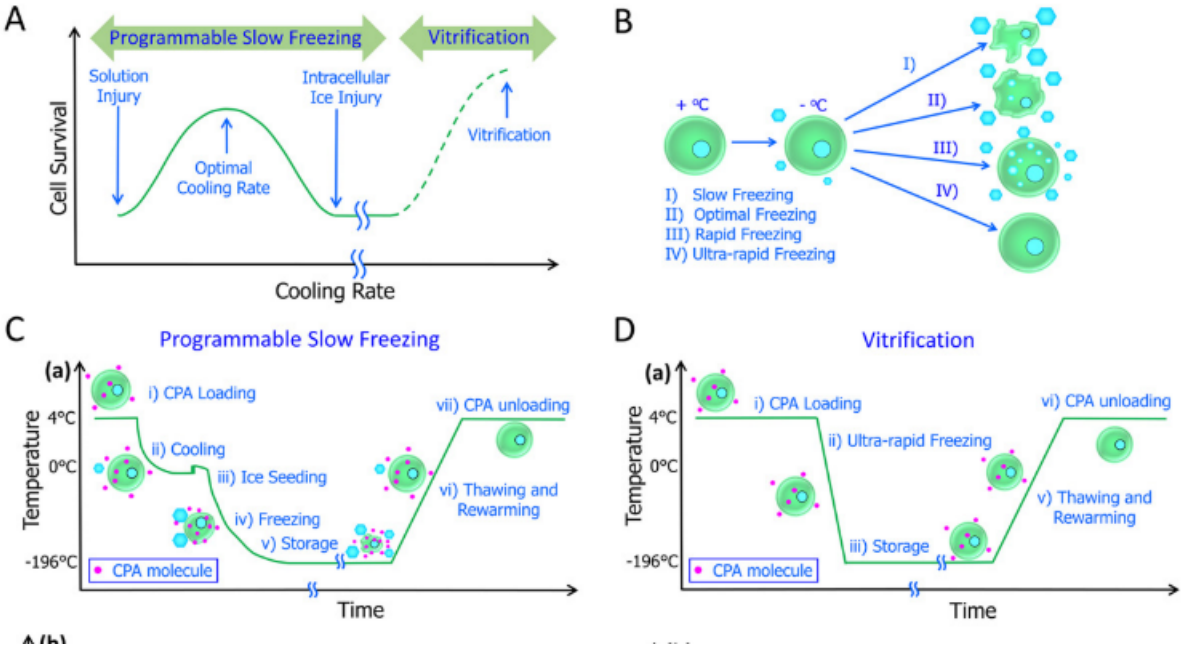

Figure 1-8: Graphical illustrations describing the difference between slow freezing and vitrification protocols. Retrieved from [43]

using a vitrification protocol, indicating that slow freezing protocols actually result in a higher intracellular CPA concentration. Thus, it can be concluded that slow freezing, stripped of all it's precise cooling rates, is simply vitrification with a higher intracellular CPA concentration. As higher CPA concentrations increase toxic effects on the cell, it makes sense that post warm survival using slow freezing is worse than when vitrification is used.

Another important reason, unrelated to CPAs and IIF, why vitrification outperforms slow freezing is because of the oocyte's susceptibility to "chilling injury". Chilling injury is defined as non-IIF related injury caused by holding cells at sub-physiological temperatures. In the case of MII oocytes (see sec. 1.2), this manifests itself in the form of meiotic spindle damage and a reduced ability to recover cellular volume after cryopreservation, which would tend to point to damage to either/both the oolemma and/or zona pellucida [46, 47]. The extent of this damage has been shown to be time dependent, again indicating that the faster an oocyte is cooled, the higher the chance of post-thaw viability.

1.4.3 CPA loading and unloading and osmotic shock

From the discussion of the previous two sections, it is clear that, to mitigate toxic CPA effects, CPAs should be loaded into the oocyte as quickly as possible prior to cooling, and unloaded from the oocyte as quickly as possible following warming. To accomplish this, it seems logical to introduce the oocyte directly into a highly concentrated CPA solution before cooling, and directly into culture medium following warming. However, as water transports across the oolemma much more quickly than

pCPAs, the time scale for equilibration for both water and pCPAs are much different [48]. This disparity in time scales results in a sharp, sudden dip in cell volume when an oocyte is introduced to hypertonic CPA solution, and a sharp, sudden spike in cell volume when an oocyte is introduced to hypotonic CPA solution. In both cases, the cell gradually returns to its approximate initial volume as the concentration of pCPAs equilibrate. However, these sudden, drastic changes in cell volume, termed "osmotic shock", have been shown to cause damage to the meiotic spindle in MII human oocytes [49], negatively impacting the oocyte's developmental competence.

To mitigate osmotic shock in manual vitrification, oocytes are introduced to CPA solutions of increasing concentration during CPA loading, and to CPA solutions of decreasing concentration during CPA unloading. Both processes are performed in a step-wise fashion (see sec 1.2), owing primarily to limitations in the dexterity and skill of a manual operator. To limit the complexity of the vitrification protocol, trial-and-error experimentation has shown that CPAs can be safely loaded and unloaded from the oocyte in two to three steps. While some studies have tried to better characterize this process by establishing "osmotic tolerances", or limits on the allowable volumetric excursions for oocytes, these estimates vary wildly, and can range anywhere from 30%-70% [50]. Part of this divide may be attributed to the fact that studies with lower excursion estimates employ the use of pCPAs [51–53], while those with higher excursion estimates use only npCPAs to control the water content of the oocyte [48]. This tends to suggest that the deleterious effects of CPAs and osmotic shock are inextricably linked and have a negative, compounding effect.

The ideal CPA loading and unloading protocol which minimizes the combined damage of CPA toxicity and osmotic shock is unclear. One school of thought, as alluded to at the beginning of this section, is to create an optimized step-wise CPA loading and unloading protocol which performs the necessary loading and unloading steps in the fastest amount of time while operating within the most conservative estimates for osmotic tolerances [50]. However, recent advances in microfluidics has provided the user unprecedented control over the oocyte's chemical environment, allowing for new loading and unloading protocols that were hitherto not possible. This has enabled the decoupling of the effects of the magnitude and rate of volumetric excursion by replacing step-wise changes in CPA concentration with gradual, continuously changing ones. This work has suggested that while both step-wise and continuous exposure conditions can result in a high post-warm survival rate, step-wise exposure conditions can result in so called "sub-lethal damage", such as decreased cytoplasmic lipid retention, increased damage to the oolemma, increased cytoplasmic leakage, and decreased blastomeres per blastocyst [54]. Though compelling, this work has only been performed on murine oocytes, making its relevance to human oocytes unclear. Moreover, numerous studies have shown that, using manual vitrification, it is possible to achieve similar clinical outcomes using either vitrified oocytes or fresh oocytes, calling into question the importance of this sub-lethal damage in a clinical context [30, 55, 56]. However, as more research into human oocyte cryopreservation is performed, and as the number of children born using oocyte cryopreservation increases, it is possible that this reported sub-lethal damage may result in negative outcomes that are as of now poorly understood.

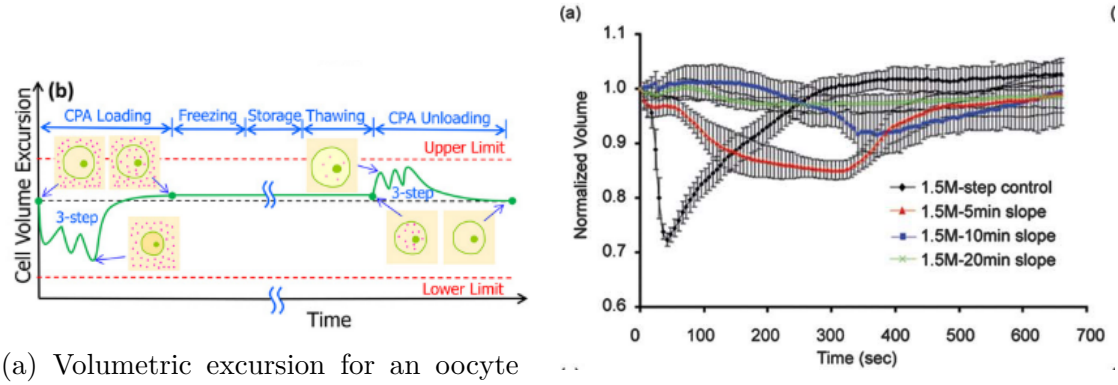

(a) Volumetric excursion for an oocyte throughout a typical vitrification protocol. Note how both CPA loading and CPA unloading are each performed in three steps to ensure volumetric excursions do not exceed the oocyte's osmotic tolerance [43].

(b) Volumetric excursions for linear CPA loading profile achieved using microfluidics. Note how, for a continuously increasing gradient of CPAs, volumetric excursion is minimized relative to a typical stepwise addition [57].

Figure 1-9: Typical volumetric excursions using manual and microfluidic methods.

1.4.4 Rapid cooling and warming rates: How fast is fast enough?

As discussed in the sec. 1.4.2, vitrification attempts to minimize damage to the oocyte via rapid cooling. However, the magnitude of how fast this cooling must occur, and the impact of CPAs on this rate, has yet to be discussed. To try answering this question, it may be useful to examine the critical cooling rates needed to vitrify pure water, and the effect CPAs have on these cooling rates. This data is summarized in **Figure 1-10**. Note that the critical cooling rate is defined as the cooling rate for which less than 0.2 % of the solution mass is turned into ice.[5]

Noting that the concentration of pCPAs in a typical vitrification solution is ~30% w/w-40% w/w [10, 21], and, from sec. 1.4.2, that the true intracellular pCPA concentration prior to cooling is at most ~33% of the max extracellular pCPA concentration, it can be concluded that the true intracellular pCPA concentration prior to cooling is at most ~10% w/w–15% w/w. Approximating the vitrification properties of the oocyte as those of a mixture of pCPAs and water, it can be estimated that the critical cooling rate for oocyte vitrification is on the order of ~10^5 $\frac{^\circ C}{min}$–10^6 $\frac{^\circ C}{min}$. In reality, the actual cooling rates achieved by typical vitrification platforms are on the order of 10^3 $\frac{^\circ C}{min}$–10^4 $\frac{^\circ C}{min}$ (**Figure 1-11**). Thus, it is found that it is actually possible to achieve vitrification in oocytes at cooling rates orders of magnitude below the critical cooling rates predicted by pCPA-water mixture models.

There are a few possible explanations as to why this may be the case. Firstly, pCPAs are only a portion of the of the non-aqueous component of the oocyte cytoplasm.

[5]The convention of choosing 0.2% w/w ice as a standard for defining the critical cooling rate is based in part on the fact that this is the minimum amount of ice that has been considered to be quantifiable by differential scanning calorimetry [36].

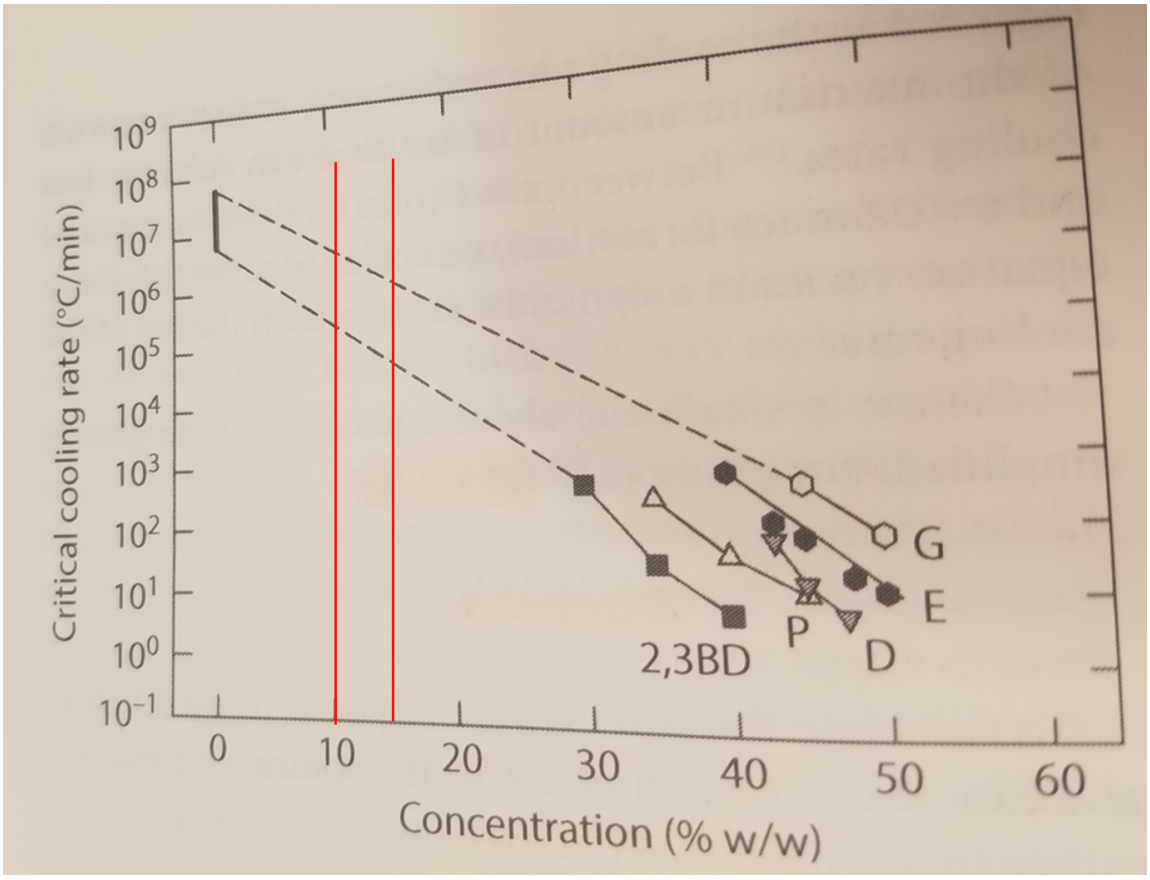

Figure 1-10: Critical cooling rates for mixtures of pCPAs and water [44]. Red lines are used to indicate the predicted range of critical cooling rates needed to vitrify an oocyte directly prior to cooling. **G** refers to glycerol, **E** refers to ethylene glycol, **D** refers to DMSO, **P** refers to propylene glycol, and **2,3BD** refers to 2,3 butanediol.

The effect of other solutes, such as salts, and macromolecules, such as polymers and proteins, present inside the cell may also play an important role in discouraging ice formation, but the extent of their impact has not been broadly investigated. Moreover, it is possible that, like toxic CPA effects and osmotic shock, IIF is inevitable and the key to successful vitrification is not inhibiting it, but minimizing it to an acceptable degree. For instance, studies with monocytes suggest that ice crystals as large as ~400 nm can exist without cell death occurring, pointing to a level of cellular robustness to IIF [59]. Finally, this discrepancy may exist partially because of the potential lack of importance of cooling rate, relative to other system parameters, to successful vitrification. For instance, preliminary studies using mouse oocytes have shown that it is possible to achieve post-warm survival rates of >80% using cooling rates as low as 95 $\frac{^\circ C}{min}$, provided that warming rates are very high (~10^5) [60]. Thus, it is possible that rapid warming, as opposed to cooling, is a more powerful determinant of successful vitrification.

Beyond this lone empirical result, the thermodynamics of ice formation tend to support the conclusion regarding the importance of rapid warming in mitigating

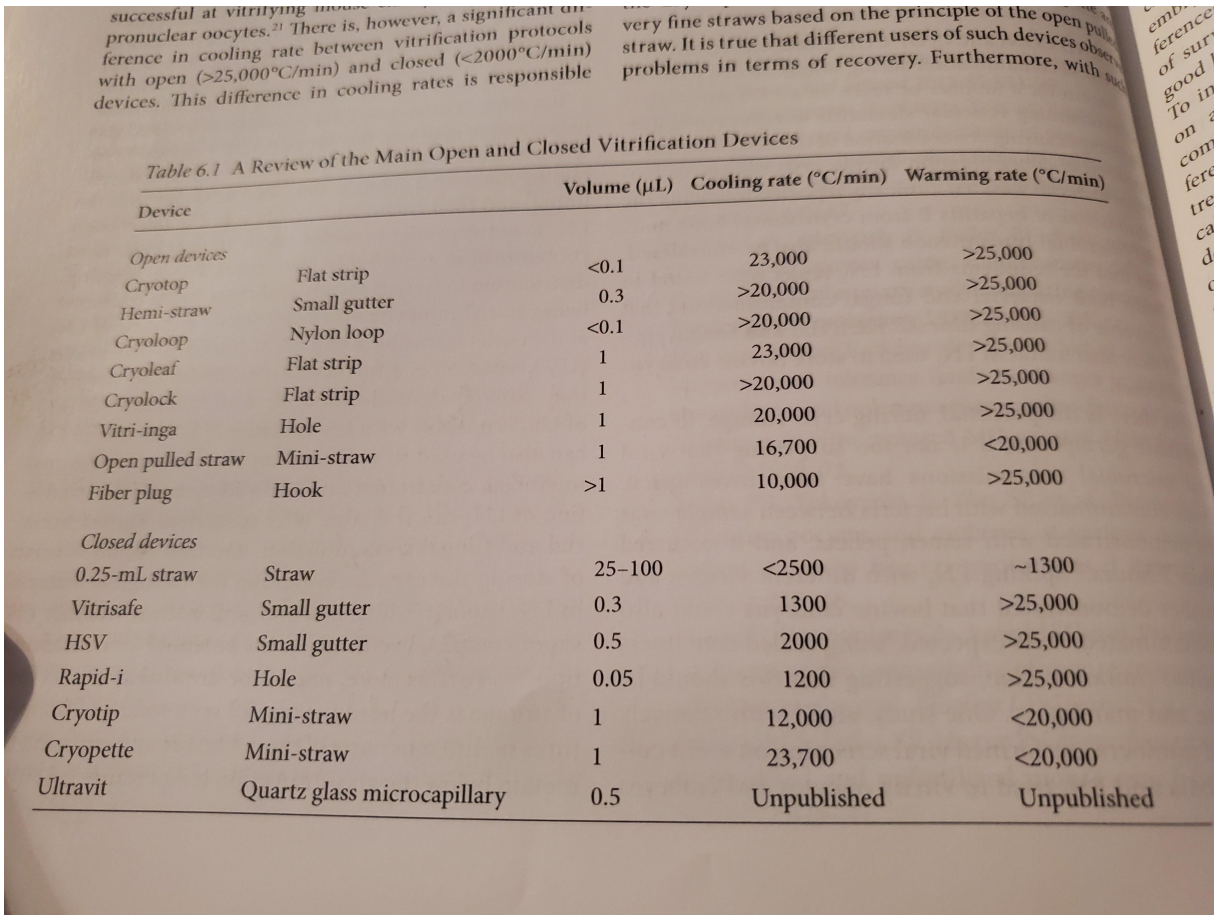

successful at vitrifying [illegible] pronuclear oocytes.[21] There is, however, a significant difference in cooling rate between vitrification protocols with open (>25,000°C/min) and closed (<2000°C/min) devices. This difference in cooling rates is responsible

very fine straws based on the principle of the open pull straw. It is true that different users of such devices obser problems in terms of recovery. Furthermore, with su

Table 6.1 A Review of the Main Open and Closed Vitrification Devices

Device		Volume (µL)	Cooling rate (°C/min)	Warming rate (°C/min)
Open devices				
Cryotop	Flat strip	<0.1	23,000	>25,000
Hemi-straw	Small gutter	0.3	>20,000	>25,000
Cryoloop	Nylon loop	<0.1	>20,000	>25,000
Cryoleaf	Flat strip	1	23,000	>25,000
Cryolock	Flat strip	1	>20,000	>25,000
Vitri-inga	Hole	1	20,000	>25,000
Open pulled straw	Mini-straw	1	16,700	<20,000
Fiber plug	Hook	>1	10,000	>25,000
Closed devices				
0.25-mL straw	Straw	25–100	<2500	~1300
Vitrisafe	Small gutter	0.3	1300	>25,000
HSV	Small gutter	0.5	2000	>25,000
Rapid-i	Hole	0.05	1200	>25,000
Cryotip	Mini-straw	1	12,000	<20,000
Cryopette	Mini-straw	1	23,700	<20,000
Ultravit	Quartz glass microcapillary	0.5	Unpublished	Unpublished

Figure 1-11: Cooling and warming rates of different commonly used vitrification platforms [58].

IIF [36]. The formation of ice crystals can be categorized by two distinct steps, nucleation and crystallization. Nucleation describes the process by which ice nuclei form from liquid water, and act as an anchor for further growth by the process of crystallization. Both processes, as can be seen in **Figure 1-12**, have distinct temperature dependencies, with ice nucleation being favored at temperatures well below water's equilibrium freezing point of 0 °C, and ice crystallization being favored just below water's equilibrium freezing point. This is because ice nucelation depends on the removal of kinetic energy in order for water molecules to come closer together with sufficiently low momentum to form nuclei.[6] Crystallization, on the other hand, is a diffusion driven process, and thus depends on kinetic energy to drive molecular motion towards the nuclei. In the context of cooling, this means that when the oocyte is passing through the temperature regime for which crystallization is preferred, there are little to no nuclei within the oocyte, drastically limiting the degree of possible ice

[6]The parabolic shape for the time dependency of ice nucleation observed in **Figure 1-12** reflects the fact that there is a kinetic energy limit below which water molecules cannot come together and nucleate. This occurs as an aqueous solution gets close to its glass transition temperature, defined as the temperature at which the solution viscosity is 10^{13} Poise.

growth. As the temperature continues to decrease, the oocyte then enters the regime which favors ice nucelation. However, at such a low temperature, even if these nuclei form, the low level of kinetic energy makes crystallization minimal. Thus, during cooling, the risk of severe IIF to the oocyte is relatively low, even for relatively low cooling rates.

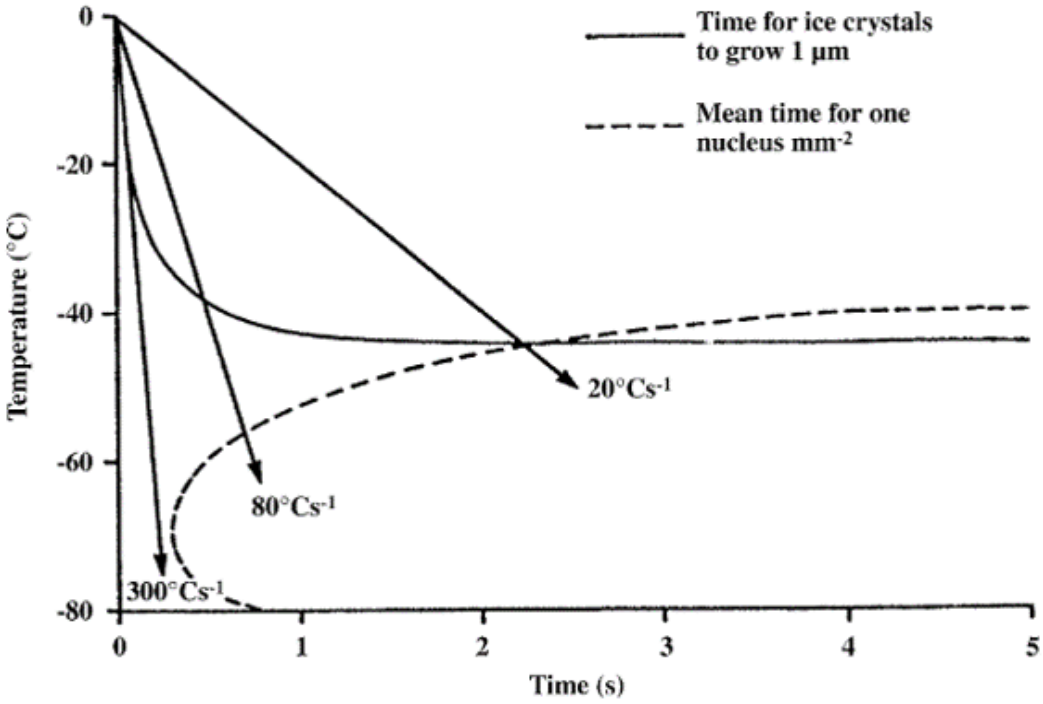

Figure 1-12: Impact of cooling rate on ice nucleation and crystallization [35]. This chart was created for a 50% w/v aqueous mixture of PVP, meaning precise numerical values should be ignored and this figure should be viewed solely for its qualitative characteristics. Note that for cooling, there are three possible outcomes with regards to ice formation. For fast cooling rates, both nucleation and crystallization can be avoided, for moderate cooling rates, nucleation may occur, but crystallization can be avoided, and for slow cooling rates, nucleation and crystallization can occur. The case of moderate cooling rates may justify why oocytes can be successfully vitrified using relatively low cooling rates.

When the oocyte is warmed, the order of travel for the oocyte is reversed; the oocyte passes through the nucleation-promoting temperature region prior to the crystallization promoting one. This makes the risk of IIF upon warming, referred to as devitrification, much higher than it was during cooling. For this reason, the predicted critical warming rates for mixtures of pCPAs and water, which are the minimum warming rates required to ensure that less than 0.2% of the solution mass is turned into ice, are orders of magnitude higher than their cooling rate counterparts (**Figure 1-13**). However, as with the the critical cooling rates, it can be observed that these predictions are many orders of magnitude lower than the warming rates reported by

successful oocyte vitrification platforms (**Figure 1-11**). This discrepancy can again be potentially attributed to the poorly understood IIF inhibiting properties of native intracellular solutes and molecules, and an unstudied robustness of the oocyte to some amount of IIF.

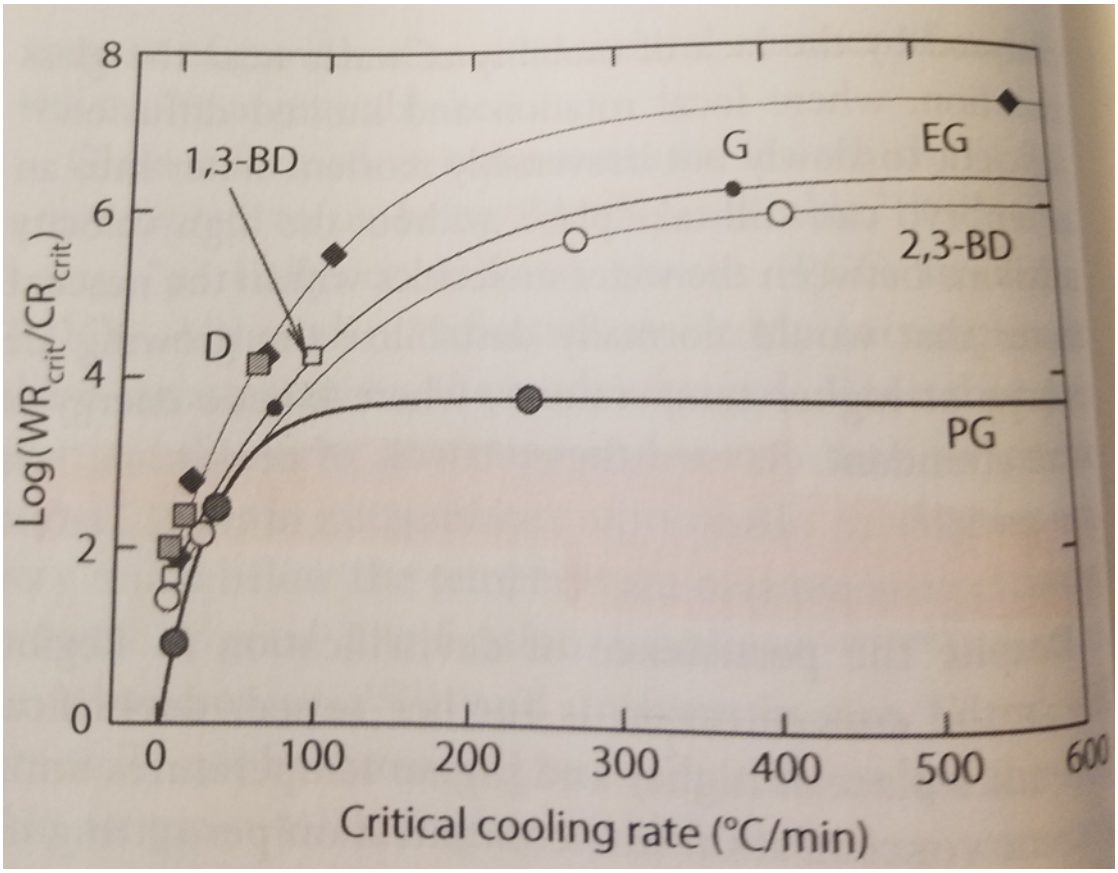

Figure 1-13: Logarithmic ratio of critical warming rates to critical cooling rates for mixtures of pCPAs and water [44]. **G** refers to glycerol, **EG** refers to ethylene glycol, **D** refers to DMSO, **PG** refers to propylene glycol, **2,3BD** refers to 2,3 butanediol, and **1,3BD** refers to 1,3 butanediol.

In conclusion, while much work has been dedicated to understanding the physics of ice formation in pure water and in mixtures of water and pCPAs, these models do a very poor job of estimating the true cooling and warming rates needed to prevent lethal levels of IIF. This is evidenced by the fact that successful oocyte vitrification platforms use cooling and warming rates well below those predicted by these models. While some suspect that these discrepancies can be attributed to poorly understood contributions of intracellular solutes and molecules and/or a robustness to some amounts of IIF, the true reasons are unknown and require further investigation to be better understood.

1.4.5 Glass fracture and vitrification at minimum volume

In addition to IIF, osmotic shock, toxic CPA effects, and chilling injury, oocytes are susceptible to another form of injury called glass fracture. Glass fracture, as its name denotes, is the formation of cracks and fractures inside the oocyte while it is in a vitrified or glassy state (**Figure 1-14**). Crack formation is brought on by the extreme thermomechanical stresses induced by rapid warming and cooling of the oocyte below its glass transition temperature, T_g, or the temperature at which the oocyte reaches a viscosity of 10^{13} Poise [61, 62]. It was found in [63] that there were three primary factors that impact the probability of glass fracture, P_{gf}, that's relationship can be described as

$$P_{\text{gf}} \propto \frac{\Delta T}{\Delta t} \times V \times \phi_{\text{CPA}} \tag{1.1}$$

where $\frac{\Delta T}{\Delta t}$ denotes the cooling/warming rate, V denotes the size of the oocyte-containing volume, and ϕ_{CPA} denotes the CPA concentration of the vitrificiation solution.

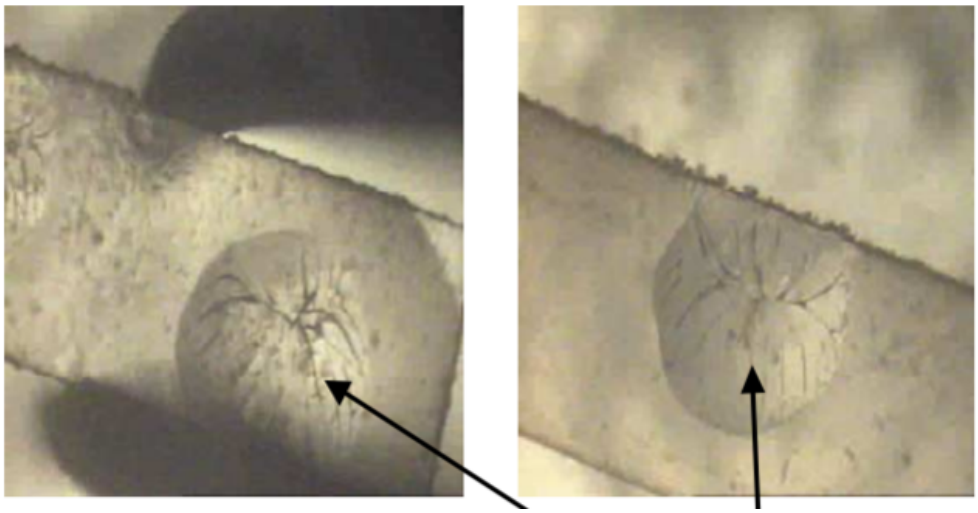

Figure 1-14: Glass fracture in droplets of vitrification solution [63]. Black arrows point to individual fractures in the droplet.

All parameters in the above equation increase P_{gf} by increasing the magnitude of the developed thermomechanical stress. Higher cooling/warming rates and larger volumes increase the magnitude of the temperature difference between the inner and outer portions of the droplet, exacerbating thermomechanical stresses. Higher cryoprotectant concentrations increase the solution viscosity and thus raise the solution's T_g. To better understand why this is an issue, it should be noted that the boiling point of liquid nitrogen is -196 °C, and the T_g of pure water is -137 °C [64]. By raising the T_g of the solution, the size of the temperature range for which the solution is a glass increases, which inevitably increases the magnitude of thermomechanical stress development in the glass.

Analyzing the above equation and recalling previous discussion throughout this section, it can immediately be recognized that $\frac{\Delta T}{\Delta t}$ and ϕ_{CPA} are not only related

to increases in P_{gf}, and that decreases in either of these values increases the risk of lethal IIF. Thus, in order to reduce the risk of glass fracture without increasing the risk of IIF, the only available solution is to reduce the size of the oocyte containing volume. In fact, this decision also reduces the risk of IIF by reducing the thermal mass undergoing cooling/warming [7], thus increasing the overall cooling/warming rate. The critical volume below which glass fracture was shown to be drastically minimized was ~1 μL, in line with the recommendation of a 0.1 μL vitrification volume described in sec. 1.2 [63]. However, the carrier device for this study was a glass slide (**Figure 1-14**), which formed a droplet-like geometry for the oocyte-containing volume. It is unclear how this upper volume bound of ~1 μL translates to other geometries for the oocyte-containing volume.

1.4.6 Oocyte vitrification: a vaguely understood balancing act

From the discussion throughout this section, two realities regarding oocyte vitrification should be clear. First, successful oocyte vitrification is a delicate, complex process that requires the determination of a set of parameters that adequately balances the risks of many different forms of cell damage. The relationship between a few key parameters and different forms of cell damage can be found in **Figure 1-15**. While this list of parameters is not exhaustive (excluded parameters include design of vitrification solution, design of loading/unloading protocol, and selection of vitrification platform), this figure effectively summarizes many important conclusions made throughout this section, while also communicating the complexity of tuning this design space.

The second reality regarding vitrification that has been communicated throughout this section is that, while researchers' understanding of the oocyte vitrification process has grown immensely over the past four decades, there is still much that has yet to be understood. The reasons for this, in the opinion of the author, are multifaceted. Firstly, oocyte vitrification is a uniquely difficult topic to study. The combined thermal, time, and length scales involved in the oocyte vitrification process pose challenges experienced by few other fields, necessitating the creation of novel measurement systems and techniques to accurately monitor what is happening during oocyte vitrification. Moreover, aside from its scientific merit, the need to deeply understand the effects of vitrification at the single cell level are uniquely important to oocyte vitrification; no other application of cryopreservation calls for the individual vitrification of such a tiny population of massive cells. Robustness to cell damage, afforded either by an increase in population size or by regenerative, multicellular networks, may have allowed researchers in cryopreservation to avoid answering these deeper, more fundamental questions. For oocytes, however, these questions are key to understanding and perfecting a clinical process that has hitherto been guided by trial and error.

[7] Technically, it is the surface-to-volume ratio, and not strictly the volume, that impacts the cooling/warming rate. For a more in-depth discussion, go to sec. 5.3.1

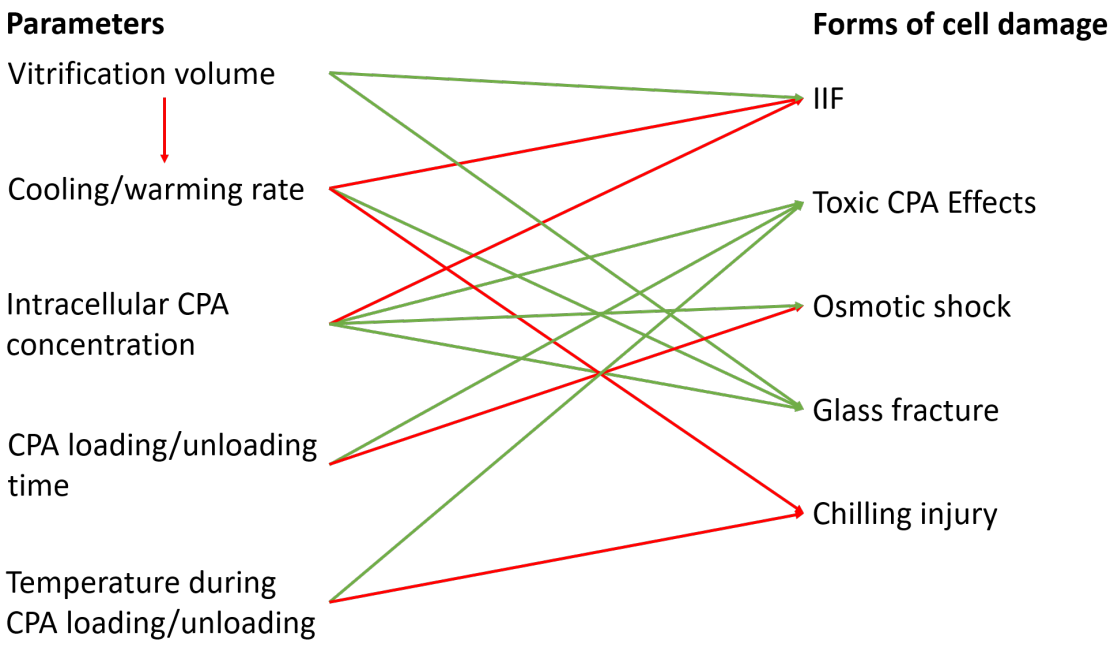

Figure 1-15: Relationship between key vitrification parameters and different forms of cell damage. Green arrows between parameters and forms of cell damage should be read as "An increase/decrease in *parameter* increases/decreases the risk of *form of cell damage*". Red arrows between parameters and forms of cell damage should be read as "An increase/decrease in *parameter* decreases/increases the risk of *form of cell damage*". The red arrow between "vitrification volume" and "cooling/warming rate" is meant to indicate that a decrease in the former leads to an increase in the latter. All other parameters can be controlled independently, but are inherently coupled through their relationships with the different forms of cell damage.

The lack of understanding in oocyte vitrification may also be attributed to the complicated relationship between funding sources and assisted reproduction. As evidenced by the historical lack of both public and private funding for oocyte cryopreservation and other assisted reproductive procedures (see sec. 1.2), the level of priority for the advancement of assisted reproductive knowledge and technologies has traditionally been low. It is only now, as discussed in sec. 1.1, that significant amounts of private funding have begun to be dedicated towards providing improved levels of service and access for patients. However, as private funding comes with the heavy burden of a return on investment, it is unlikely that these new partnerships will shed light on the fundamental phenomena underlying oocyte cryopreservation. It is for this reason that academia-industry partnerships, such as this project, are vital to the advancement of both the technological AND theoretical aspects of oocyte cryopreservation.

1.5 Existing vitrification platforms

1.5.1 Commercial platforms

GAVI system

The GAVI system, a product of Australian company Genea Biomedx, has shown a fair amount of success in the vitrification of human embryos and blastocysts, with results comparable to those reported using the Cryotop method [65,66]. The platform boasts a throughput of either 8 oocytes or 4 embryos/blastocysts per vitrification cycle, making it slightly lower than the current clinical throughput using manual vitrification (see section 1.3). This success has resulted in the evaluation of this platform's clinical viability in performing embryo vitrification through an ongoing clinical trial in France [67], and the platform has also achieved CE certification for use in Europe [65].

Operation of this platform begins with the manual loading of an embryo to a patently designed "pod" (**Figure 1-16**). The pod is then loaded into the the GAVI tray and placed into the GAVI. Inside the GAVI is an automated liquid handler that periodically changes the solution surrounding the embryo in order to load CPAs into the embryo. Due to the pod's design, the platform is able to achieve a continuously increasing gradient in CPA concentration by utilizing diffusion. Once the CPAs are fully loaded into the embryo, the pod is automatically closed at the top via a heat seal. The operator must then manually remove the pod, and dunk it in liquid nitrogen while stirring. The pod in liquid nitrogen is then transferred to a storage vessel for long term storage. These CPA loading and cooling steps were taken from the platform's video workflow, created by Genea Biomedx, which can be found here.

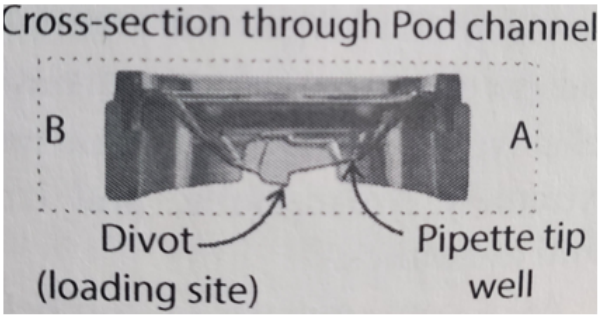

Figure 1-16: Cross section of the Gavi Pod [65]

To warm the embryo, the operator needs to remove the pod from the liquid nitrogen, and immediately swirl the pod in water preheated to 37 °C for ~2 seconds. The pod seal must then be manually removed, and 10 microliters of a warming solution must be added manually to the contents of the pod. The embryo is then transferred manually from the pod to increasingly dilute CPA solutions for the purpose of CPA unloading. Following CPA unloading, the embryo is transferred to culture medium in preparation for implantation. These warming and CPA unloading steps were taken

from [68], which is an article written by the scientists and engineers at Genea Biomedx describing how they performed embryo vitrification using the GAVI system.

The GAVI system, while an improvement on manual vitrification, presents many challenges in the context of an ideal oocyte vitrification system. Most fundamentally, despite some initial reports validating the platform's efficacy at vitrifying human oocytes [69], this platform has yet to prove itself as a clinically viable oocyte vitrification tool. Oocyte vitrification is considered to be more challenging than embryo vitrification because of the oocyte's comparatively low permeability [70] and high surface to volume ratio relative to embryos [71]. As a result, it is harder to remove water from the oocyte and introduce CPAs into the oocyte, increasing the risks of both toxic CPA effects and IIF. Moreover, as an embryo consists of a population of pluripotent stem cells, it is inherently more robust to the death of a few cells than the single-single celled oocyte. It is therefore important to recognize that warming and cooling rates that are successful at vitrifying embryos may not be high enough to successfully vitrify oocytes. Therefore, a major cause for concern is the reported cooling and warming rates of the GAVI system, being approximately 11,400 $\frac{^{\circ}C}{min}$ and 8,600 $\frac{^{\circ}C}{min}$ respectively [65]. These values are approximately one half and one fifth of the cooling and warming rates of the Cryotop method respectively. While the creators attribute this to an inherent limitation of a closed system[8] [68], this belies inherent limitations in the creators' choice of a "pod" as the oocyte carrier, and its consequent design. Furthermore, the submerging and removal of the oocyte from liquid nitrogen, as well as CPA unloading, are all still performed by hand. As a result, the GAVI system will still inevitably suffer from the same limitations of manual vitrification, particularly during the warming and CPA unloading process, where the protocol using the GAVI system seems even more technically complicated than when performing manual vitrification. This complexity can make the oocyte more susceptible to devitrification and CPA toxicity upon warming. The effect of these shortcomings on Gavi's ability to meet the criteria of an "ideal vitrification system" is summarized in **Table 1.2**.

SARAH

Another platform attempting to improve upon manual vitrification is SARAH, a product of Israeli company fertileSAFE. This platform has yet to be used for the vitrification of human cells and tissues, but has begun to show promise in experiments vitrifying both murine and bovine oocytes, embryos, and blastocysts [72]. The creators claim a single vitrification cycle using SARAH can successfully vitrify up to 30 embryos/oocytes, which exceeds current clinical throughput.

Operation of SARAH begins with loading of oocytes/embryos onto "mini straws", which are devices similar in form and function to the Cryotop sheet (see sec. 1.2). The device can accommodate up to six mini straws, with each one holding up to five oocytes/embryos. A special cap, with a pore size of 50 microns, is then attached to

[8] A closed system involves the use of a vitrification platform that prevents direct contact between the oocyte and liquid nitrogen. The benefits of a closed system are that it prevents cross contamination between patient samples, and it prevents contamination of patient samples by potentially unsterile liquid nitrogen. For a more in depth discussion on this matter, see [58].

Figure 1-17: Picture of the SARAH platform. Note that the most of the small plates contain CPA solutions, and the large, green plate contains liquid nitrogen [72].

the end of each straw to ensure that the oocytes/embryos do not fall off the straws during the CPA loading process. **Note that a typical oocyte has a cytoplasmic diameter of 113 microns, and a total diameter (including the perivitelline space and zona pellucida) of 164 microns** [73]. Each straw is then loaded into a robotic arm capable of moving up and down. Below this robotic arm is a motor-actuated lazy Susan with a series of plates located at its edges (**Figure 1-17**). All but two of these plates contain increasingly concentrated solutions of CPAs; one plate contains absorbing paper that soaks up excess solution prior to vitrification, and one plate contains liquid nitrogen for cooling. To perform CPA loading, the robotic arm lowers the straws into a given CPA solution for a predetermined amount of time. When the time in that CPA solution has elapsed, the vertical arm raises, the lazy Susan turns until the next, more concentrated CPA solution is directly under the robotic arm, and the robotic arm lowers once again into this new CPA solution. This process is repeated until the oocytes/embryos are fully loaded with CPAs, at which point the plate containing the absorbing paper is moved under the robotic arm. The straws are then lowered onto the absorbing paper to remove excess solution surrounding the oocytes/embryos prior to cooling. The robotic arm is then raised, the liquid nitrogen plate is positioned appropriately, and the straws are lowered by the robotic arm into the liquid nitrogen. The straws are then disconnected from the robotic arm, and moved to a long term storage tank.

For warming, the straws are manually removed from liquid nitrogen, and then quickly placed inside a warming solution at 37 °C for five seconds. The straws are then

quickly reloaded into the vertical robotic arm, and the process for CPA unloading is carried out by essentially reversing that of CPA loading; the robotic arm sequentially submerges the oocytes/embryos in increasingly dilute CPA solutions until all CPAs are unloaded from the oocytes. The oocytes are then submerged by the robotic arm into a plate of culture medium, until they are ready to be fertilized. The steps for the entire vitrification process were taken from the platform's video workflow (created by fertileSAFE and can be found here), and from [72], which is an article written by the scientists and engineers at fertileSAFE describing how they performed oocyte/embryo vitrification using SARAH.

Like the GAVI system, SARAH has yet to prove itself as a clinically viable oocyte vitrification tool. Though it shows vast improvement in cooling and warming rates relative to GAVI, which were found to be 18,000 $\frac{^{\circ}C}{min}$ and ~21,000 $\frac{^{\circ}C}{min}$, respectively, these are still lower then those reported using the Cryotop method. Moreover, the warming process is still being performed manually, meaning that SARAH still suffers from some of the same limitations negatively impacting manual vitrification . Finally, the use of absorbing paper as a method of achieving minimal volume, while simple and easy to use, does not seem like a reliable, repeatable way to determine the volume in which oocytes will be vitrified. Issues stemming from this lack of precision become exacerbated when one considers that each straw has five oocytes located at different positions along its length, meaning that each oocyte likely experiences a different cooling and warming rate (and, likely, different CPA exposure profiles). The effect of these shortcomings on SARAH's ability to meet the criteria of an "ideal vitrification system" is summarized in **Table 1.2**.

RoboVitri

RoboVitri, a system developed by a team at the University of Toronto, is an automated robotic system that has shown promise as an embryo vitrification platform [74]. The platform claims to process embryos at three times the rate of manual vitrification. Despite this reported success, there exists few online resources for RoboVitri (no website, no new materials published since 2016) seeming to indicate little to no commercial development of the platform. However, for completeness, the operation and utility of this platform will be discussed.

RoboVitri is an integrated optical system that manipulates embryos via a motorized syringe attached to a robotic manipulator (**Figure 1-18**). The embryos begin in a dish of culture medium, which resides on a custom designed carrier plate. This carrier plate also accommodates a multiwell plate, to be filled with CPA solutions, and up to three "vitrification straws" (this is why the authors claim that their throughput is triple that of manual vitrification). The carrier plate rests on the motorized XY stage of a microscope. The process of CPA loading begins by detecting the embryos residing in the dish of culture medium. The microscope stage is automatically moved until the embryos are in the microscope's field of view, at which point they are automatically detected through image processing. Embryos are then automatically aspirated into the micropipette via the motorized syringe, and the micropipette is raised above the microscope stage by the robotic manipulator. The motorized XY stage then posi-

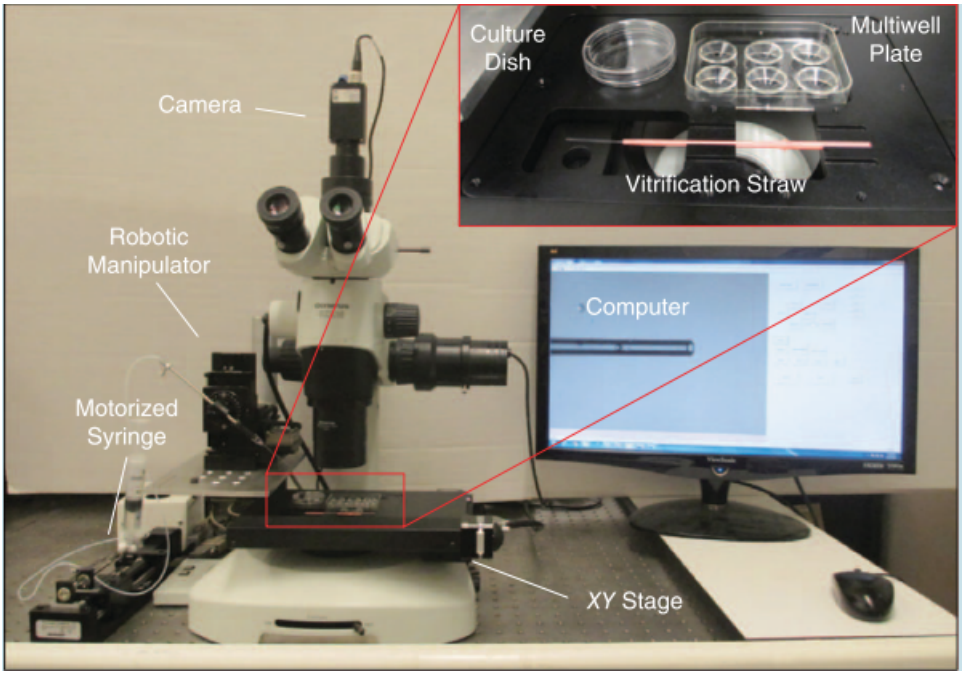

Figure 1-18: Labelled photo of the RoboVitri automated vitrification system. Inset shows a close up photo of the specially designed "carrier plate", which holds a dish of culture medium, a multiwell plate of CPA solutions, and "vitrification straws"

tions the first CPA solution below the micropipette, and the micropipette is lowered until it returns to its previous height above the stage. The motorized syringe then pushes the embryos out of the micropipette, and the embryos remain in this solution for a period of time prescribed by the protocol being used. This process of finding the embryos, aspirating them, lifting the micropipette, moving the stage, and redepositing the embryos into the next solution, is repeated until the embryos are fully loaded with CPAs. Once this occurs, the embryos are automatically retrieved from vitrification solution in the micropipette, and the XY stage positions the straws below the micropipette. The micropipette is then lowered down by the robotic manipulator until contact with the straw is detected. The embryos are then deposited onto the straws with a relatively large amount of excess volume. Following embryo deposition, the micropipette goes back to each straw, and slowly aspirates excess volume from the straw in order to ensure a maximum cooling/warming rate. The straws are then removed from the carrier plate, and manually inserted into liquid nitrogen by an operator. After cooling, the straws are transferred to long term storage. Warming and CPA unloading protocols are not explicitly specified, but it is assumed that, similar to manual vitrification, warming is accomplished by manually removing the straws from liquid nitrogen and quickly placing them in a warming solution preheated to 37 °C. CPA unloading is likely accomplished in the same automated fashion as CPA loading was, with the automated pipette transferring the embryo into CPA solutions of decreasing concentration until all CPAs are unloaded. These steps were taken from the platform's video workflow, created by the team at University of Toronto, which

can be found here.

This platform, while a brilliant technical accomplishment, does not appear to be an ideal oocyte vitrification system. Like GAVI and SARAH, it has not proven itself as a clinically viable oocyte vitrification tool. And, also like GAVI and SARAH, this platform is still only semi-automated; the crucial steps of cooling and warming are still performed manually, making them just as liable to error as with manual vitrification. Moreover, the need for the platform to visualize the embryos, while incredibly useful in the real time monitoring of CPA loading and unloading, can cause issues when the embryos are transferred to relatively high density CPA solutions. In these solutions, the embryos can have a tendency to float and drift within the well, which has resulted in the embryos entering "blind regions" where they can no longer be visualized [75]. The effect of these shortcomings on RoboVitri's ability to meet the criteria of an "ideal vitrification system" is summarized in **Table 1.2**.

Table 1.2: Evaluation of existing commercial vitrification platforms based on criteria of an "Ideal clinical system" described in sec. 1.3. A rating of 1 indicates that a criterion is poorly met or not addressed, and a rating of 5 indicates the criterion is well met.

	Comprehensive	**Easy to operate**	**High fidelity**	**High throughput**	**Space Efficient**
GAVI	2	3	5	4	5
SARAH	4	3	2	5	5
RoboVitri	3	3	2	3	4

1.5.2 Microfluidic platforms

Microfluidic platforms developed for oocyte vitrification have predominantly attempted to simplify the process of CPA loading and unloading.[9] These devices can be separated into two classes depending on how they process the egg: confinement devices and free flow devices. Confinement devices are devices in which the oocyte is physically immobilized during the CPA loading and unloading process. This immobilization has been achieved through a physical obstruction across a pressure difference (**Figure 1-19a**) [54, 57], as well as through confinement within a droplet on an electrowetting-on-dielectric (EWOD) device (**Figure 1-19b)** [78]. The chief benefit of confinement devices is the control the user has over the chemical environment of the oocyte throughout the entire CPA loading and unloading process, which has allowed researchers to experiment with concentration profiles not possible using commercial platforms or manual vitrification. However, for the case of physical obstructions, one

[9]There has been some work that attempts to use microfluidics to aid in the cooling/warming steps of vitrification, but this work has been limited to small cells like sperm [76]. There is also recent, promising work that attempts to reduce the risk of IIF through microencapsulation of cells in hydrogels [77], but this strategy has yet be shown effective in vitrifying cells as large as oocytes.

primary disadvantage is the need to press cells up against device walls. Even with surface blocking, cells have a tendency to stick to device walls, making oocyte retrieval from the device difficult. Furthermore, localized stresses on the cell induced during this pressing have the potential to damage or impair the oocyte. Another disadvantage of confinement using physical obstructions is that such confinement strategies work well only for particle populations with a low (~4%) coefficient of size variation (COSV) [79]. As the COSV of human oocytes is >10% [73], it is likely that not all oocytes would be effectively confined. For the case of confinement using EWOD, one major disadvantage involved is the complexity of fabrication and operation relative to other, more traditional microfluidic devices. Furthermore, this method has only been shown to work for embryo vitrification, and has not been tested using oocytes.

Free flow devices exploit laminar microfluidic flow, using diffusion for controlling the chemical environment around the cell (**Figure 1-19c**) [80]. These devices consist of multi-channel junctions where the oocyte and CPAs get introduced, followed by long, serpentine channels that allow for CPAs to diffuse into the oocyte. The primary advantage of free flow devices is that, unlike confinement devices with physical obstructions, oocytes in free flow devices never make contact with internal device surfaces. Moreover, the fact that CPAs are being delivered to the oocyte via diffusion as opposed to convection provides a natural grading of CPAs to the cell. The major downside of this approach is that the evolving chemical environment around the oocyte cannot be changed following its introduction into the device. This makes it difficult to correct for variations in oocyte positioning in device channels, which will effect the graded CPA profile experienced by the oocyte [81], as well as natural heterogeneity in membrane permeability [70], ultimately contributing to suboptimal vitrification success.

In addition to the described shortcomings of the developed microfluidic CPA loading and unloading devices, little work has been done towards developing an automated work flow that will load the oocyte onto a vitrification platform with minimal external volume, submerge it in liquid nitrogen for rapid cooling, and remove it from liquid nitrogen for rapid warming. As discussed extensively in sec. 1.4, there is a great deal of nuance and subtlety impacting the post warm survival rate of oocytes that will remain poorly quantified and understood as long as these processes remain manually operated and non-standardized. In the following sections, this report will focus on the progress being made towards creating a CPA loading and unloading device that fits the criteria of section 1.3, with the understanding that this work should be viewed in the larger context of developing a comprehensively automated oocyte vitrification system (this will be revisited in sec. 5.3).

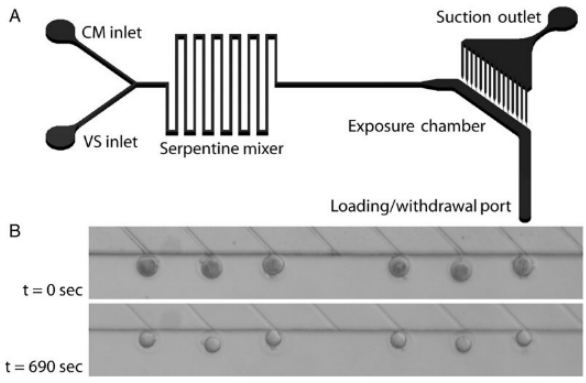

(a) Confinement device using physical obstruction across a pressure difference [54]

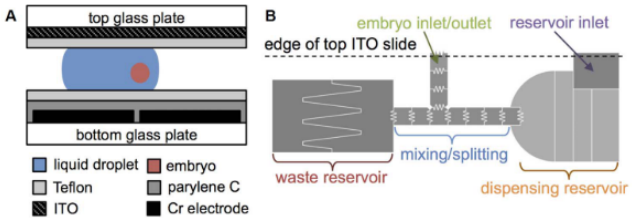

(b) Confinement device using EWOD [78]

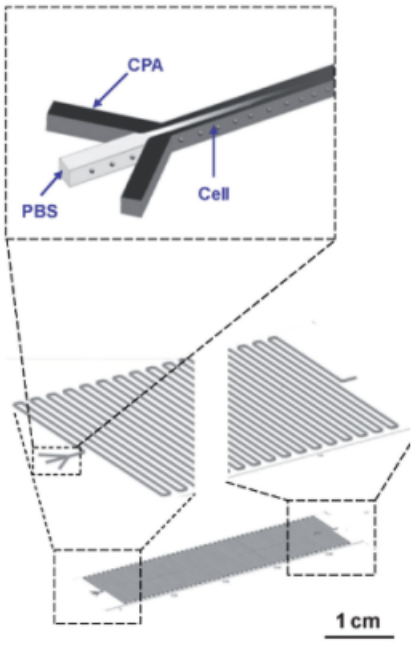

(c) Free flow device [80]

Figure 1-19: Different types of microfluidic devices used for CPA loading and unloading

Chapter 2

Proposed Approach

2.1 Overview

From the discussion in section 1.5 it is clear that there is no single vitrification platform, either in the literature or on the market, that simultaneously meets all the criteria set forth in section 1.3. However, it can be observed that different platforms excel at different criteria, motivating the notion of combining the positive aspects of different platforms to create a new platform that meets all criteria of an ideal vitrification system. In the coming section, the design of an ideal vitrification will be outlined by drawing upon the knowledge of the previous chapter, and applying new knowledge that has yet to be used towards oocyte vitrification.

2.2 Microfluidic Device

It was decided that the ideal oocyte handling device for CPA loading and unloading should be a microfluidic one. One justification for this decision was by drawing inspiration from the RoboVitri system; of all the commercial platforms described, the RoboVitri system was the only one that enabled real time visualization of the oocyte during CPA loading and unloading. Volumetric changes in the oocyte have long been used in manual vitrification to signal the completion of various steps of the CPA loading and unloading processes (see section 1.2), and provides valuable information in the optimization of loading and unloading protocols. Without this information, the user is forced to apply a feedforward, "one-size-fits-all" approach to vitrification, which fails to account for oocyte to oocyte heterogeneity. One of the downsides of the RoboVitri system was oocyte drift during CPA loading and unloading. However, if the multiwell plate of the RoboVitri system was replaced with a microfluidic device that more rigidly confined the oocyte position and motion, this issue becomes resolved. The use of a microfluidic system also helps enable precision liquid dispensing, which will be crucial in achieving repeatable cooling and warming rates and minimizing the probability of glass fracture.

Once it was decided that the platform should consist of a microfluidic device interrogated by a microscope, the microfluidic device design needed to be determined.

As was discussed in section 1.5.2, both classes of microfluidic devices had their respective downsides. While confinement devices using physical obstructions give the user incredible control over the oocyte's chemical environment, they do not perform well with particle populations with a large COSV and can make oocyte retrieval difficult. While confinement devices using EWOD addressed these issues, complexity in fabrication and operation made this style of platform undesirable. As for free flow devices, while oocyte retrieval is straightforward because of the limited contact of the oocyte with the device walls, it does not allow the user significant control over the oocyte's chemical environment after loading. Therefore, to merge the benefits of all these devices, a device needed to be conceived that was simple to fabricate and operate, but also needed to give the user control over the oocyte's chemical environment throughout the CPA loading and unloading process. To this end, a single layer, multi-channel device using hydrogel microwindows (HMWs) was conceived.

HMWs are thin, hydrogel membranes that are manufactured *in situ* in a microfluidic device (**Figure 2-1**) [82]. The novelty of this technology is that, because of hydrogels' high porosity and permeability, HMWs allow for diffusion across them but act as a barrier to convective forces. Thus, a microfluidic device, as described in **Figure 2-2**, can be created where the oocyte resides in a central channel flanked on either side by two side channels. A section of these side channels will be separated from the main channel via HMWs, and the oocyte will be positioned in this section during CPA loading and unloading. CPA concentration profiles would be controlled by altering solution concentrations flowing in the side channels, and would be smoothed out by diffusion prior to arriving at the oocyte. Thus, the described system provides real time visualization of the oocyte, control over the oocyte's chemical environment throughout the loading/unloading process, and precludes the need to physically immobilize the oocyte in ways that risk damaging it or making it hard to retrieve.

2.3 Oocyte Position Control

To realize the device outlined in **Figure 2-2**, it is important that oocyte position and motion are carefully controlled in a way that does not fall victim to the shortcomings of traditional confinement devices. The RoboVitri system demonstrated that it is straightforward to create an optical system capable of recognizing and locating oocytes. To achieve oocyte position control, the described system will integrate this kind of optical system with three-point flow control to move the oocyte and monitor it's position. Three-point flow control has been shown to be an effective method for the control of cell position and motion [83, 84]. By designing a simple control algorithm that turns optical inputs regarding the oocyte position to flow based outputs designed to modify it, the desired tight control over oocyte position and motion can be achieved.

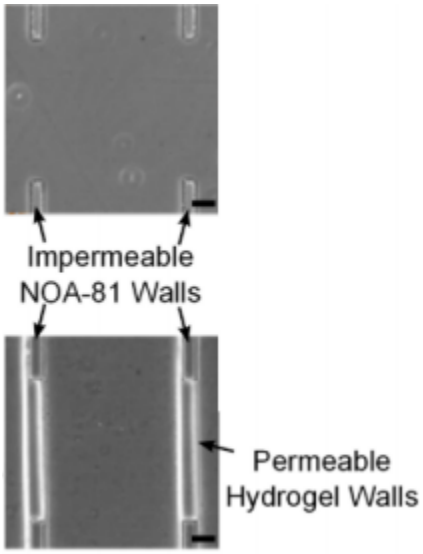

Figure 2-1: Hydrogel Microwindows (HMWs). Hydrogel microwindows serve as a barrier to convection, but, because of their high porosity and permeability, allow for diffusion across them. NOA-81 refers to an optical adhesive that, in this instance, was used as a building material for a microfluidic device [82].

2.4 Cryoprotectant Concentration Measurement

A shortcoming of all the previously mentioned platforms is their inability to monitor the chemical environment of the oocyte in real time. Some platforms, such as the GAVI and SARAH systems, opt for completely open loop approaches, wherein the extracellular solution concentrations are set prior to the CPA loading and unloading processes, and are assumed to permeate the oocyte in the time period prescribed by the protocol. In reality, while time is a useful measure of toxic CPA effects, the use of time as a measurement of progress through CPA loading and unloading is a vestige of manual vitrification. For instance, small changes in the volume of extracellular solution during solution to solution transfer can contribute to heterogeneties in the loading and unloading processes. This reality contributes greatly to the frantic pipetting required in manual vitrification following the introduction of the oocyte to vitrification solution (see section 1.2). And, while the GAVI system tries to control for this through the use of an automated liquid handling system (unclear what the tolerances on this system are), the SARAH system does not.

For microfluidic systems that introduce CPA solutions via convection, this problem is not as much of an issue as any solution surrounding the oocytes is being constantly replaced by new, upstream solution of known concentration. However, as was discussed previously, the containment methods needed to enable these systems often result in problems of their own regarding oocyte damage and retrieval. The proposed method of CPA introduction, as described previously, is able to overcome these problems, and involves gently introducing CPAs to the oocyte via diffusion. While this gentle grading minimizes osmotic damage to the oocyte, the consequence of this

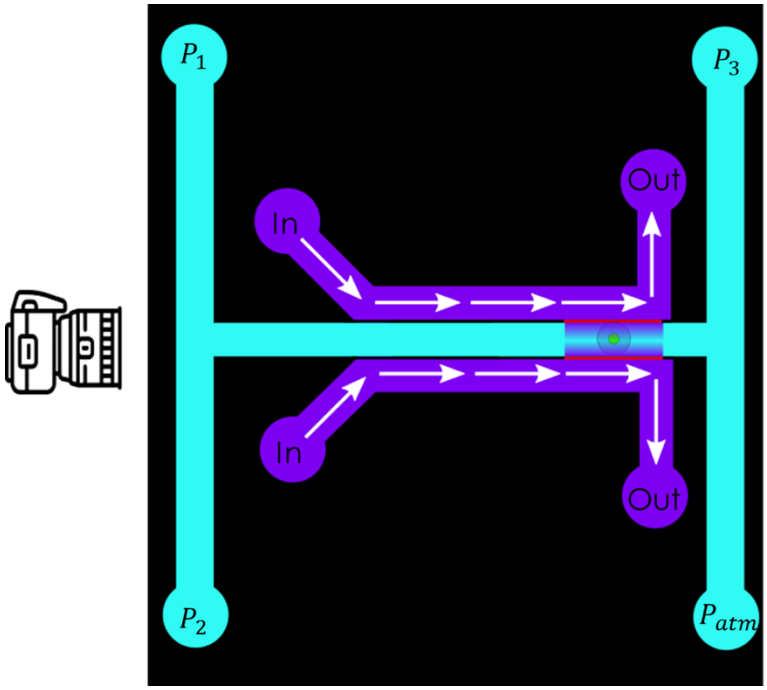

Figure 2-2: Proposed schematic for ideal CPA loading and unloading device. The oocyte position is monitored by a camera which informs a control algorithm to adjust pressures P_1, P_2, and P_3 accordingly. Chemicals are introduced at the inlets (labelled "In" above), and reach the oocyte by diffusion through the hydrogel microwindows (represented by red lines above). When the oocyte is ready for vitrification, P_1, P_2, and P_3 are adjusted to drive the oocyte to the device exit (labelled P_{atm} above).

is that overall oocyte volume changes can be small [57]. Without visible changes to the oocyte volume, it becomes difficult to gauge when the oocyte is finished with CPA loading and unloading. For the case of CPA loading, this increases the risk of toxic CPA effects on the oocyte. Moreover, uncertainties in diffusion coefficients of CPAs[1] can result in huge differences between expected CPA exposure conditions and real ones. These potential issues become nonexistent if measurements of the chemical concentration in the vicinity of the oocyte are made.

Interferometric methods have proven effective at making *in situ* measurements of chemical concentrations in microfluidic devices that are fast, sensitive, and high resolution [88–95]. These methods rely on changes in refractive indices (RIs) that alter the interference patterns of diffracted light to infer information about either absolute or relative shifts in solution concentration. The primary drawback of most

[1]Recall that CPAs are small molecules (<70 Da) that are chosen to participate in hydrogen bonding with water. Their small sizes make empirical measurements using fluorescent proteins unfeasible, and their strong intermolecular interactions with water make theoretical predictions using the Stokes-Einstein equation inapplicable. As a result, the majority of work dedicated to understanding the diffusion of these small molecules in water is sparse and consists of non-traditional methods of diffusion measurements [85] and molecular dynamics simulations [86, 87]. This is all to say that, despite the highly deterministic physics of microfluidic systems, the parameter values, in this case, tend to be uncertain.

methods, however, is the degree to which they increase the complexity of device manufacturing. Back scattering interferometry (BSI) has shown promise as a versatile, simple-to-integrate measurement technique that can be used to detect changes in chemical concentration [96,97]. A sample BSI setup is shown in **Figure 2-3**, and relevant specifications and performance characteristics of this BSI system are provided in **Table 2.1**. This style of BSI platform is desirable as its modular nature does not increase the complexity of microfabrication and design. Moreover, the reported refractive index resolution of 1×10^{-6} is more than sufficient to resolve a system where the changes in concentration during CPA loading and unloading are approximately $\Delta RI_{\text{load}} = 3.66 \times 10^{-2}$ and $\Delta RI_{\text{unload}} = -4.43 \times 10^{-2}$ respectively (**Supplementary Note A.1**).

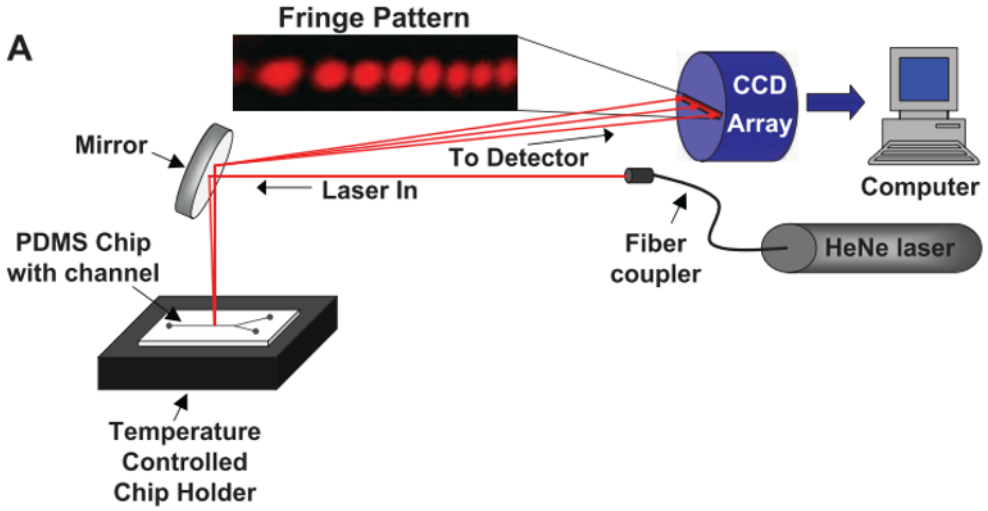

Figure 2-3: Representative setup of a microfluidic device being interrogated using BSI [96].

Table 2.1: Specifications and performance characteristics of a BSI system described in [96]

Compatible materials	**Compatible geometries**	**Temporal resolution**	**Spatial resolution**	**Refractive Index resolution**
Fused silica and PDMS	Circular, semicircular, and rectangular	Real-time	Depends on laser spot size, ~100 microns	1×10^{-6}

2.5 System Integration

By combining the microfluidic device, oocyte position control system, and CPA measurement system, an integrated optical system for CPA loading and unloading,

as shown in **Figure 2-4**, can be conceived. By combining microfluidics, automation, and optical measurement systems, this proposed system successfully integrates new technologies with the benefits of the platforms described in sec. 1.5, ultimately realizing an "ideal clinical system". In the coming sections, the progress towards the development of this system, and the work that still needs to be done, is described.

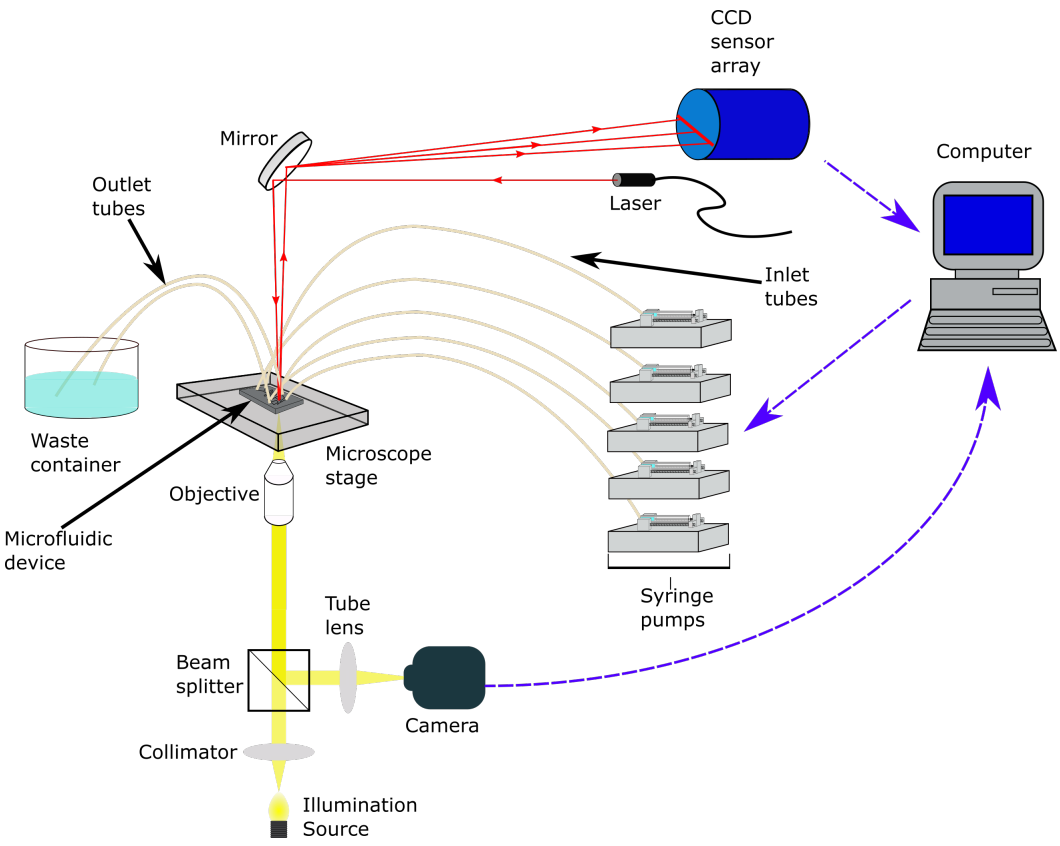

Figure 2-4: Schematic of proposed integrated system. The microfluidic device is loaded onto the microscope stage, and tubing is inserted into the device. Diascopic microscopy is used to visualize the device and monitor the oocyte position inside the device. Oocyte position information is monitored by a camera and sent to a computer for image processing. Position information inputs are converted to syringe pump inputs through a closed-loop control algorithm to alter the oocyte position accordingly. Back-scattering interferometry (BSI) is used to monitor the chemical environment around the oocyte.

Chapter 3

Microfluidic device fabrication

3.1 Device design

A CAD of a preliminary device design can be found in **Figure 3-1**. Relevant design specifications for the device can be found in **Table 3.1**, and detailed explanations regarding the determination of these specifications can be found in **Table A.1**. This design incorporates the features described in **Figure 2-2**, with the addition of a long serpentine mixing channel and two inlets for the introduction and mixing of vitrification solution and culture medium during the graded exposure of CPA solutions to the oocyte. It should also be noted that this device biases the location of the HMWs towards the device outlet. The motivation behind this is to reduce the time following CPA loading that it takes for an oocyte to be retrieved from the device, thus minimizing toxic CPA effects.

Table 3.1: Relevant design specifications of the CPA loading and unloading device design.

Specification	Channel width	Channel height	Length of mixing channel	Length of HMW slot	Width of HMW slot
Value	250 μm	250 μm	50 mm	500 μm	125 μm

Beyond the microfluidic features of the device, the following general considerations also needed to be taken into account when determining an appropriate device material. For the generation of HMWs, the device needed to be oxygen impermeable and transparent to UV light. The condition of UV transparency was determined because it was decided HMWs were to be manufactured using UV light. Unlike other methods of inducing hydrogel polymerization [98], selective patterning with UV light is fast, simple, and provides feature resolution on the order of optical systems. As it was desired to make HMWs as thin as possible so as to minimize diffusion time of CPAs to the oocyte, UV polymerization proved to be the simplest and best proven way to achieve this [82, 95, 99]. The condition of oxygen impermeability stems from oxygen's role as a free radical quencher in photopolymerization reactions. This restriction

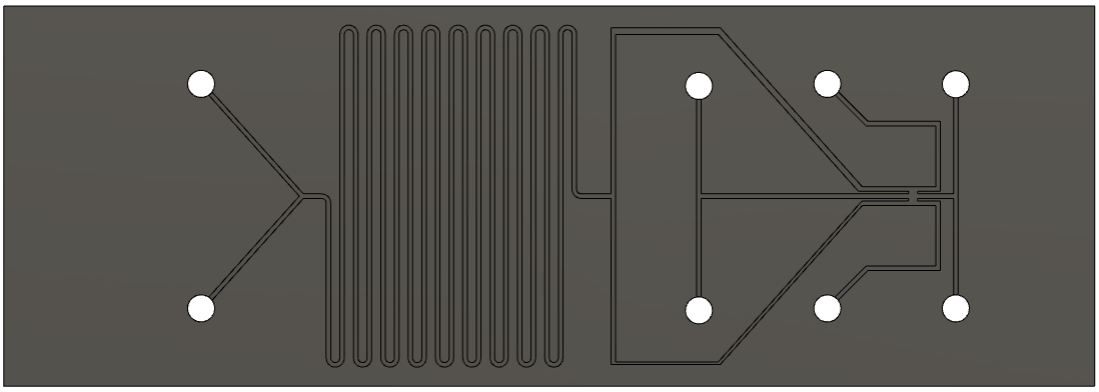

Figure 3-1: CAD of preliminary CPA loading and unloading device design. The device consists of two separate fluidic networks. The first, designed for the introduction of CPAs, consists of a mixing channel that splits into two side channels. The second, designed for the introduction and retrieval of the oocyte, consists of a symmetric H-shaped network of straight channels. The two networks merge at only two locations, which are both to be the sites of HMW fabrication.

rules out the traditional polydimethyl siloxane (PDMS) as a potential prototyping material, as its known permeability to oxygen has been used in a variety of applications to polymerize photoactive hydrogels designed to be flown out of the microfluidic device [100–103]. As HMWs are designed to be permanent structures within microfluidic devices, PDMS is an incompatible material. This motivated the need to use less conventional microfluidic materials, as will be explained in greater detail over the course of this chapter.

It was also important that the optical properties of the material used were consistent, and that device thickness was repeatable. This restriction stems from the need for reliability and ease in performing optical measurements of CPA concentration. While a calibration step will be performed prior to each CPA loading or unloading cycle, if the thickness and optical properties of devices vary widely from device to device, the task of automating optical measurement becomes increasingly challenging.

Finally, because the HMWs to be fabricated required high resolution UV patterning, the optical path to the region of HMW fabrication should remain relatively unimpeded. This is because increases in optical path length results in increased diffraction. Diffraction blurs the UV pattern and decreases effective resolution (**Figure 3-2**). Thus, to ensure high resolution UV patterning, the optical path to the region of HMW fabrication must be minimized. This requirement must be balanced with device integrity, meaning that the device must be relatively robust to mechanical handling and not be easily punctured or cracked.

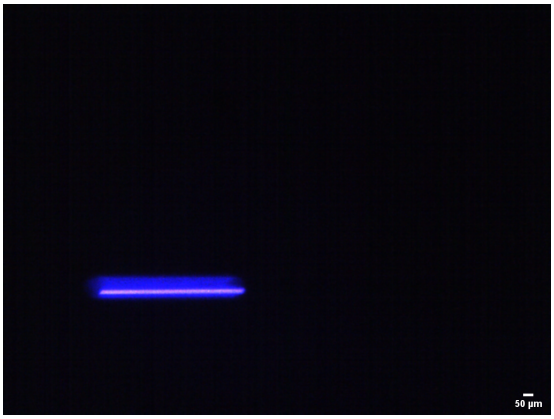

(a) Projection of straight line UV pattern through a glass slide with 1 mm thickness.

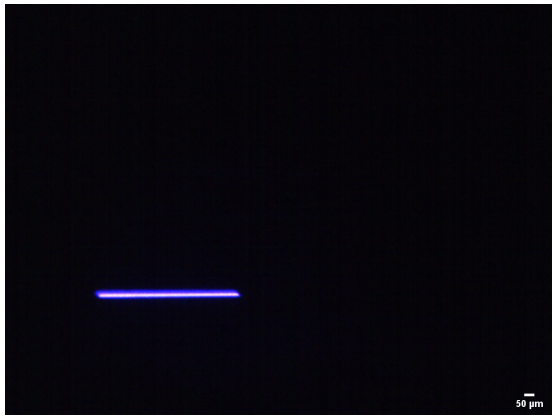

(b) Projection of straight line UV pattern through a #1 coverslip (thickness ~130-160 μm).

Figure 3-2: Effect of optical path length on UV pattern diffraction. The projected pattern of a thin, straight line segment is representative of the exposure conditions used to create an HMW. To ensure high resolution fabrication of HMWs, the optical path to the HMW fabrication region must be as unimpeded as possible.

3.2 Norland Optical Adhesive 81 as a candidate device material

3.2.1 Background and Material Properties

Norland Optical Adhesive 81 (NOA-81) is a liquid adhesive that cures to a tough, hard (Young's modulus=200,000 psi) polymer when exposed to UV light between 320 nm and 380 nm via a free radical polymerization reaction [104]. The transmission curve for the cured polymer can be found in **Figure 3-3**.

NOA-81 has been shown to be a viable and inexpensive alternative to PDMS for microfluidic applications [105–108], as well as highly biocompatible [109]. One of the major advantages of NOA-81 for this application is that it is oxygen impermeable, and as a result it has previously been used in the fabrication of devices containing HMWs [82, 99, 108]. NOA-81 also has shown to allow for the stability of long term (>40 days) surface treatments, a useful property in the event that surface blocking becomes necessary to prevent oocyte sticking. The material has also been shown to have a low level of autofluorescence, and it's native hydrophilicity makes channel wetting easier and the formation of persistent air bubbles less likely. For these reasons, NOA-81 was chosen as the initial candidate material for device fabrication.

3.2.2 Fabrication

Replicating the fabrication protocol from [105], the work flow for the fabrication of NOA-81 devices is provided in **Figure 3-4**. To begin with, soft lithography was used to create SU-8 master molds (**Supplementary Note A.3**). PDMS was then cast

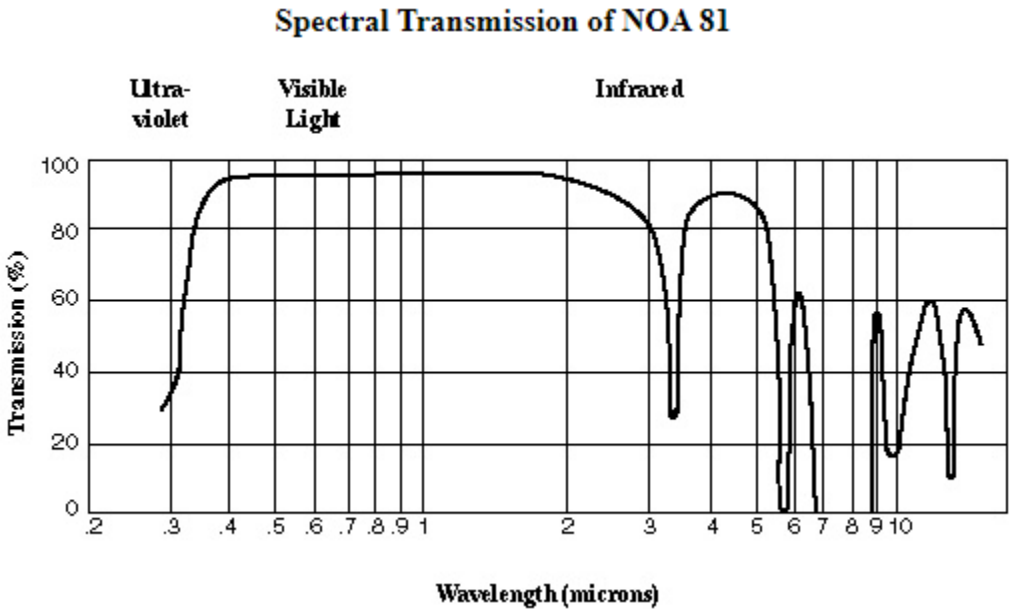

Figure 3-3: Transmission curve of NOA-81 following curing [104]

onto these molds to create PDMS replicate molds. Separately, PDMS wells of defined depth were fabricated and filled with a volume of NOA-81. The NOA-81 was then sandwiched between the replicate mold and the well bottom, and was exposed from above to UV light. Because of PDMS's native oxygen permeability, a thin layer of unpolymerized NOA-81 remained at all PDMS surfaces, allowing for the easy release of the replicate mold from the now polymerized NOA-81 device. The PDMS well is not removed as it is used to provide an easy way to handle the device coated in unpolymerized adhesive. Following replicate mold release, a glass slide is brought in contact with the small layer of unpolymerzied NOA-81 at the bonding surface of the NOA-81 device. The assembly is then briefly exposed to UV light from above in order to seal the device. The PDMS well is then removed, and the final device is then washed with acetone and isopropanol to remove any remaining unpolymerized NOA-81.

3.2.3 Fabrication issues and attempted solutions

The fabrication process proposed in the previous section was fraught with issues that were either left unfixed or were attempted to be fixed with limited success. To begin with, it was found that trying to produce ~250 micron thick SU8 molds was incredibly difficult and hard to reproduce. This was because the spin coating process (not unlike manual vitrification) was highly sensitive to operator errors. In order to obtain an SU8 layer of perfectly uniform thickness, it is imperative that the wafer center is precisely aligned with the spin coater's axis of rotation and that photoresist is deposited such that the axis of rotation is coincident with the center of the pool of photoresist. The impact of errors in centering become amplified as photoresist viscosity increases, which the author believes is a result of viscous forces dominating

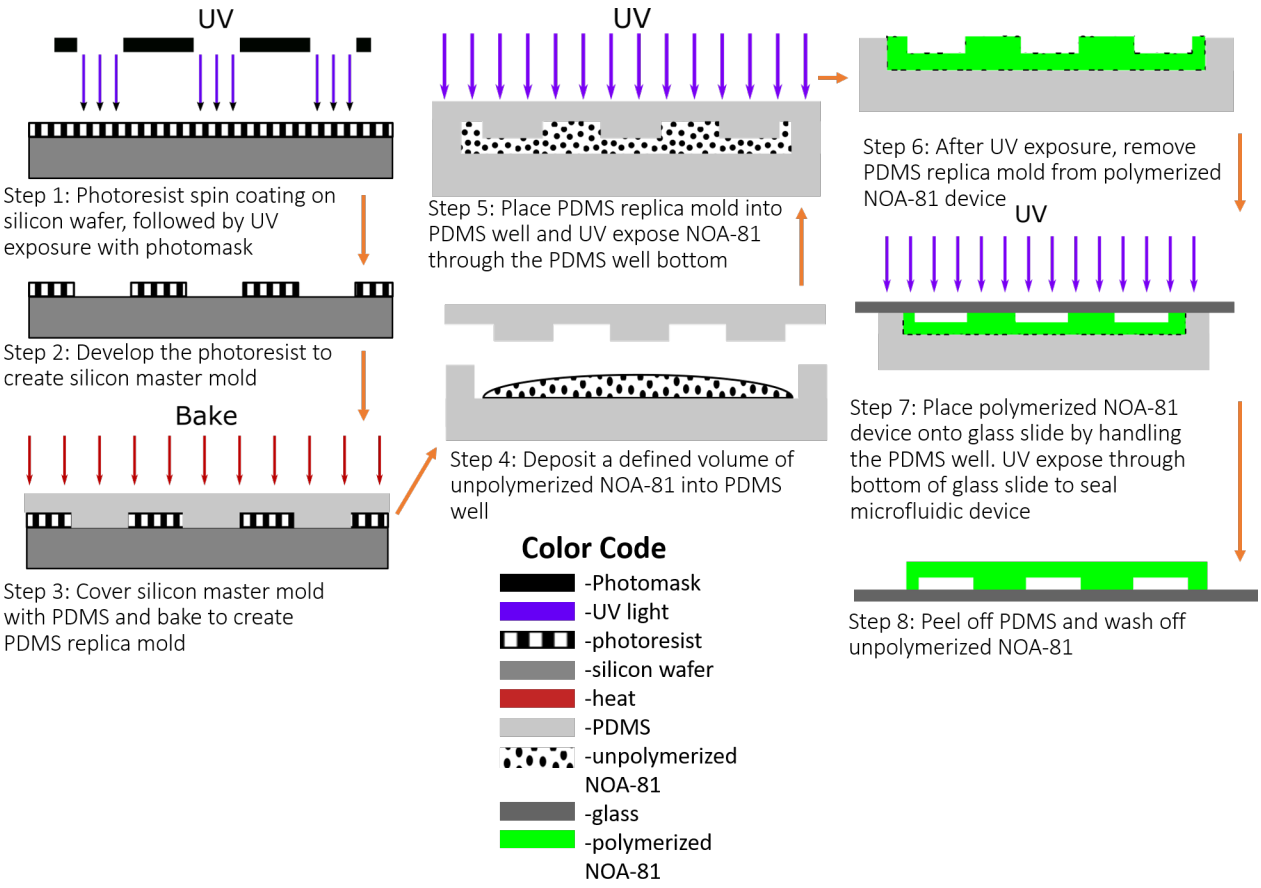

Figure 3-4: Detailed work flow describing the fabrication of NOA-81 devices. Orange arrows indicate the sequence of steps. Any modifications on this work flow in the fabrication of NOA-81 devices is described explicitly in the text.

over surface tension forces which act to reduce the film's surface-to-volume ratio and thus promote a uniform thickness across the film. The photoresist used, SU8 2150, is the most viscous photoresist offered in the commonly used SU8 2000 series of photoresists, with a dynamic viscosity of 6.46×10^4 cps [110], making it roughly six time the viscosity of honey. As a result, it was incredibly difficult to obtain a uniform thickness of photoresist across the wafer surface. This was verified by measuring the surface contours of the patterned photoresist following development using a surface profiler (Dektak 150, Veeco). These measurements, performed on five separate wafers, revealed features as short as 150 microns, and as tall as 370 microns. Differences in height were often observed to be linearly directional, indicating centering errors during photoresist spin coating. These issues were never resolved, and SU-8 molds were created until sections that were within 50 microns of the desired height of 250 microns happened to be fabricated.

Issues continued following the fabrication of SU-8 molds. While the creation of PDMS replicate molds and wells proved to be straightforward and high fidelity, casting of the NOA-81 proved to be incredibly challenging. The majority of these chal-

lenges stemmed from the fact that NOA-81 is hydrohilic while PDMS is hydrophobic. These differing material properties resulted in strong capillary forces that would inhibit NOA-81 from wicking into PDMS features, resulting in poor feature replication. This problem was particularly prevalent for features with high aspect ratios (ARs) (HMW slots), and device areas where the density of features was high (serpentine mixing channel). It should be noted that in the literature where NOA-81 is used as a microfluidic device material (see references for sec. 3.2.1), the AR of features is usually quite low (~0.1-0.5). Thus, while NOA-81 may be well suited for the replication of low AR features, it did not perform well in this application where all features have an aspect ratio greater than one.

There are several ways in which this issue tried to be ameliorated. One way was by introducing the unpolymerized NOA-81 to the replicate mold first, and applying vacuum until the PDMS mold was successfully penetrated. The rationale behind this was to decrease ambient pressure surrounding the device, with the hope of ultimately drawing air trapped inside the PDMS mold out of the device. However, this tended to make the problem worse; diffused oxygen in the PDMS mold transferred to the NOA-81 and, despite, being left in vacuum for over an hour, failed to be evacuated from the NOA-81, resulting in large air bubbles throughout the adhesive. This is likely a function of the strong surface tension forces present in unpolymerized NOA-81, which is the cause of the problem in the first place.

Recognizing that the application of vacuum would not work because of NOA-81's strong surface tension, it was then attempted to reduce its surface through the application of heat. To accomplish this, NOA-81 was deposited onto a PDMS mold, and was placed inside an oven at 80 °C for 20 minutes. However, this tended to result in strange pooling patterns in the NOA-81, to the point that large swaths of the replicate mold would become uncovered. It is likely that this was the result of phase separation, as this adhesive is a relatively complex compound consisting of relatively incompatible phases (photoinitiators, for instance, tend to be hydrophobic).

Recognizing that heating also would not help, it was attempted to increase the wettability of PDMS through plasma treatment. This actually did improve penetration of NOA-81 into the PDMS allowing for the successful replication of features in PDMS molds (inset of **Figure 3-5**). The issue, however, was that this often came at the cost of unpolymerized NOA-81 remaining stuck to the PDMS mold. Without this unpolymerized NOA-81, sealing of the device to a glass slide became difficult. To remedy this, the UV intensity was decreased to decrease the rate of free radical generation. The rationale behind this was that by decreasing the rate of free radical generation, oxygen present in the PDMS would be able to diffuse deeper into the polymerizing mold before binding to and quenching a free radical. However, for the UV intensities explored ($20\ \frac{\text{mW}}{\text{cm}^2}$ – $89\ \frac{\text{mW}}{\text{cm}^2}$), this effect did not reliably correlate to when the NOA-81 device would successfully bond to a glass slide and seal. Thus, there was no method by which NOA-81 devices could reliably replicate the features of PDMS molds and be easily sealed.

On top of these issues, for reasons that are still poorly understood, the NOA-81 often became yellow and hazy upon curing (**Figure 3-5**). This result was surprising, as it runs counter to the properties reported in sec. 3.2.1. When the author contacted

Norland Optical regarding this issue, the designing chemist attributed this effect to unreacted free radicals, and to remedy this issue, recommended leaving the molds out at room temperature for a few days. While this method seemed to reduce yellowing of the devices, the devices remained hazy and translucent. Recalling the requirement of device transparency for CPA concentration measurement, this issue would also need to be fixed in order to move forward with this material.

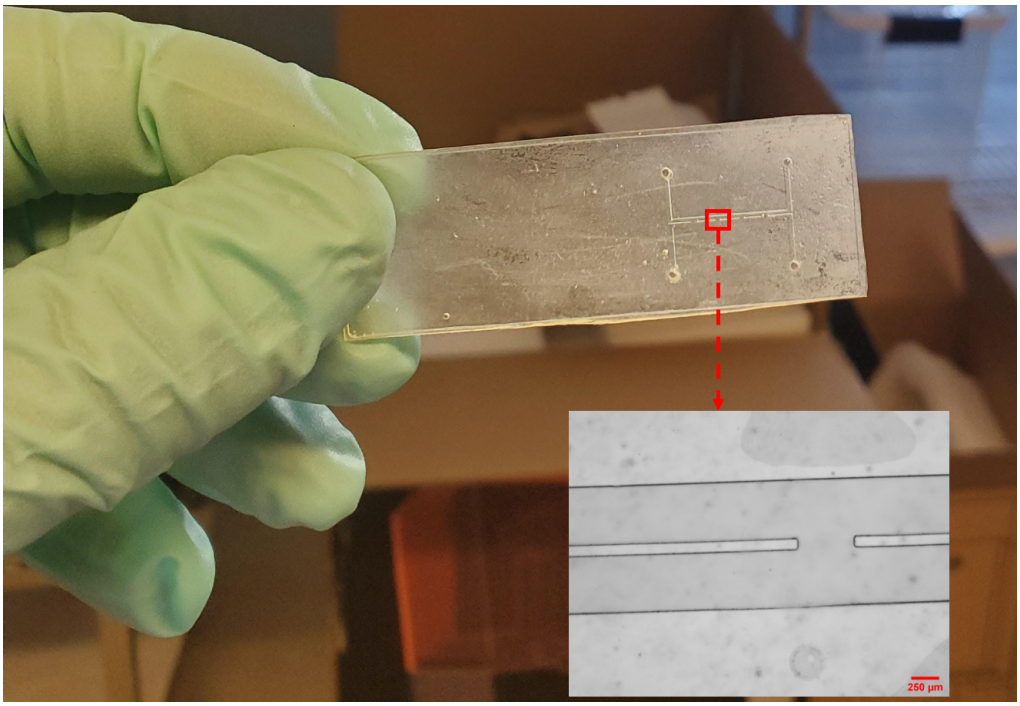

Figure 3-5: Sample NOA-81 molded device created with the assistance of PDMS mold plasma treatment, with close up of HMW slot (inset). This device was used as a test device for HMW fabrication. While it was possible to obtain reliable replication of PDMS molds, sealing of devices created with the help of plasma treatment proved challenging. Moreover, device yellowing and haziness negatively impacted optical properties, which would have made CPA concentration measurement very difficult.

In conclusion, while NOA-81 may be a useful prototyping material for short, low aspect ratio devices, for the proposed device, which has tall, relatively high aspect ratio features and requires a material with repeatable thickness and optical properties, NOA-81 cannot be used.

3.3 Cyclic Olefin Copolymer as a candidate device material

3.3.1 Background and Material properties

Cyclic Olefin Copolymer (COC) is a clear, (usually) amorphous polymer consisting of cyclic monomer chains copolymerized with ethylene. From a physical perspective,

COC closely resembles poly methyl methacrylate (PMMA) and polycarbonate (PC) [111]. As was reported for NOA-81, COC has excellent optical transparency across a wide range of wavelengths [112] (**Figure 3-6**).

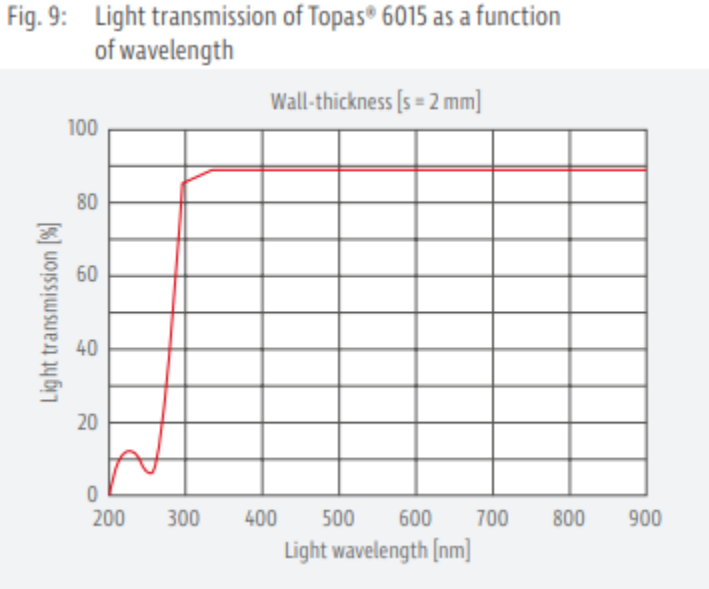

Figure 3-6: Sample transmission curve for a typical grade of COC. This particular grade of COC, TOPAS 6015, is clear and relatively temperature resistant [112].

Like NOA-81, COC has been shown to exhibit excellent biocompatibility [113,114] and long term stability in surface treatments [111]. COC has also been shown to be highly oxygen impermeable, with common grades of the material being ~1000 times less oxygen permeable than PDMS [115, 116]. Unlike NOA-81, COC tends to be highly hydrophobic, which makes device operation and channel wetting more difficult. However, both short and long term (>28 days) hydrophilicity has been shown to be induced through simple procedures such as exposure to oxygen plasma [113, 117]. Advantages of COC over NOA-81 is its compatibility with a number of fabrication methods such as micromilling, hot embossing, injection molding, and laser ablation [111]. This makes production scale up with COC devices straightforward, which would not be the case for a more lab-based method like NOA-81 molding. Moreover, while all these machining operations are also compatible, to some extent, with other thermoplastics, COC is unique in its high flowability and relatively low and tunable range of T_g, being anywhere from 80 °C to 180 °C [112]. This has spurred the advent of rapid microfluidic prototyping in COC, where, for injection molding, rapidly fabricated PDMS molds are being used instead of costly, difficult to fabricate aluminum or steel ones [118]. Rapid prototyping of COC microdevices has also began to garner attention in the field of ART as a platform for the automated culturing and maturation of oocytes, where hot embossing is used to manufacture devices [114]. With all this in mind, COC was chosen as a candidate material for device fabrication.

3.3.2 Fabrication

Fabrication of COC prototypes was performed using micromilling. This method was chosen because of its simplicity, reliability, speed, and amenability to rapid design changes. The work flow for the fabrication of COC devices is provided in (**Figure 3-7**).

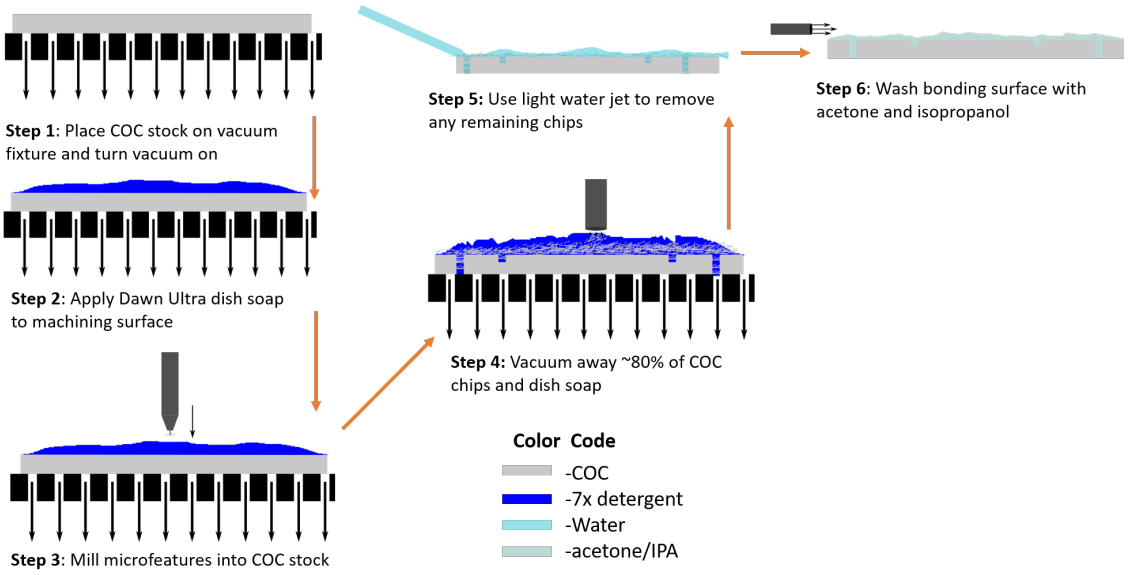

Figure 3-7: Work flow describing the micro milling of COC devices. Orange arrows indicate the sequence of steps.

To begin, a microscope slide size piece of Topas COC stock, measuring 25.5 mm x 75.5 mm x 1 mm was removed from its packaging (microfluidic ChipShop, Jena, Germany). The stock was then fixtured inside a benchtop micromilling CNC machine: Othermill Pro (Bantam Tools, Peekskill, NY). Because the features to be machined have tolerancing on the order of tens of microns, the mode of fixturing proved to be an important factor in successful fabrication. Ultimately, vacuum fixturing was found to produce the best results by securing the stock to the milling bed by static friction, thus eliminating relative motion between the two. Dawn Ultra dishwashing liquid (Procter and Gamble) was then applied liberally to the machining surface in order to act as a coolant and dissipate heat generated during the machining process. Device design and GCode generation were performed using AutoDESK Fusion. It should be noted that all COC milling operations were performed using conventional (as opposed to climb) milling because of the material's inherent ductility and flowability. These properties make COC chips relatively "sticky", necessitating the use of of the more aggressive conventional milling strategy to effectively evacuate the chips during fabrication and reduce the prevalence of burrs [119].

After milling has been completed, a wet vacuum is used to remove the majority of chips generated during the CNC machining process. Chips that remain usually reside in the features of the device, and are removed using using a lightly pressurized

water jet. The device is then sprayed with acetone and isopropanol, and is dried using compressed air.

A sample device fabricated using the described workflow is shown in **Figure 3-8**. It can be observed immediately that the optical quality of COC is far superior to that of the NOA-81 device shown in **Figure 3-5**, meeting the criteria of optical clarity for CPA concentration measurement. Moreover, the achieved device resolution meets the design specifications outlined in **Table 3.1**; channels with a minimum width of ~250 microns and a minimum spacing between channels of ~125 microns were able to reliably fabricated. Thus, it can be concluded that COC micromilling is a viable fabrication technique for this application.

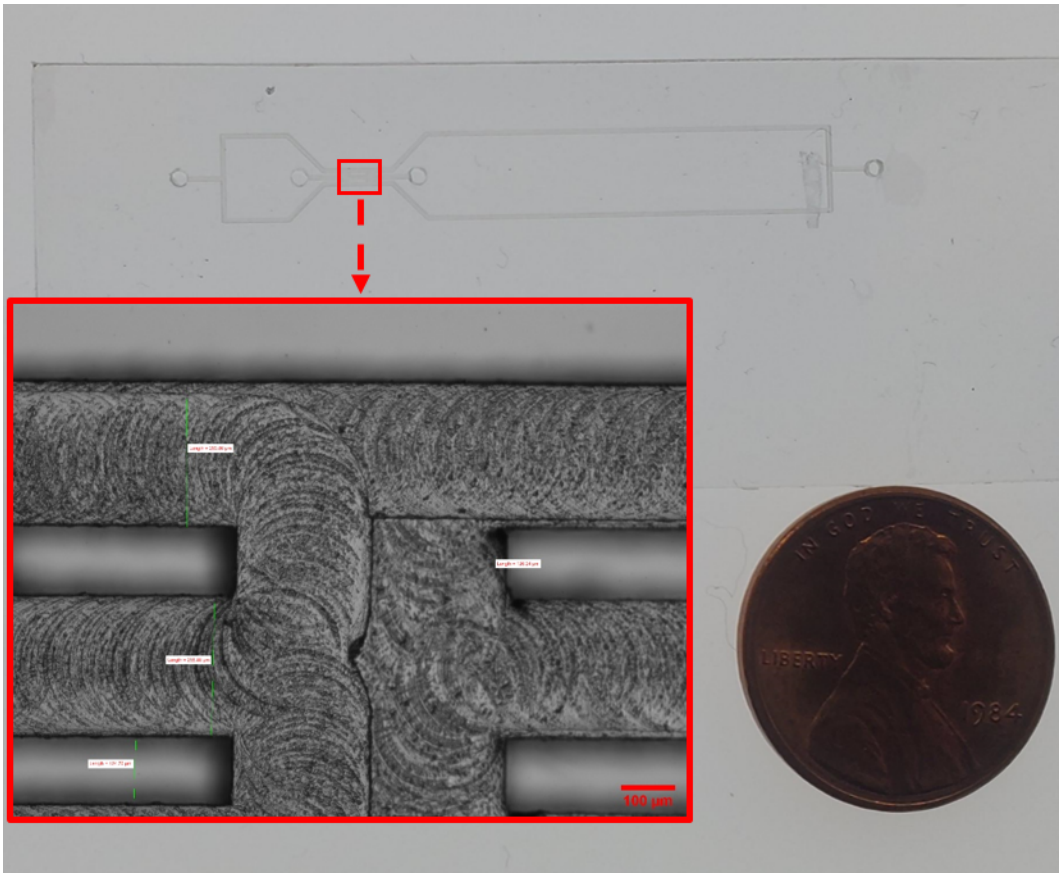

Figure 3-8: Sample milled COC device with close up of HMW slot (inset). This device was used as a test device for HMW fabrication. Using the described fabrication method, it was possible to reliably manufacture microfluidic channels with a minimum width of ~250 microns and a minimum spacing between channels of ~125 microns. The circular patterns seen in the inset image are created as the milling tool removes material from the COC stock. This machining process took ~30 minutes to complete, with minimal user intervention following initiation of the CNC program.

3.3.3 Sealing of COC devices

Sealing of COC devices proved to be a nontrivial task. In the literature, there are three primary methods of COC device sealing: thermal bonding [114, 120], adhesive bonding [121], and solvent bonding [118, 122]. Thermal bonding relies on the use of heat, pressure and time to form an irreversible bond between two COC substrates. The working principle behind thermal bonding is by heating the substrate at or slightly below its T_g, diffusion of polymer chains is encouraged. If this diffusion of polymer chains is encouraged while the two substrates are in pressurized contact, then, over time, polymer chains from either substrate will diffuse into one another, creating a strong, irreversible bond. While this is a reliable method of COC bonding, the process is highly sensitive to the bonding temperature, pressure, and time, values that need to be modified from COC grade to COC grade, and from device to device. The process is also highly sensitive to parallelism of bonding surfaces, and can result in device cracking if the two surfaces are misaligned (**Figure 3-9a**).

Adhesive bonding simply involves the use of a double-sided adhesive layer to join two COC substrates. Adhesive bonding is simple, fast, versatile, and robust to errors in protocol. The main challenge with adhesive bonding is that, often, the toxicity and biocompatibility is usually poorly understood. Moreover, as this application needs to avoid sticking of oocytes to device surfaces, it does not seem prudent to have an entire device surface consist of an adhesive. While the stickiness of the adhesive could potentially be mitigated with a surface treatment, this complicates the fabrication process and would require time and resources to resolve.

Solvent bonding, like thermal bonding, attempts to bond two COC substrates by promoting diffusion of polymer chains from either substrate into one another. However, this is achieved through the use of nonpolar, organic solvents (e.g. cyclohexane) as opposed to heat. These solvents penetrate into the COC disrupting the network of bonds between polymer chains. This results in a fluidization at the COC surface that, when put in contact with another COC substrate, allows polymer chains to diffuse from one substrate into another, forming the desired irreversible bond. Solvent bonding can be combined with light heat and pressure treatment to increase bonding strength. The primary challenge in solvent bonding is determining the optimum exposure conditions for the solvent. If the exposure is too low, then this compromises the integrity of the bond. If the exposure is too high, then, following bonding, this excess of solvent will attempt to diffuse through the now bonded COC interface. This results in gas bubble formation at the bonded interface, which negatively impacts optical quality and reduces bond strength (**Figure 3-9b**). Thus, like thermal bonding, successful solvent bonding requires careful optimization that will change from COC grade to COC grade, and from device to device.

To overcome the disadvantages of these sealing methods, the Griffith Lab has developed a new method of sealing COC devices by utilizing Topas Elastomer E-140 (E-140). Developed in 2010, this elastomer has been shown to be safe and biocompatible, and has already received FDA clearance for use in medical applications [123]. Unlike other grades of COC, E-140 has a semi-crystalline structure, giving it the mechanical properties of a flexible elastomer. This semi-crystallinity makes E-140 more

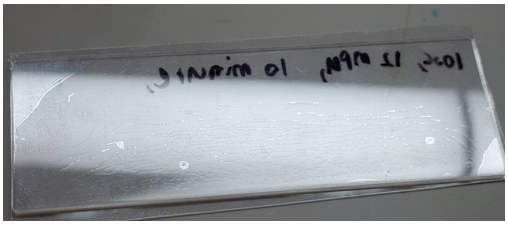

(a) Cracks in sealing COC film during thermal bonding process as a result of nonparallel layer alignment.

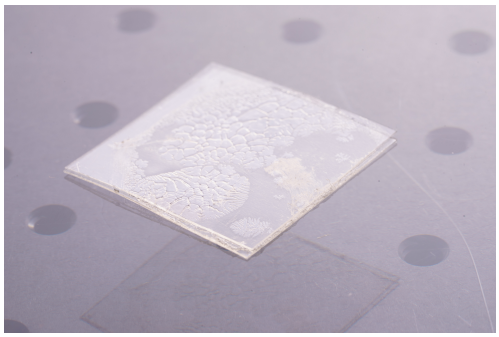

(b) Bubbles forming at solvent bonding interface as a result of excess solvent exposure. This photo was borrowed, with permission, from the work of Duncan Allison O'Boyle (unpublished).

Figure 3-9: Challenges of different methods of conventional COC device sealing.

oxygen permeable than other, amorphous grades of COC by a factor of ~100 (this is still ~30 times less permeable than PDMS) [124]. It was found through in-house experimentation that, when treated with oxygen plasma, reactive chemical groups form at the elastomer surface. These chemical groups were then able to form strong bonds with polymer chains present on amorphous COC surfaces. It was this property of E-140 that was leveraged to seal COC devices.

The work flow of this sealing method, colloquially referred to as the "elastomer sandwich method", can be found in **Figure 3-10**. To begin, a piece of 140 micron thick Topas COC film (microfluidic ChipShop, Jena, Germany) was cut to have planar dimensions slightly larger than those of the fabricated COC device (~40 mm x ~90 mm). A piece of E-140, with thickness 127 microns, was cut to roughly the same dimensions as the COC film. Both films have protective films, as shown at the top of **Figure 3-10**, to aid with handling and protect from surface scratches and dust. One protective film was then removed from the COC film, and the bonding surfaces of the COC film and E-140 were sprayed with acetone and dried with compressed air. After cleaning, both the E-140 and COC film were placed in a PDC-001 plasma cleaner (Harrick Plasma, Ithaca, NY) on "HI" setting (30 W) for 45 seconds [125]. This time was determined, through trial and error, to sufficiently create reactive species at the E-140 surface, without impacting the elastomer's bulk properties. Excess plasma treatment was found to make the E-140 stiff. After plasma treatment, the E-140 surface was gently brought into contact with the COC film surface, being careful to avoid wrinkling of the E-140 surface and trapping of large pockets of air. A cell lifter (Corning, Corning, NY) was then used to ensure conformal contact between the surfaces, and force out any air bubbles that may be present. Note that, because of the E-140's protective film, the elastomer was protected from scratching during treatment with the cell scraper. This "COC window" was then placed onto a hot plate at 72 °C for 10-15 minutes to strengthen the plasma bond. After heating, the protective film of the E-140 is removed from the COC window. The COC window and milled

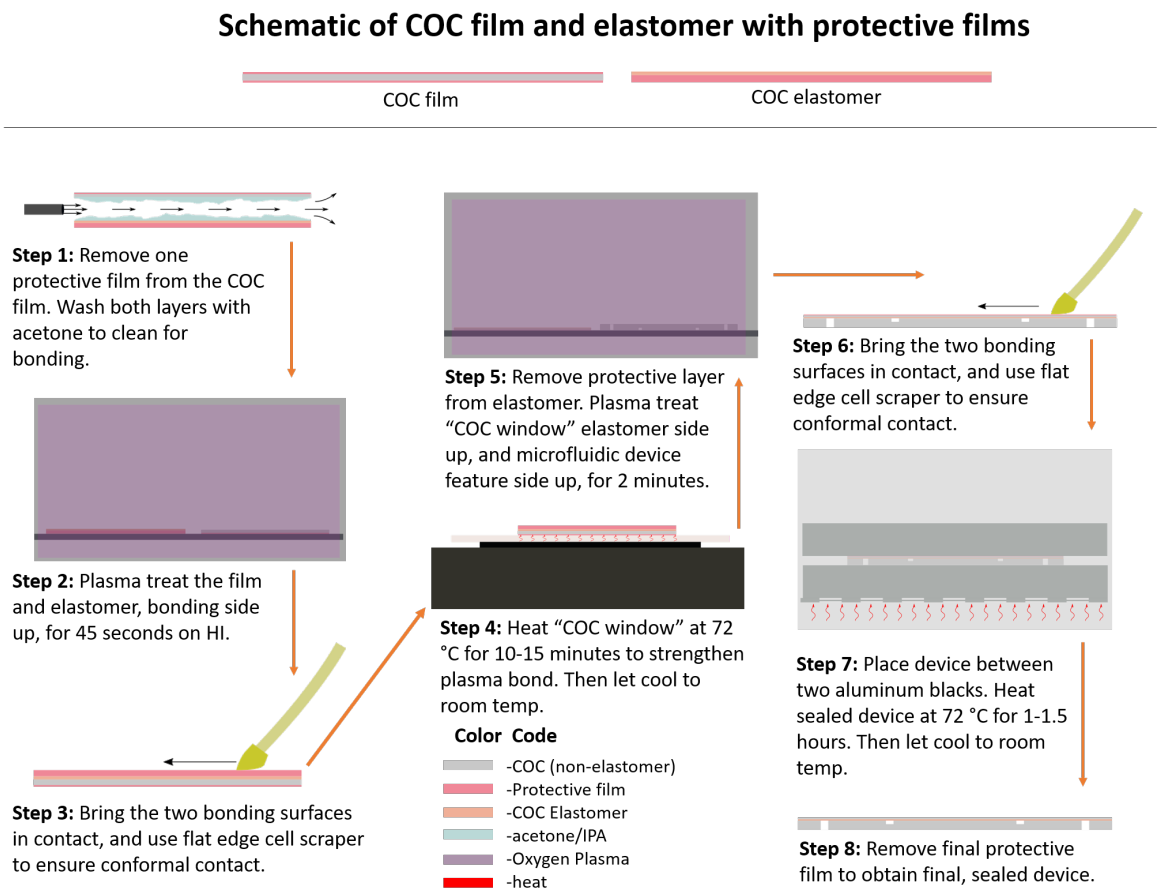

Figure 3-10: (top) Schematic of the COC film and COC elastomer with protective films (bottom) Work flow describing the sealing of COC devices. Orange arrows indicate the sequence of steps.

COC device are then placed bonding side up inside the PDC-001 plasma cleaner on the "HI" setting (30 W) for 2 minutes. Similar to before, the COC window is then gently brought in contact with the COC device, and a cell scraper is used to ensure conformal contact between the COC window and the COC bonding surface. The entire assembly is then place between two, flat aluminum blocks, and is placed inside an oven set at 72 °C for 60-90 minutes. Following heating, the device is then allowed to slowly cool to room temperature to prevent delamination of the COC window due to sudden thermal stresses. Once cooled, the final protective layer is removed from the device film and the overhangs of the COC window are removed using a scissors and scalpel.

The primary advantage of this method is its simplicity and robustness. The parameters described here are applicable to all COC devices, regardless of their design. Moreover, unlike most adhesives, E-140 has already been approved for use in medical devices, and will likely not stick as much to oocytes by virtue of the fact that it is not designed to be naturally sticky. One potential shortcoming of this bonding technique for this application is the enhanced oxygen permeability of E-140. However, as the

free surfaces of E-140 have a total area of ~25 mm^2 and are located at the extremities of the device, far away the region of HMW fabrication, the impacts of oxygen diffusion through the E-140 are expected to be minimal. Even if this did prove to be a problem, these avenues for oxygen diffusion could be blocked by covering the sides of the device in a more oxygen impermeable material. However, as will be shown later on, these measures are unnecessary.

3.3.4 World-to-chip connection

When using PDMS as a microfluidic material, obtaining a simple world to chip connection is a given. This is because the elastomeric properties of the PDMS provide a built in seal when making fluidic connections. When using a non-elastomeric material like COC, this process becomes more challenging. Originally, the use of PDMS as a gasketing material was attempted. The molded and hole punched PDMS gasket was attached to the top surface of the sealed COC device via plasma bonding, and was used in creating leak-free fluidic connections.[1] This bonding did not, however, prove to be reliable, and resulted in highly leaky connections. A PDMS gasket was then used in conjunction with a screw clamping mechanism to secure the the PDMS to the top of the COC device. However, due to the rigidity of the tubing used, it was not uncommon for the tubing to simply pop out from the relatively weak elastic forces maintaining them inside the PDMS. Ultimately, it was found that micromilling could be used as an effective tool in creating a reliable world to chip connection. The process flow for the creation of this world to chip connection is shown in **Figure 3-11**.

The process begins by machining an interfacing “tube holder" from acrylic in a fashion similar to the one described in **Figure 3-7**. A design for this tube holder can be found in **Supplementary Note A.4.** This tube holder featured holes needed to make the world-to-chip connection, and a slot that was meant to act as a window for CPA concentration measurements. This CPA measurement window was designed to align with the HMW fabrication region, and was toleranced such that minor misalignments could be permitted. The key to ensuring a strong, leak-free world-to-chip connection was by creating a chamfer at the top of the through hole, and making the minimum through hole diameter of the acrylic slightly smaller than the outer diameter of the tubing. The chamfer was needed to provide compressive radial forces to help the tube enter the through hole, and the through hole diameter was chosen to allow tubing to enter the through hole while maintaining compression on the tubing. Through trial and error it was determined that the through hole could only be made 25 microns (the resolution of the Othermill Pro) smaller than the outer diameter of the tubing used before the tubing would not penetrate the through hole. Though this reduction might seem slight, the results were fantastic; manual removal of the tubing from the hole required a fair deal of pulling, indicative of a strong frictional seal.

Tubing was then inserted into the tube holder. NOA-81 was used to fill the chamfers in the tube holder, and was polymerized to further secure the fluidic connection.

[1]It occurs to the author now that E-140 could be used as an effective gasketing material for COC devices. However, as the material comes most often as a thin ~125 micron film, it’s direct application as a gasketing material requires some thought

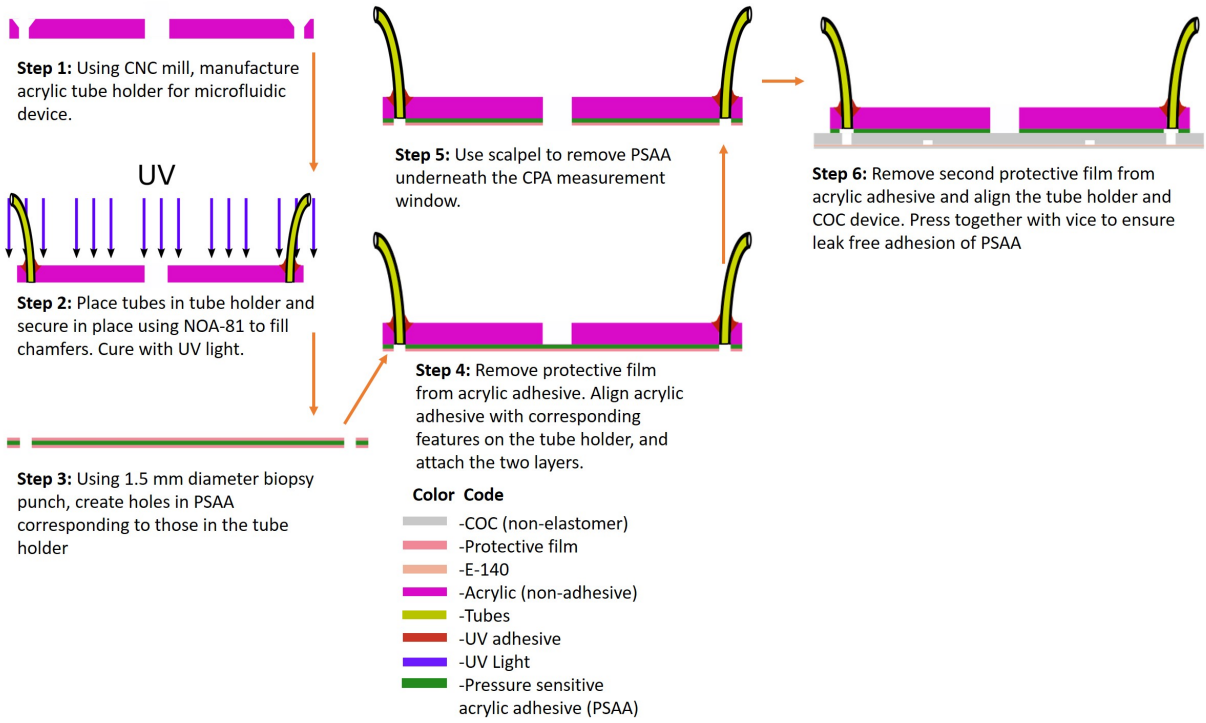

Figure 3-11: Work flow describing how the world to chip connection was made for COC devices. Orange arrows indicate the sequence of events.

Holes corresponding to those in the tube holder were then manually punched out of a thin, double sided, sheet of pressure sensitive acrylic adhesive (PSAA) using a 1.5 mm diameter biopsy punch (Integra Milltex). One of the PSAA's protective films was removed, and the PSAA was carefully aligned and attached to the tube holder. A scalpel was then used to remove the PSAA located below the CPA measurement window. The PSAA's other protective film was then removed, and was aligned and attached to the top of the COC device. A toolmaker's vise was used to press the entire assembly together, which mainly served to strengthen the bond between the PSAA COC.

3.4 Final Device

A sample device created using the described processing techniques is pictured in **Figure 3-12**. It's high optical clarity and layers of defined thickness evince the benefits of micromilling optically clear thermoplastics for this application. Moreover, the world-to-chip connection used was able to maintain flow of at least 50 $\frac{\mu L}{min}$ in devices without the occurrence of leaks at fluidic ports. Thus, through extensive testing and failure, a defined method for the fabrication of microfluidic devices that meet the criteria outlined in section 3.1 was established. Moreover, if NOA-81 was chosen as the preferred material of prototype fabrication, fabrication would be limited to replica molding. Replica molding has been shown to have minimal scale up potential [126],

relegating it to uses mainly in academia. COC, on the other hand, is amenable to a wide range of large scale fabrication techniques, making the eventual consideration of scaling up production after prototype validation a simpler one to resolve.

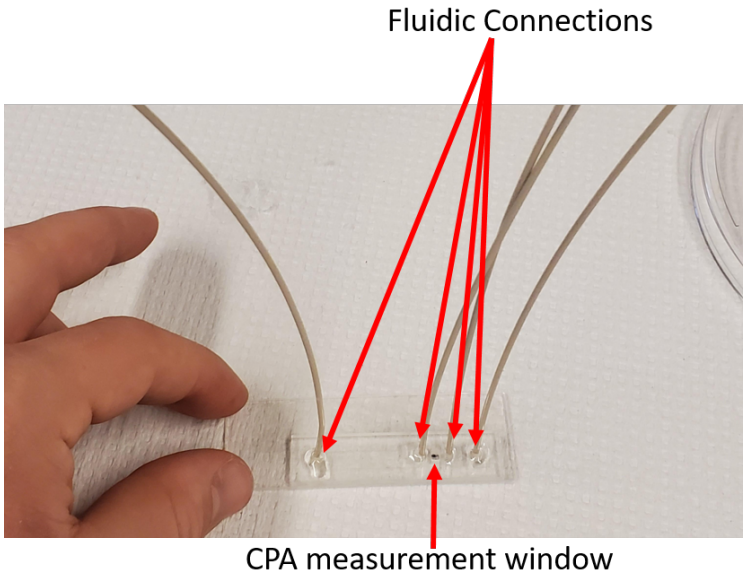

(a) Isometric view

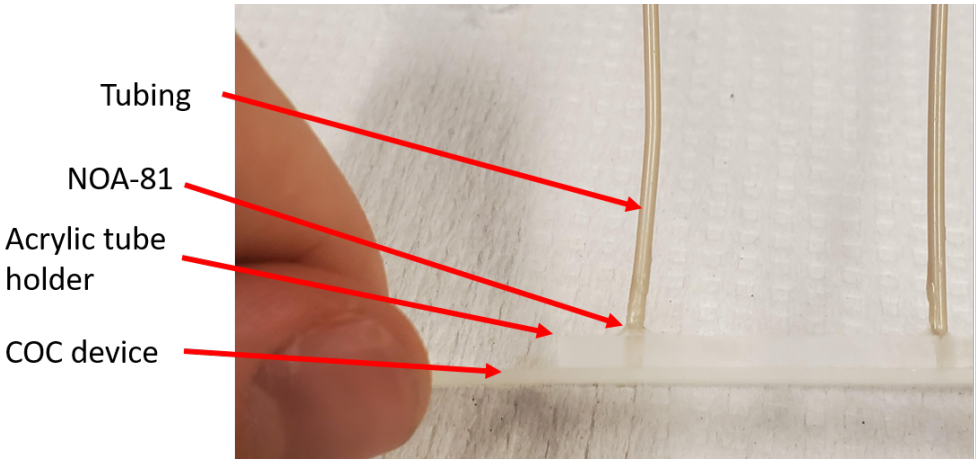

(b) Side view

Figure 3-12: Labelled views of a completed COC device.

Chapter 4

Hydrogel microwindow (HMW) fabrication

4.1 Background

4.1.1 UV Projection for HMW fabrication

HMWs, as discussed in sec. 2.2, are thin hydrogel membranes that are manufactured *in situ* in a microfluidic device. They possess the unique property of being a diffusion permitting convection barrier. Moreover, it was determined in sec. 3.1 that, for this application, HMWs were to be manufactured using UV patterning due its simplicity and high resolution capabilities. However, the way in which this UV patterning was to be achieved, and the composition of the HMWs have yet to be discussed.

Traditionally, UV patterning for HMW fabrication has been achieved using microscope projection lithography (**Figure 4-1a**) [82, 95] (MPL). This method is similar in spirit to soft lithography; by using a UV light source and a photomask (similar to the one shown in **Figure A-1**), one can reliably project and position microscale UV patterns onto an area. While simple and inexpensive to use, this method is not amenable to rapid prototyping of different UV patterns. Photomasks are static and cannot be altered once they are manufactured. Moreover, the intensity of UV light hitting an area of interest is binary by design; UV light either hits a region or does not, making the production of intermediate illumination states impossible.

Recently, more advanced methods of HMW fabrication have been realized by using laser scanning confocal microscopy (LSCM) (**Figure 4-1b**) [99]. This method polymerizes HMWs through the use of a rastering laser. By controlling the laser speed and rastering path, controlled, microscale UV exposure to a microdevice can be achieved. This method improves upon MPL by replacing a static photomask with a dynamic scanning mirror, providing the ability to rapidly prototype with different UV patterns. Moreover, pulse width modulation (PWM) of the laser could be used to change the local exposure intensity, allowing the production of intermediate

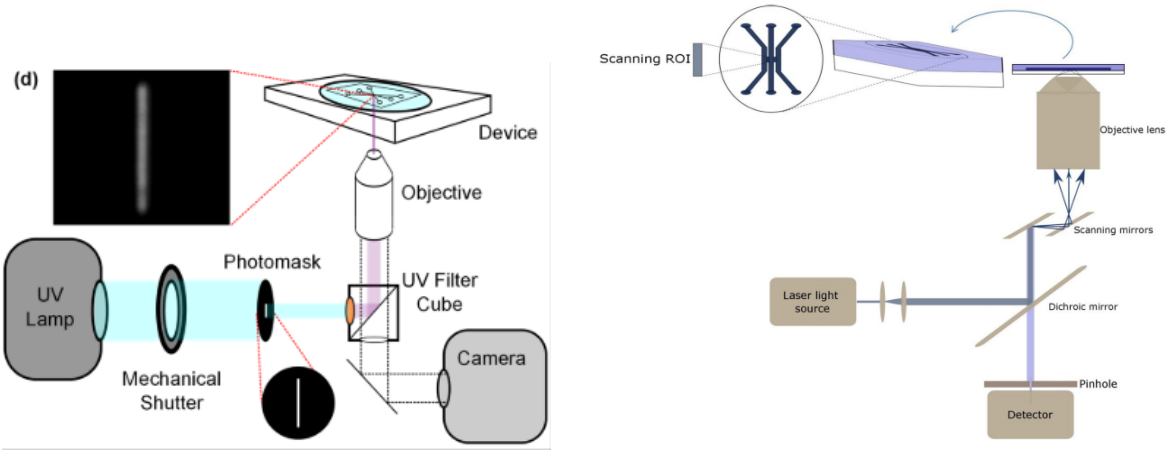

(a) Schematic drawing of HMW fabrication using microscope projection lithography [82].

(b) Schematic drawing of HMW fabrication using laser scanning confocal microscopy [99].

Figure 4-1: Schematics for different methods of UV patterning in HMW fabrication.

illumination states. This method, however, requires the use of a confocal microscope, which is expensive and complicated to acquire, use, and repair if necessary.

High resolution UV patterning is not only of interest for HMW production. For decades, researchers in the field of additive manufacturing have been investigating how to create high resolution UV patterns for the selective polymerization of photoactive resins [127]. To this end, a prominent researcher in this field, Prof. Nicholas Fang of MIT, developed projection micro stereolithography (PμSL) [128]. Like MPL, PμSL uses a UV lamp as its illumination source. However, instead of using a static photomask to achieve high resolution UV patterns, a digital micromirror device (DMD) is used. A DMD is an array of micromirrors that can take on one of two binary states; when a micromirror is "on", it reflects a small portion of the incident UV light towards the target of interest, and when it is "off", it does not. These micromirrors can toggle between these two states relatively quickly allowing for the realization of intermediate illumination states through PWM. Quality DMDs are available at a fraction ($\sim 10^{-2}$) of the cost of confocal microscopes, making them easily replaceable if necessary, and are very easy to use and program. Thus, using PμSL for HMW fabrication merges the versatility and dynamic nature of LSCM with the simplicity and cost effectiveness of MPL.

4.1.2 Selection of Polethylene Glycol (PEG) for HMW Fabrication

Selection of an appropriate hydrogel was crucial to successfully fabricating HMWs for this application. From the discussion thus far, it is clear that the selected hydrogel needed to be UV polymerizable, biocompatible, and have easily tunable mechanical and diffusive properties. Moreover, to ensure platform reliability, these properties

needed to be repeatable from device to device. Drawing upon the Griffith's lab extensive prior work with polyethylene glycol (PEG) hydrogels [129–131], it was determined that PEG hydrogels met all the described requirements, and were thus ideal for this application.

PEG consists of a long, linear chain of repeated ethanol subunits (**Figure 4-2a**). In order to form a UV polymerizable hydrogel, PEG molecules need to have functionalized end groups that, with the assistance of other molecules, bind to one another in response to UV light. This binding of end groups ultimately results in a crosslinking of PEG molecules, creating a large, nanoporous mesh. Water is then driven into the mesh by hydrophlic/hydrophobic interactions and osmotic gradients, forming what is called a PEG hydrogel.

There are two primary strategies for binding PEG molecules together to form a hydrogel. The first method, known as chain polymerization, involves the the linking of functionalized, linear PEG molecules, such as PEG diacrylate (PEGDA) (**Figure 4-2b**), together through free radical chain polymerization (the following video provides an excellent animation illustrating the process) [132]. Chain polymerization begins by mixing together "photoinitiators" with functionalized PEG molecules dissolved in water. Upon exposure to UV light, photoinitiators are cleaved and form highly reactive, free radical species in a process called "initiation". These free radicals abstract electrons from the pi bonds of double bonded carbon atoms in order to stabilize themselves, in the process leaving one of the carbon atoms with a free lone electron. This carbon atom then abstracts another electron from a different pi bond to stabilize itself, and this process of "propagation" repeats itself until two or more of these growing chains of bonded PEG molecules meet. In this case, the free lone electrons from each growing chain stabilizes one another in a process called "termination". This process continues until all reactive species have been terminated, and no free electrons remain. The random, uncontrolled nature of chain termination tends to result in hydrogels with a more heterogeneous structure and mesh size (**Figure 4-2d**) [133].

The second method of creating UV polymerized PEG hydrogels, known as step growth polymerization, involves the linking of functionalized, multi-armed PEG molecules (**Figure 4-2c**) together using "click chemistry" [134]. Step growth polymerization, like chain polymerization, involves the combination of water, photoinitiators, and functionalized PEG molecules. However, step growth polymerization also requires the addition of "crosslinker" molecules to this mixture. Like chain polymerization, step growth polymerization begins with the formation of free radicals resulting from the cleavage of photoinitiators. These free radicals then abstract the electrons from pi bonds, most commonly present on the functionalized PEG arms, resulting in reactive atoms with free lone electrons. Crosslinker molecules then conjugate with two or more PEG arms, binding them together. This process continues until all crosslinker molecules have been conjugated. The novelty of step growth polymerization is that reactive PEG species do not react with one another, and can only be bound together via a crosslinker. This circumvents the problems inherent in relying on termination as a reaction end point, affording the user more control over the structure and mesh size of the resulting hydrogel (**Figure 4-2d**) [133].

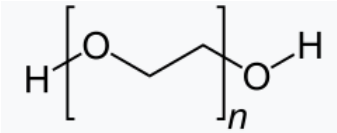

(a) Structural formula of polyethylene glycol (PEG).

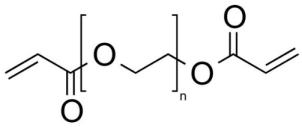

(b) Structural formula of PEG diacrylate (PEGDA). During chain polymerization, the carbon-carbon double bonds located at the molecule ends are opened up by free radicals, resulting in the creation of carbon atoms with free lone electrons. These carbon atoms will open up the double bonds of other PEGDA molecules, until two growing chains terminate each other.

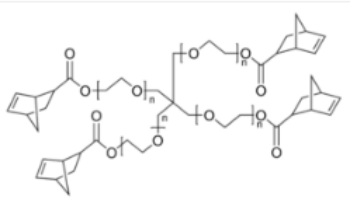

(c) Structural formula of 4-arm PEG with norbornene end groups. During step growth polymerization, the carbon-carbon double bonds located at the molecule ends are opened up by free radicals, resulting in the creation of carbon atoms with a free lone electron. These carbon atoms will react with crosslinker molecules, which will in turn bind the PEG molecules together in a network.

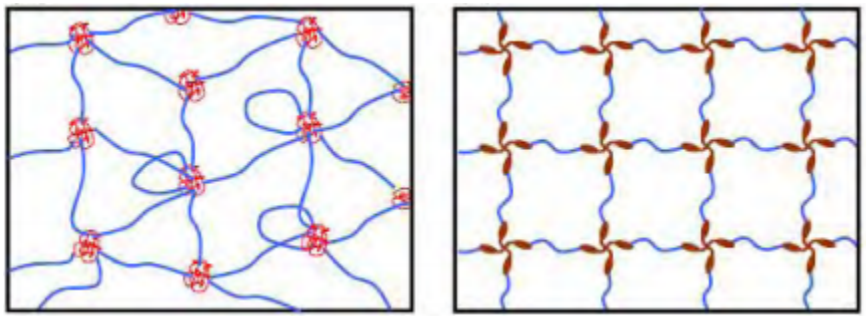

(d) Differences in mesh structure between chain polymerized PEG hydrogels (left) and step growth polymerized PEG hydrogels (right)

Figure 4-2: (top row) Structural formulas of polyethylene glycol (PEG) and its functionalized forms. (bottom row) Differences in mesh structure between chain polymerized and step growth polymerized PEG hydrogels.

It is unclear what effect the differences in chain polymerized and step growth polymerized mesh structure have on diffusion of small molecules such as CPAs. However, most likely owing to its relative simplicity, chain polymerized PEG hydrogels have traditionally been used in the creation of HMWs [82, 95, 99]. For this reason, it was decided that fabrication of HMWs via chain polymerization was a good starting point for HMW fabrication, with the knowledge that the Griffith Lab's expertise in designing step growth polymerized PEG hydrogels could be called upon later on if need be.

4.2 Experimental Setup

4.2.1 UV Projection, Visualization, and Microfluidic Operation

A picture of the set up for UV projection, device visualization, and microfluidic operation is shown in **Figure 4-3**, and a schematic of the system's optics is shown in **Figure 4-4**.[1] UV light was generated using a CBT-39-UV LED centered at 405 nm (Luminus, Sunnyvale, CA). This LED was embedded inside a PRO4500 light engine (Wintech, San Marcos, CA) in order to pattern the UV light appropriately. Light was patterned by controlling a DMD internal to the PRO4500 light engine. The PRO4500's DMD consists of a 912 x 1140 array of 7.6 μm x 7.6 μm pixels arranged diagonally (**Supplementary Note A.5**). To program the DMD, simple gray scale images were generated using Processing and were uploaded to the PRO4500 light engine through the use of the DLP Lightcrafter 4500 software (Texas Instruments, Dallas, TX). Projected UV light from the PRO4500 then passed through a collimating tube before entering the Olympus IX71 microscope (Olympus). The collimated UV light was then split by an 80:20 beam splitter (Thorlabs, Newton, NJ), which was used to allow simultaneous projection and visualization of the UV pattern. Reflected light was redirected upwards where it passed through the objective and reached the microfluidic device residing on the microscope stage. A portion of this light was then reflected, recollected by the objective, and transmitted through the beam splitter. This light was then focused by the tube lens and directed towards the MU300 CMOS camera (AmScope) for visualization.

Device visualization began by choosing an appropriate light source for illumination of the microfluidic device during HMW fabrication. Initially, transmission illumination of a broadband white light was used to visualize the device. However, as the hydrogel is light sensitive, this would result in unwanted hydrogel polymerization within the device channels. To remedy this, a 500 nm highpass filter (Thorlabs, Newton, NJ) was installed to filter the white light prior to it reaching the microfluidic device. This transmitted light would be focused by a condenser, and directed towards the microscope stage to illuminate the COC device. Light transmitted through the

[1] The optical setup was entirely inherited from Nicholas Fang's Lab Group at MIT, and was the product of a past Master's student [135]. Since the publication of the Master's, however, this set up has undergone some modifications.

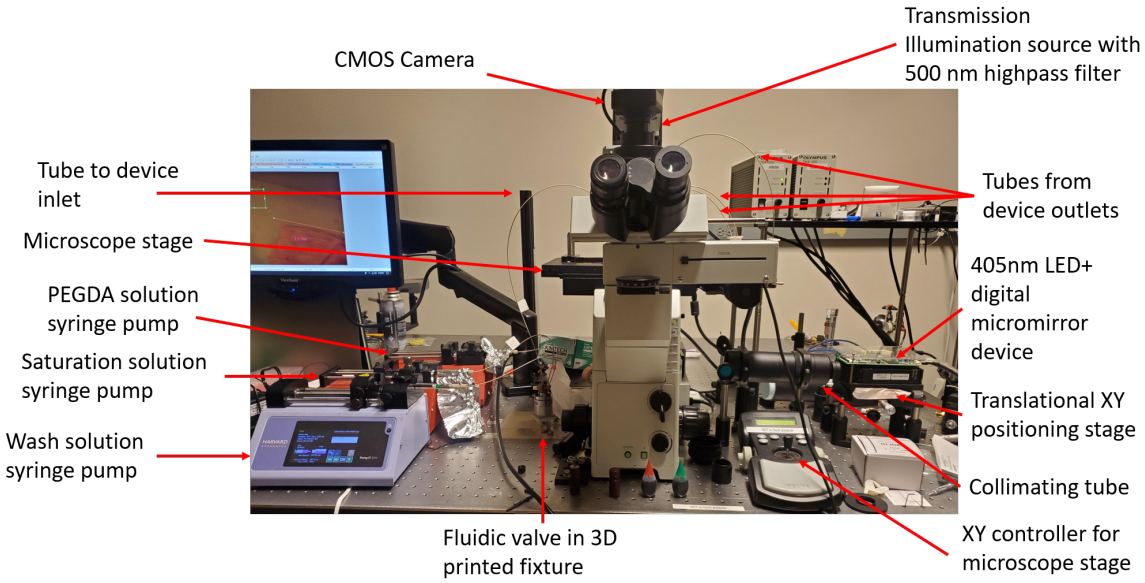

Figure 4-3: Picture of the experimental setup for HMW fabrication experiments. All components related to UV projection, device visualization, and microfluidic operation are shown.

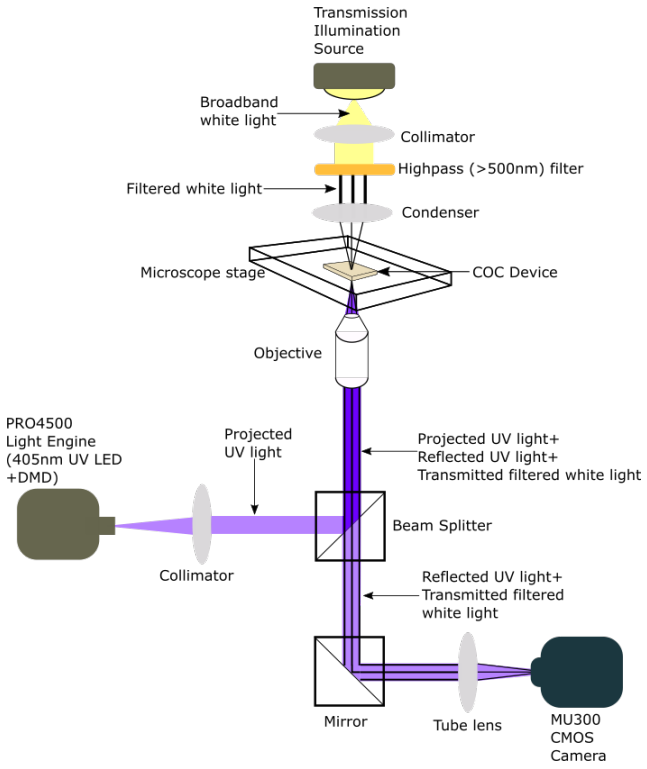

Figure 4-4: Schematic of the optical system used for UV projection and device visualization.

device would be captured by the objective and sent to the MU300 CMOS camera for visualization.

Microfluidic device operation was achieved through manual control of three separate syringe pumps (two syringe pumps were NE-300 "Just Infusion" pumps from New Era Pump Systems Inc., Farmingdale, NY, and one syringe pump was a PHD 2000 Programmable pump from Harvard Apparatus, Holliston, MA). Each syringe pump controlled a single, 1 mL gastight syringe (Hamilton, Reno, NV). These syringes were then connected to polyether ether ketone (PEEK) tubing (IDEX Health and Science LLC) via a Luer lock connection. Tubing had an internal diameter of 250 μm and an outer diameter of $\frac{1}{16}$". This tubing was then loaded into a six-to-one analytical selector valve (IDEX Health and Science LLC) that was manually operated to determine which solution entered the microfluidic device at a given time. This valve was added to the fluidic setup because it allowed for solution introduction to be limited to a single fluidic connection on the microfluidic device. Without this condition, it was not possible to effectively flush out photoactive solutions from the microfluidic device following HMW polymerization. The valve was secured to the optical table using a custom-built, 3D-printed fixture, and a long PEEK tubing was used to transport solutions from the outlet of the valve to a single fluidic port on the microfluidic device. All other fluidic ports on the microfluidic device were connected to 1.5 mL Eppendorf tubes via PEEK tubing of identical cross sectional dimensions to that described previously. Two through holes were punched at the top of each Eppendorf tube using a 1.5 mm biopsy punch (Integra Milltex). The first through hole was made to enable the PEEK tubing to easily enter the Eppendork tubes, and the second was to relieve any pressure buildup that would occur as the Eppendorf tubes filled with liquid.

4.2.2 Microfluidic device for HMW fabrication tests

The design for the microfluidic device used in HMW fabrication tests can be found in **Figure 4-5** (this was the design used to manufacture the device pictured in **Figure 3-8**). Cross sectional channel dimensions and HMW slot dimensions reflect those described in **Table 3.1**. The rationale behind this device design was that each HMW could be tested for leaks simply by changing the direction of flow. This is because, for each HMW, there is a flow direction (left or right) for which there are no upstream HMWs. Leaks in upstream HMWs were previously found to make it more difficult to determine if downstream HMWs were leak-free.

4.3 Experimental Design

4.3.1 Hydrogel composition

As discussed in sec. 4.1.2, the three essential components of a chain polymerized PEG solution are functionalized PEG molecules, photoinitiator, and water. From these components, there are four relevant parameters that can be altered depend-

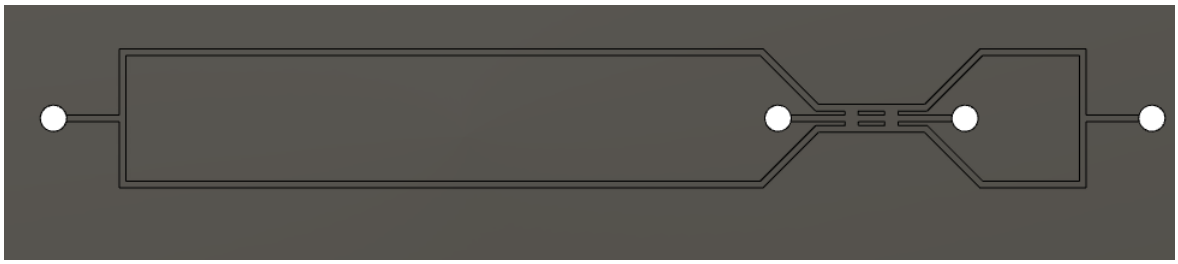

Figure 4-5: Design for HMW fabrication test device.

ing on the application's desired gel properties. These parameters are the molecular weight of the PEG molecules, water content, the type of photoinitiator used, and the concentration of photoinitiator.

Both the molecular weight of the PEG molecules used and the water content of the gel have been shown to heavily influence the diffusive properties of the hydrogel as well as it's swelling properties [136]. Larger molecular weight (MW) PEG hydrogels with high water content are associated with a higher diffusivity and a higher swelling ratio, while low MW PEG hydrogels with low water content are associated with a lower diffusivity and swelling ratio. This fundamentally comes down to the density of crosslinking points and its impact on mesh size; the higher the density of crosslinking points, the smaller the mesh size. A smaller mesh size means that it is harder for molecules to diffuse through the gel, and there is less entropic slack available to enable the gel to expand. For this application, the created hydrogel should be highly diffuse in order to deliver CPAs to the oocyte as fast as possible. Thus, the HMW should consist of a hydrogel with a high MW PEG species and a high water content. Using past work on HMWs as a reference [82], it was decided that HMWs were to be fabricated using high (~20 kDa) MW PEGDA and high (~80%) water content.

The photoinitiator used in these experiments was chosen to be lithium phenyl-2,4,6-trimethylbenzoylphosphinate (LAP). LAP was chosen because of its high water solubility and it's photoactivity at the projected wavelength of 405 nm [137].[2]

Photoinitator concentration is expected to have an impact on spatial resolution, with higher concentrations resulting in decreased spatial resolution. This is because higher concentrations of photoinitiator tend to result in a greater density of free radicals. These free radicals can diffuse away from the site of UV exposure [138] and trigger unwanted chain polymerization events, resulting in thicker HMWs. Also, as a higher photoinitiator concentration results in a more photo-sensitive solution, any diffraction of the UV pattern will have more pronounced effects on the final gel thickness. A higher photoinitiator concentration also increases the depth of gel that can be generated for a given UV exposure [139]. This result is a consequence of the "working curve" equation for photopolymerizable polymers, which states that the

[2]As the optical setup was inherited, it was decided that it would be easier to choose an optically compatible photoinitiator as opposed to changing the UV LED inside the light engine with one that projects a shorter wavelength of UV. However, if one wanted to use a different photoinitiator for some reason, one could as long as the system optics were altered appropriately.

polymerization depth, P_d, can be expressed as

$$P_d = D_p \ln\left(\frac{E_{\max}}{E_c}\right) \tag{4.1}$$

where $E_{\max}$ is the maximum UV exposure energy, E_c is the critical UV exposure energy needed to trigger polymerization, and D_p is the penetration depth, which describes how efficiently light is transmitted through the polymer medium. E_c is inversely proportional to photoinitiator concentration, meaning that to increase P_d, one should increase the photoinititor concentration.

Thus, it would seem that there is a conflict in determining photoinitiator concentration. In order to deliver CPAs to the oocyte quickly, the fabricated HMW should have a minimal thickness. This suggests that a small amount of photoinitiator should be used. However, in order to be an effective convection barrier, the HMW needs to be polymerized throughout the channel depth, which would suggest that a high concentration of photoinitiator should be used. This conflict can be resolved by trying to use the growing HMW as a self-propagating waveguide [140, 141]. Though this has not been explicitly achieved with a PEG hydrogel, high water content PEG hydrogels have been used previously as waveguides, suggesting that self-propagating PEG hydrogel waveguides may be possible [142].

Self-propagating waveguides attempt to exploit the difference in RI between the polymerized and non-polymerized phases in order to create high aspect ratio, photopolymerized structures. The key to utilizing this property is to find an optimal exposure condition that is above the minimum threshold needed to trigger polymerization, but uses a sufficiently low intensity so as to avoid creating an excess of free radicals too quickly. This excess of free radicals would diffuse away from the site of exposure and defeat the purpose of self focusing. This upper intensity bound, $I_{\max}$, is defined in the below equation as

$$I_{\max} \approx \frac{E_c}{\tau} \tag{4.2}$$

where τ is the average lifetime of a free radical [140]. While the average lifetime of a free radical may vary slightly with changes in photoinitiator concentration, the relationship between E_c and photoinitiator concentration is much stronger. Thus, to increase the band of acceptable UV intensities that can generate a self-propagating waveguide, photoinitiator concentration should be decreased. This circumvents the need for a high photoinitator concentration as was suggested by eq. 4.1, as the UV intensity exiting the waveguide tip should be relatively constant. Thus, contrary to the HMW literature where relatively large (~5% w/w) concentrations of photoinitiator are used [99], for the below experiments, a relatively low photoinitiator concentration of 0.25% w/w was used.

4.3.2 Choice of objective

The primary parameter characterizing an objective for this application is its magnification. Magnification is mainly related to minimum projected feature size and

projected UV intensity. The higher the magnification, the smaller the minimum feature size, and the higher the projected UV intensity.

Thus, the choice of the correct objective seems to be a matter of balancing conflicting system requirements. An objective needs to have a high enough magnification to generate sufficiently thin HMWs, and a low enough magnification so as not to expose the HMW with an intensity exceeding $I_{\max}$. Balancing these two requirements led to the use of a 5x objective. Using this objective, UV patterns were able to be projected with incredibly high resolution (**Figure 4-6**).

4.3.3 UV Exposure and pattern

The UV exposure condition was selected with eq. 4.2 in mind. Thus, by trial and error, the intensity of UV exposure was gradually increased until polymerization was observed to occur in the polymer solution. Using the 5x objective, this intensity was found to be $188\frac{\text{mW}}{\text{cm}^2}$.

The projected UV pattern was initially a thin straight line. However, after it was found that polymerization tended to be poor at the HMW ends, a "dumbbell" pattern (**Figure 4-6**) was adopted in order to compensate for this.

4.4 Experimental procedure

4.4.1 Solution preparation

The name, composition, and function of the different solutions injected into the HMW fabrication test device are shown in **Table 4.1**.

Table 4.1: Name, composition and function of the solutions injected into the HMW fabrication test device.

Name	**Composition**	**Function**
Saturation Solution	2.5% w/w solution of photoinitiator in red food dye	Block the device walls with photoinitiator prior to hydrogel polymerization. Food dye used for contrast
PEGDA solution	20% w/w PEGDA MW 750 0.25% w/w photoinitiator 79.75% DI water	Precursor for the HMW
Wash solution	DI water with green food dye	Flush device of all photo-active components. Food dye used for contrast during wash.

Note that, contrary to the discussion in sec 4.3.1, a relatively low MW PEGDA was used in these experiments. This was simply because of the cost of high MW PEGDA. Thus, to save money, low MW PEGDA was used in these preliminary experiments,

with the expectation that higher MW PEGDA would be used once the polymerization conditions became better defined, and the HMW diffusivity became more relevant.

4.4.2 Microscope stage adjustment

As HMW fabrication is an optically induced process, controlling the projection plane of the UV pattern was crucial to successful fabrication. From **Figure 4-3** and **Figure 4-4**, it can be deduced that control over the locations of the projection plane of the UV pattern and the focal plane of the microscope were coupled. The focal plane of the microscope was determined by the height of the objective, and the projection plane of the UV pattern was determined by the height of the objective and the distance between the light engine and the collimating tube. If these two planes were adjusted such that they coincided, then the result was that the reflection of the UV pattern came into focus on the CMOS camera (**Figure 4-6**).

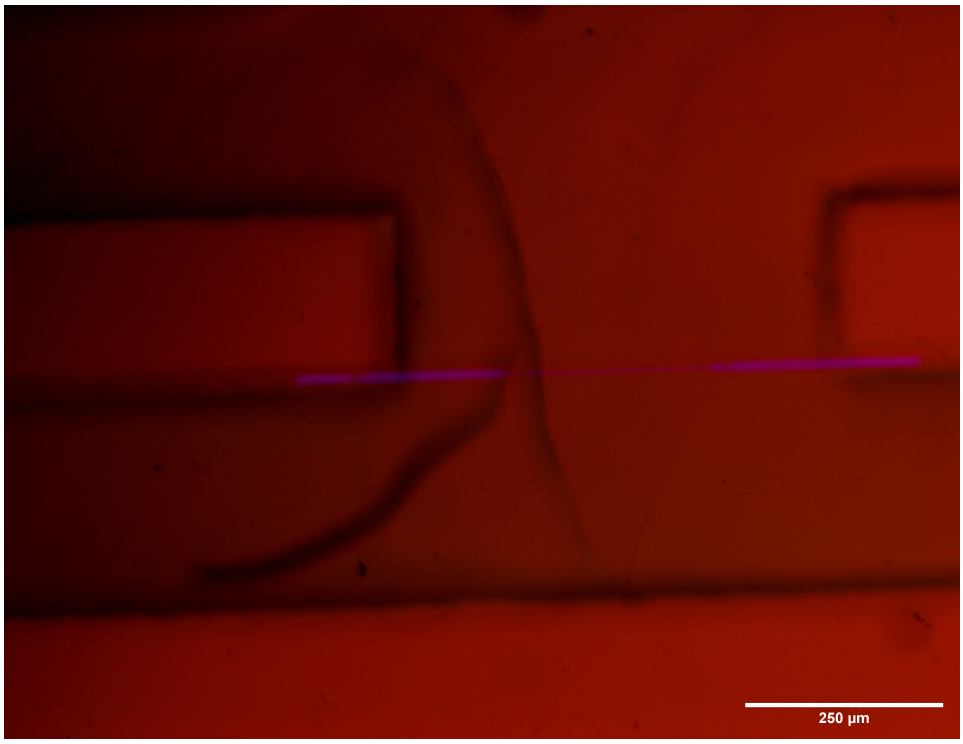

Figure 4-6: UV pattern reflection near an HMW slot visible to the CMOS camera. This indicates that the focal plane of the microscope and the projection plane of the UV pattern are coincident.

Using this feature of the optical system, the projection plane of the UV pattern was controlled as follows. First, the thickness of the COC window (see sec. 3.3.3) residing below the microfluidic device channels was measured using digital calipers (Neiko). Then, the bottom of the COC window was marked with a black marker (Sharpie) near the region of HMW fabrication. The microfluidic device was then loaded onto the microscope, and the height was adjusted until the marker spot came

into sharp focus. This was considered to be the bottom of the microfluidic device. The objective was then moved upwards by an amount equal to the thickness of the COC window. This was accomplished with accuracy by using the 1 μm gradations on the microscope's fine adjustment knob. At this point, the focal plane of the microscope coincided with the bottom surface of the microfluidic channels. The UV pattern was then projected to the microscope, and the distance between the light engine and collimating tube was adjusted using a translational XY positioning stage (Thorlabs, Newton, NJ). This distance was adjusted until the reflected UV pattern came into sharp focus, indicating the projection plane of the UV pattern coincided with the bottom of the microfluidic device channels. The positions of the objective and the light engine remained unaltered until the completion of HMW fabrication. The location of the UV pattern was then recorded in the camera's computer-based user interface, and UV projection was turned off.

4.4.3 Fabrication work flow

The experimental work flow for HMW fabrication testing is shown in **Figure 4-7**. The process began by appropriately plumbing the device. This included loading one syringe with wash solution, one with saturation solution, and one with PEGDA solution. Note that, in the past, the Griffith lab has observed phase separation in photoactive solutions over time. Thus, as a preventive measure, all photoactive solutions were vortexed directly before their loading into syringes. Appropriate tubing was then attached to each syringe, and each tube was filled with the contents of the syringe it was attached to before the tubing was loaded into the inlets of the fluidic valve. Any syringes containing photoactive components were wrapped in aluminum foil to protect them from background UV light. One of the tubes connected to the COC device was then loaded into the outlet of the fluidic valve. At this point, the transmission illumination source was turned on, and ambient lights were turned off and blocked with black curtains. The device was then flushed with saturation solution in order to purge the device channels and tubing of air, and to coat the device walls with photoinitiator; in the past, the Griffith lab has experienced issues where photoiniator has adsorbed to container surfaces, reducing the concentration of photoinitiator in the bulk solution, and negatively impacting polymerization. Thus, as a preventive measure, this step was added to the protocol. Once the device was filled with saturation solution, flow was stopped and the saturation solution was left static in the microfluidic device for 15 minutes. After this time had elapsed, the device was then flooded with PEGDA solution until all saturation solution had been removed from the device. Once this had occurred, the region of the camera where the UV pattern had been recorded was aligned with the HMW slot of interest, and the selected UV pattern was projected for 50 seconds. After this time had elapsed, an HMW occupied the entire width of the HMW slot. Then, when the desired number of HMWs had been fabricated, wash solution was flown through the device in order to remove all photoactive species. Ambient light was then turned back on, and the device was appropriately re-plumbed in order to check the HMWs for leaks.

In the above work flow, all solutions were introduced to the device at a rate of 50

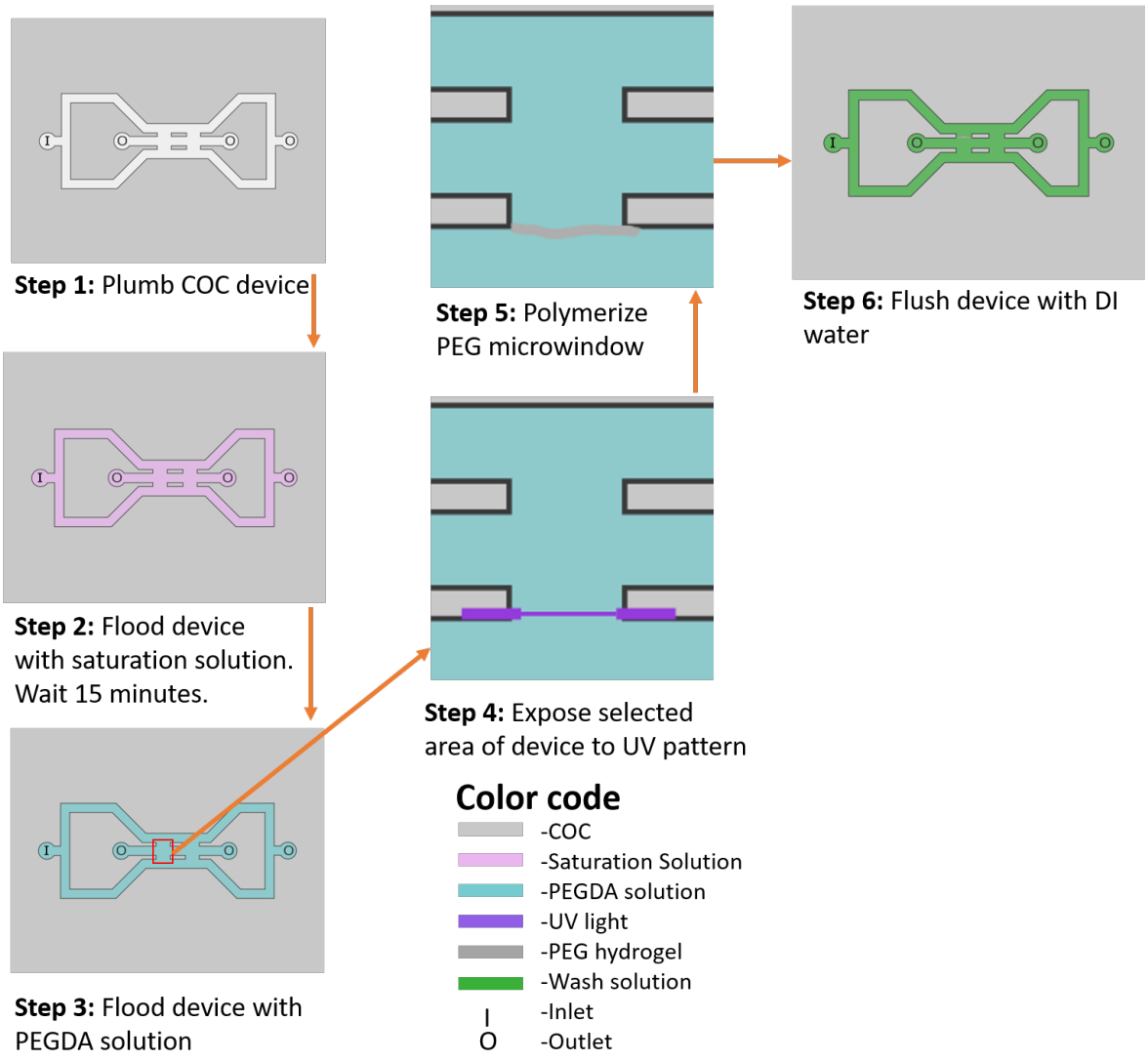

Figure 4-7: Experimental work flow for HMW fabrication test experiments. Orange arrows indicate the sequence of steps.

$\frac{\mu L}{min}$ without the occurrence of fluidic leaks.

4.5 Experimental results

After HMWs were manufactured using the protocol described above, they were tested to see if they were indeed leak-free and were acting as diffusion allowing convection barriers. To test this, the work flow described in **Figure 4-8** was performed. First, the device was replumbed such that there were now two fluidic connections acting as inlets; a green inlet, where water mixed with green food dye entered, and a clear inlet, where clear water entered. Note that, at the start of this test, the device was full of green-dyed water from the final step of the HMW fabrication process. As before, solutions were loaded into syringes, syringes were loaded into syringe pumps, and tubes were attached to each syringe. Outlet tubes were connected to 1.5 mL Eppendorf tubes using the same protocol described previously. Flow was then initiated at both inlets in a parallel configuration, and was modulated such that clear water did not flow back towards the green inlet. Once this was achieved, the HMW was monitored to see if it could effectively act as a convection barrier, indicated by division between clear water and green dyed water. As shown in **Figure 4-9**, the HMW did indeed act an effective convection barrier between the two solutions. Thus, the fabrication of a ~100 μm wide, 250 μm high HMW inside a sealed COC device has been achieved, providing a proof of concept for the microfluidic device conceived in sec. 2.2. This HMW has been shown to be able to remain intact and in place under flows at least as high as 50 $\frac{\mu L}{min}$, providing a rough validation of its mechanical integrity and stability.

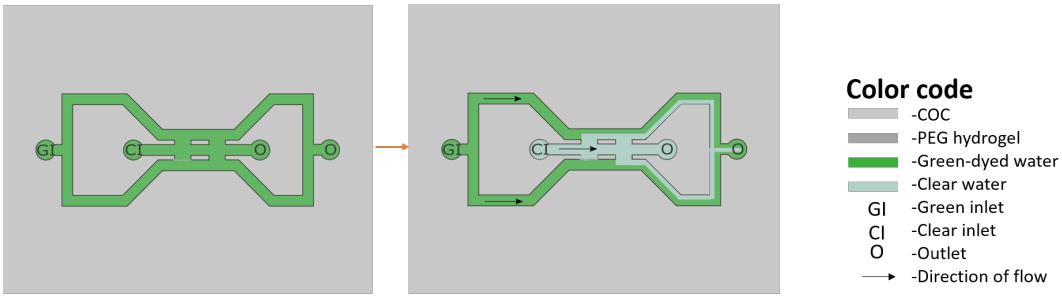

Figure 4-8: Experimental work flow for testing HMWs for leaks.

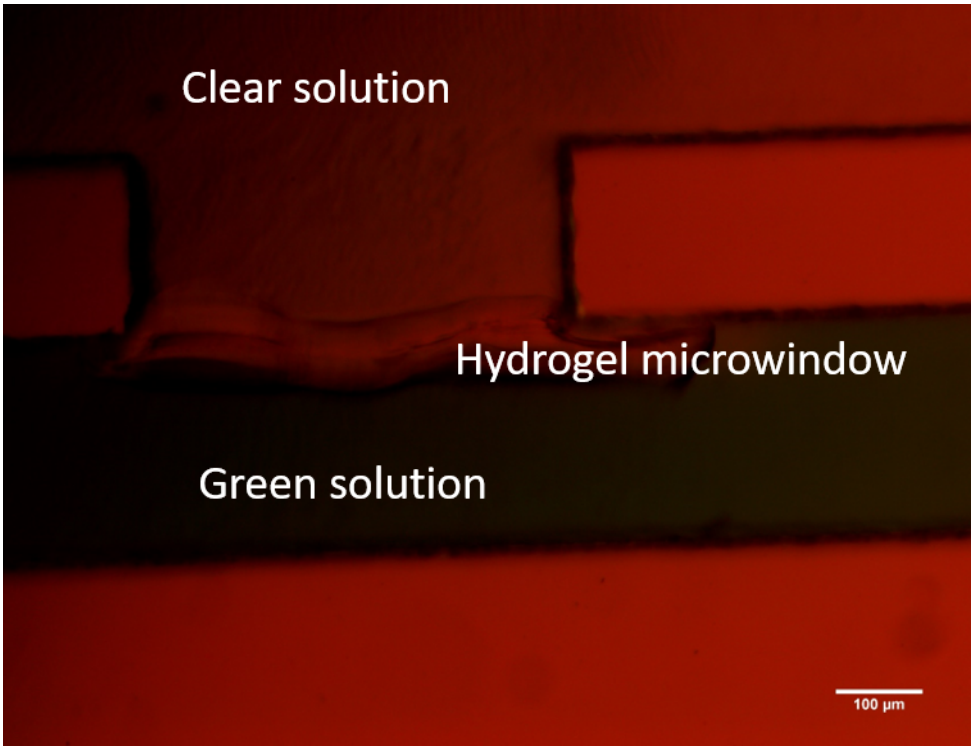

Figure 4-9: PEG hydrogel microwindow successfully acting as a convection barrier between clear water and green-dyed water.

Chapter 5

Conclusion and future work

5.1 Conclusion

While oocyte cryopreservation has come a long way over the past 35 years, the heterogeneity in clinical outcomes resulting from the widespread use of manual vitrification indicates that there is still more work to be done. By analyzing the technical challenges of manual vitrification and the fundamental risks underlying the vitrification process, an automated CPA loading and unloading platform was proposed that merged microfluidics, automation, and optical measurement systems. This platform hoped to overcome the challenges faced by manual vitrification, and merge the benefits exhibited by existing CPA loading and unloading platforms.

In order to begin creating the proposed platform, a microfluidic device was designed that was simple to fabricate and operate while also giving the user control over the oocyte's chemical environment throughout the CPA loading and unloading process. This design included the use of HMWs which required that the microfluidic building material be oxygen impermeable. This restriction disqualified the commonly used PDMS as a candidate prototyping material, and necessitated experimentation with less commonly used materials. Initially, NOA-81 was seen as a viable alternative. However, difficulties in high AR feature replication, device sealing, and optical clarity proved to be overly cumbersome, and the material was abandoned in favor of COC. Using micromilling, a novel device sealing technique, and a custom world-to-connector, the designed microfluidic device was able to be realized and operated at flow rates of up to 50 $\frac{\mu L}{min}$without leaks.

Following microfluidic device fabrication, a PμSL setup was adapted to perform HMW fabrication. HMWs were to be fabricated using high MW, high water content PEG in order to increase the HMW's diffusivity. Moreover, to increase spatial resolution and attempt to have the growing HMW act as a self-propagating waveguide, a low concentration of photoinitiator was used. The objective and UV intensity were also determined by trial and error to provide sufficiently high spatial resolution without overpolymerizing the HMW solution. The UV pattern was selected to overcome the phenomenom of HMWs being poorly polymerized at their ends. These parameters, along with the past experience of the Griffith lab, led to the development of an

experimental protocol for the fabrication of HMWs. This protocol ultimately led to the creation of an HMW that was ~100 μm in width and was able to successfully act as a convection barrier. This HMW was also found to remain in place under flows at least as high as 50 $\frac{\mu L}{min}$. This proof-of-concept validates the creation of leak-free HMWs in COC devices and, by extension, the proposed microfluidic device. This promising work marks the first step towards a completely automated vitrification platform, capable of removing the uncertainty in success plaguing clinics and their patients.

5.2 Future work for CPA loading and unloading

5.2.1 HMW fabrication

The choice to try to use the growing HMW as a self-propagating waveguide was made because of it's relatively large height of 250 μm. For reference, the tallest HMW created in the literature is only 80 μm tall [99]. The challenge in creating tall HMWs is the limited depth of field (DOF) achievable using an optical microscopy setup such as the one described in **Figure 4-4**. The DOF is a quasi-arbitrary measure of the axial distance along the optical axis for which a feature can be resolved. For HMW fabrication, this roughly translates to how deep into a microfluidic channel a UV pattern can be projected before it begins to be significantly blurred. The DOF is related to the numerical aperture (NA) of a microscope's objective and, for low NA, the DOF can be approximated as

$$\text{DOF} \approx \frac{\lambda n}{\text{NA}^2} \tag{5.1}$$

where λ is the wavelength of light used, and n is the refractive index of the medium between the specimen and the objective [143]. Rearranging the above equation to isolate NA gives

$$\text{NA} \approx \sqrt{\frac{\lambda n}{\text{DOF}}} \tag{5.2}$$

To project through the depth of a 250 μm channel, the minimum DOF must be 250 μm. Taking $\lambda = 405\,\text{nm}$ (the wavelength of projected UV light), $n = 1$ (refractive index of air), it is found that the maximum allowable NA is

$$\text{NA} \approx \sqrt{\frac{(405 * 10^{-3})(1)}{250}} = \mathbf{0.04} \tag{5.3}$$

This value is well below the NA of typically available microscope objectives (the NA of a basic 2x Nikon microscope objective is 0.1), which motivated experimentation using self-propagating waveguides.

While it was shown in the previous section that leak-free HMWs can be polymerized in COC devices, it is unclear whether this is because the self-propagating waveguide property is being appropriately utilized. It is possible, instead, that after

a sufficiently long exposure, enough free radicals are generated to diffuse upwards and trigger polymerization outside the projected DOF. It is also possible that polymerization is still happening outside the projected DOF, and the arbitrary blurring limit for which an image is out of focus is relatively negligible for this distinctly different application.

To better assess how and why the HMW is polymerized, future work will be focused on experimentally quantifying parameters of the hydrogel prepolymer that, until this point, have been tuned with a qualitative sense of what is occurring. This, for instance, would help determine whether the condition of eq. 4.2 is actually being satisfied. These values would also help in the performance of MATLAB simulations, with which experimental results could be compared against.

Another issue that has plagued this project is repeatability in HMW fabrication. Using the same exposure conditions and experimental protocol, different thickness and height HMWs have been fabricated. While many of these repeatability issues had previously been attributed to issues with the setup for HMW fabrication experiments and the microfluidic device, as these issues have now been successfully resolved, more scrutiny needs to be placed on the process of HMW fabrication. One possible fix for these repeatability issues would be to opt for a better established method of manufacturing tall structures by UV polymerization than self-propagating waveguides, such as layer-by-layer polymerization. This technique is at the core of stereolithography (SLA) 3D printing, and has shown to reliably produce high aspect ratio structures with height on the order of millimeters (for more information on SLA 3D printing, watch the following video). By making accurate, repeatable adjustments to the objective height and distance from the light engine to the collimating tube, manual layer-by-layer polymerization can be achieved. Later on, this process can be automated if need be.

5.2.2 Oocyte position control

Syringe pumps responsive to real-time computer commands (two PHD 2000 Programmable pumps and one PHD Ultra pump from Harvard Apparatus, Holliston, MA) have been acquired and preliminary tests have been performed to evaluate their performance characteristics. These tests have shown that the three pumps can be successfully controlled by a single computer, and are capable of infusing and withdrawing liquid at precise flow rates. These tests have also shown that the older, PHD Programmable pumps have a system response time of ~250 ms, meaning that commands to the pumps must be spaced out by at least this time in order to ensure proper command execution. These significant system delays make traditional controllers designed in the continuous time domain, such as PI controllers, difficult to implement, as each cycle through the feedback loop will generate a new flow rate which will introduce more delay into the system. Thus, in order to mitigate these system delays, a feedback controller should be designed that heavily restricts the number of executable flow rates.

Bang-bang controllers are perhaps the simplest conceivable feedback controllers. These controllers are designed to produce a finite number of possible control outputs

to a range of different control inputs. As the feedback controller for this application should be designed to restrict the number of executable flow rates, utilization of a bang-bang controller seems appropriate. Using a bang-bang controller, there will be two executable flow rates; one will be for coarse adjustment of the oocyte position, and the other for fine adjustment. As each syringe pump can either infuse or withdraw liquid, this limits each syringe to only four potential "flow states", reducing the number of commands needed to operate the system. Using the described control system, an oocyte positioning work flow can be proposed (**Figure 5-1**). Future work will be focused on execution of this proposed work flow, which will include design of a proper device visualization platform, creation of an "oocyte recognition" code using MATLAB's image processing toolbox, and integration of this code into a larger, bang-bang control system with the described flow control outputs.

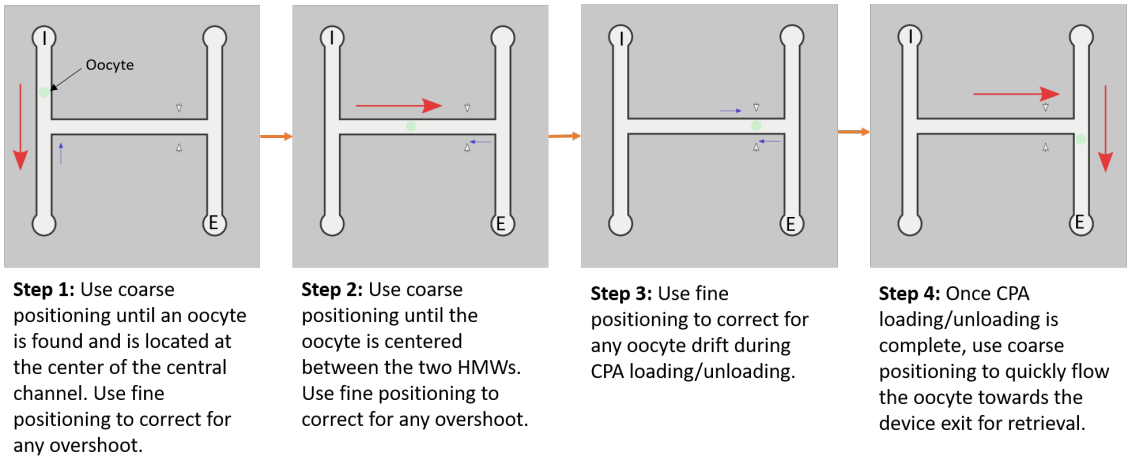

Figure 5-1: Proposed work flow for automated oocyte positioning inside the designed microfluidic device. Note that large, red arrows represent coarse oocyte position adjustments, small, blue arrows represent fine oocyte position adjustments, and white arrow heads denote the location of HMW midpoints. The fluidic ports labeled with the letters "I" and "E" are the sites of oocyte introduction and exit respectively.

5.2.3 BSI measurement system

Little experimental work has been performed towards the development of a BSI measurement system. However, as this will be a crucial tool in evaluating diffusivity of CPAs across HMWs, it is imperative that testing on this front begin soon, given the described success in creating leak-free HMWs. Using materials available in the Manalis lab, preliminary work evaluating the feasibility of a BSI measurement system for rectangular-channeled COC devices will be performed.

5.3 Future work towards a comprehensive, automated oocyte vitrification system

5.3.1 Oocyte vitrification platform and maximal cooling and warming rates

The choice of oocyte vitrification platform strongly impacts the cooling and warming rates that a vitrification system is able to achieve and reproduce. To better understand how the oocyte vitrification platform impacts the magnitude and reproducibility of cooling and warming rates, a brief heat transfer analysis can be performed. This begins by computing the Biot number, Bi, for a typical oocyte-containing vitrification platform. Estimates for external convection coefficient, h, of boiling liquid nitrogen during oocyte vitrification range from 125 $\frac{\mathrm{W}}{\mathrm{m^2-K}}$ – 1000 $\frac{\mathrm{W}}{\mathrm{m^2-K}}$ [144], and a typical VS has a thermal conductivity, k, of ~0.8 $\frac{\mathrm{W}}{\mathrm{m-K}}$ [145]. Taking a conservative characteristic length, L, of 500 μm, the Bi can be computed as

$$Bi = \frac{h}{k}L = \frac{500}{0.8}(500 \times 10^{-6}) = \mathbf{0.3125} \tag{5.4}$$

Thus, it can be concluded that while lumped parameter analysis (LPA) may not be able to be used for quantitative predictions regarding this thermal system, using it to make qualitative design choices has merit. Performing an energy balance on the oocyte containing vitrification platform using LPA gives

$$hA(T_\infty - T_s)A_s = \rho c_p \frac{dT}{dt}V \tag{5.5}$$

where T_∞ is the bulk liquid nitrogen temperature, T_s is the surface temperature of the vitrification platform, A_s is the surface area of the vitrification platform exposed to liquid nitrogen, ρ and c_p are the average density and specific heat, respectively, of the vitrification platform and VS, $\frac{dT}{dt}$ is the cooling/warming rate, and V is the combined volume of the vitrification platform and VS. Rearranging the above equation, the cooling/warming rate is found to be

$$\frac{dT}{dt} = \frac{hA(T_\infty - T_s)A_s}{\rho c_p V} \tag{5.6}$$

One conclusion from this result is that it is the surface-to-volume ratio, and not necessarily only the volume, that determines the cooling/warming rate. Thus, in order to achieve high cooling and warming rates that are reproducible, it is imperative that a vitrification platform with a consistent and large surface-volume-ratio is used. To this end, the author recommends the use of an ultra-thin straw.

The primary rationale behind this suggestion is the reproducibility of the surface-to-volume ratio despite minor fluctuations in the dispensed volume; minor changes in volume will only impact the height of the fluid column inside the straw. As the

surface-to volume ratio, SV_c, of a long, slender cylinder is

$$SV_c = \frac{A_{s,c}}{V_c} = \frac{2\pi rh}{\pi r^2 h} = \frac{2}{r} \tag{5.7}$$

it can be observed that SV_c is independent of the height of the fluid column. Moreover, the use of ultra-thin straws has already been shown to produce extraordinarily high cooling and warming rates. For instance, researchers have already successfully used quartz microcapillaries (QMCs) to achieve low-CPA vitrification by ultra fast cooling [146]. By leveraging the thin walls, small diameter, and favorable thermal properties of quartz, cooling rates of $\sim 10^5 \frac{^\circ C}{min}$–$10^6 \frac{^\circ C}{min}$ were projected. Thus by using a QMC, or potentially an even more thermally conductive material such as stainless steel (ultra-thin walled syringe tips are already commercially available), a large and repeatable cooling/warming rate can be achieved.

5.3.2 Cooling and warming protocol

Automation of the cooling and warming steps will be accomplished through the use of a robotic manipulator, and will likely proceed as follows. After CPA loading, the oocyte will quickly be flown out of the microfluidic device inside of a sub-microliter droplet of solution. The oocyte will then be retrieved and cooled following the protocol described in **Figure 5-2**. The oocyte-containing capillary will then be manually transferred to a larger tank of liquid nitrogen for long term oocyte storage.

When the oocyte is to be warmed, an oocyte-containing capillary will be manually retrieved from long term cryostorage and placed in a transportable liquid nitrogen container. This container will then be placed below a robotic gripper. Oocyte warming will be performed as described in **Figure 5-3**. After the oocyte has been warmed, the warmed oocyte will be withdrawn from a Petri dish using a syringe pump in preparation for CPA unloading. CPA unloading will then performed. After the oocyte is ejected from the microfluidic device, it will be transferred to a capillary similar to the process described in steps 1-3 of **Figure 5-2**, and will be ejected from the capillary into a Petri dish of warm culture medium similar to the process described in steps 2-3 of **Figure 5-3**. The oocyte will then be manually transferred to an incubator in preparation for fertilization.

The proposed cooling work flow is very similar to the one utilized by SARAH, but differs in it's addition of a downward spiral motion of the capillary during submersion in liquid nitrogen. This is performed in order to decrease vapor buildup around the capillary walls and enhance heat transfer. As for warming, it is unclear to the author if the SARAH platform performs this step manually because of it's need for manual loading of straws into the robotic manipulator, or because the motions involved in removing a straw from liquid nitrogen and submerging it in a pool of warming solution are too complex to be performed in under ~1 s. If the latter is the case, then the work flow described in **Figure 5-3** would need to be re-evaluated. One potential alternative would be to simplify the motion through the use of a "warm water gun" that jets water at 37 °C out of its nozzle. Such a device could be positioned ~10 cm above the liquid nitrogen tank, and used to spray the capillary with warm water immediately upon

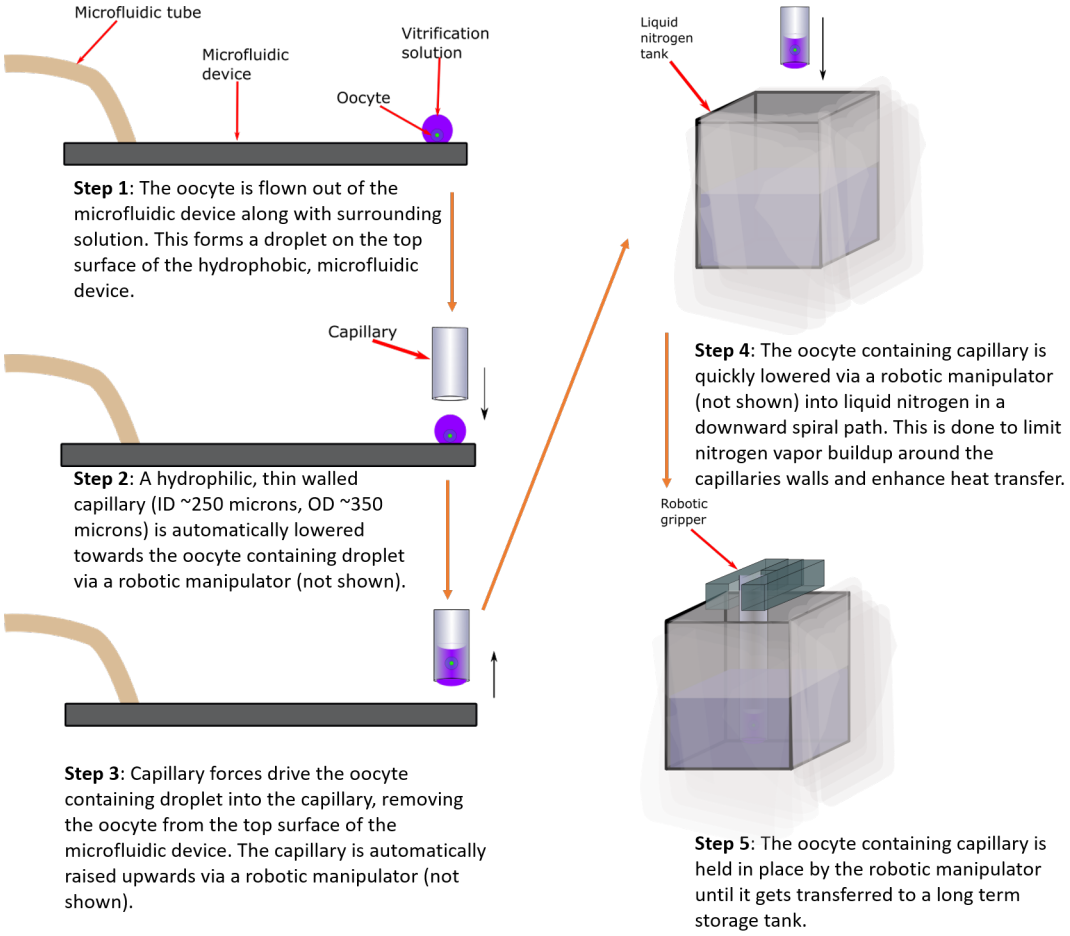

Figure 5-2: Process flow for oocyte cooling. Note that black arrows indicate paths of motion, and orange arrows indicate the sequence of steps.

its exit from the liquid nitrogen tank. Alternatively, the robotic manipulator could be outfitted with a heating element that could warm the capillary while it is being transported to warming solution. Through theoretical and experimental analysis, a power input profile could be determined that is capable of rapidly warming the capillary to 37 °C prior to its introduction into warming solution.

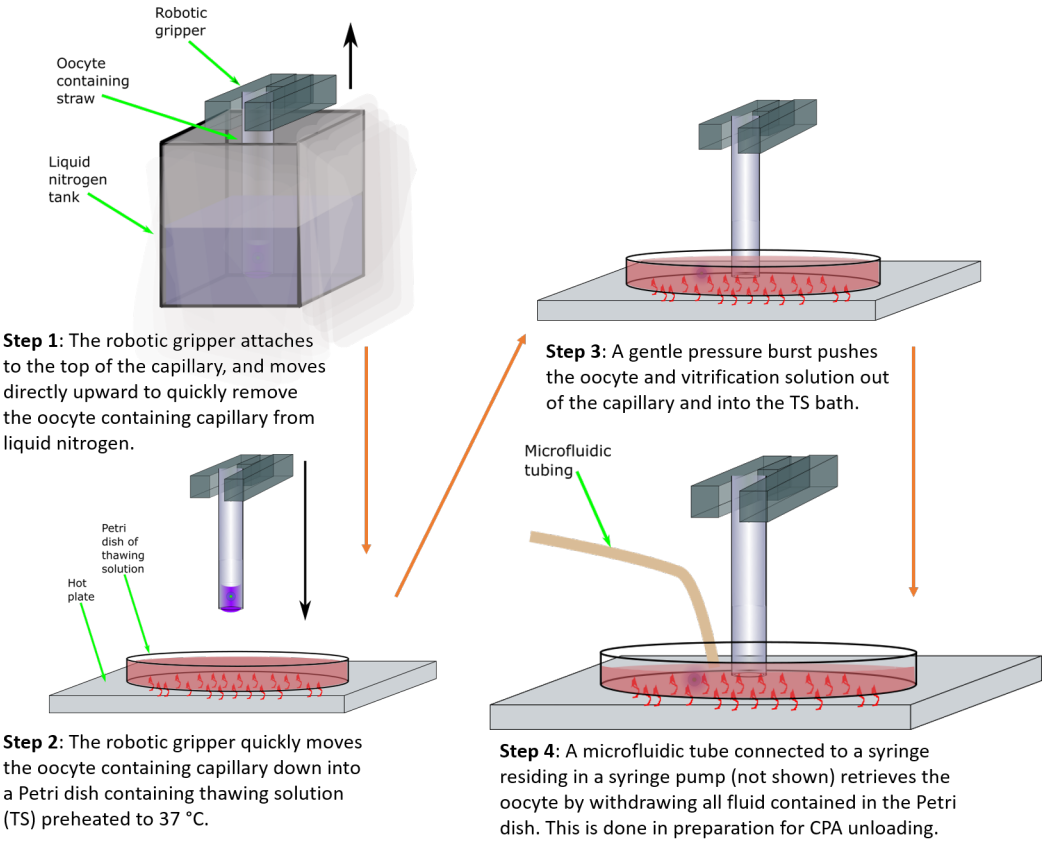

Figure 5-3: Process flow for oocyte warming. Note that black arrows indicate paths of motion, curly red arrows indicate heat, and orange arrows indicate the sequence of steps.

Appendix A

Supplementary Notes

A.1 Calculation of change in RI during CPA loading and unloading

The calculation for the change in RI during CPA loading was performed using the Irvine Scientific vitrification solution, which contains 15% v/v DMSO and 15% v/v EG, and the calculation for the change in RI during CPA unloading was performed using the Irvine Scientific thawing solution, which contains 1 M sucrose [21]. All components other than CPAs were approximated to have the properties of pure water, and the culture medium in which oocytes begin and end the vitrification/thaw process was approximated to have the properties of pure water. DMSO is reported to have an RI of $n_{\text{DMSO}} = 1.4772$ [147], EG is reported to have an RI of $n_{\text{EG}} = 1.4318$ [148], sucrose is reported to have an RI of $n_{\text{suc}} = 1.5376$ [149], and pure water is reported to have an RI of $n_{\text{water}} = 1.3325$ [150]. By applying the Arago-Biot approach [151], an estimate for the RI of the vitrification solution can be obtained by computing a weighted average of individual RIs based on each component's volumetric fraction. Doing this gives a refractive index for the vitrification solution, n_{VS}, of

$$\begin{aligned} n_{\text{VS}} &= (1 - 0.15 - 0.15)(1.3325) + (0.15)(1.4318) + (0.15)(1.4772) \\ &= \mathbf{1.3691} \end{aligned} \tag{A.1}$$

which ultimately gives a change in RI over the course of CPA loading, ΔRI_{load}, of

$$\Delta RI_{\text{load}} = n_{\text{VS}} - n_{\text{water}} = 1.3691 - 1.3325 = \mathbf{3.66 \times 10^{-2}} \tag{A.2}$$

For CPA unloading, the sucrose concentration of the thawing solution must be converted to a volumetric fraction in order to apply the Arago-Biot approach. Knowing that sucrose has a molar mass and density of $342.3\frac{\text{g}}{\text{mol}}$ and $1.58\frac{\text{g}}{\text{mL}}$ respectively [149], the volumetric fraction of sucrose, ϕ_{suc}, can be calculated to be

$$\phi_{\text{suc}} = \frac{1}{1}\frac{\text{mol}}{\text{L}} \times \frac{342.3}{1}\frac{\text{g}}{\text{mol}} \times \frac{1}{1.58}\frac{\text{mL}}{\text{g}} \times \frac{1}{1000}\frac{L}{mL} \times 100\% = \mathbf{21.6\%} \tag{A.3}$$

Using the Arago-Biot approach, the RI of the thawing solution, n_{TS}, can be found to be

$$\begin{aligned} n_{\mathrm{TS}} &= (1 - 0.216)(1.3325) + (0.216)(1.5376) \\ &= \mathbf{1.3768} \end{aligned} \tag{A.4}$$

which gives a change in RI over the course of CPA unloading, ΔRI_{unload}, of

$$\Delta RI_{unload} = n_{\mathrm{water}} - n_{\mathrm{TS}} = 1.3325 - 1.3768 = \mathbf{-4.43 \times 10^{-2}} \tag{A.5}$$

A.2 Detailed explanations for determination of design specifications

A table of relevant design specifications of the CPA loading and unloading device design, with explanations, can be found below.

Table A.1: Relevant design specifications of the CPA loading and unloading device design.

Specification	**Value**	**Rationale**
Channel width	250 microns	A sample of 314 human oocytes taken from 72 infertile couples were found to have a mean total diameter (including perivitelline space and zona pellucida) of $\mu = 164\,\mu$m, with a standard deviation of $\sigma = 17\,\mu$m [73]. Therefore, to be able to accommodate oocytes of all sizes, the minimum channel height needs to be $> \mu + 3\sigma = 164 + (3)(17) = \mathbf{215}\,\boldsymbol{\mu}\mathbf{m}$. A value of $250\,\mu m$ seemed large enough to accommodate the largest human oocytes without excessively increasing the diffusion distance of CPAs to the oocyte.
Channel height	250 microns	same as above
Length of mixing channel	50 mm	Determined by computing the characteristic diffusion length given a reasonable Peclet number flow.
Length of HMW slot	500 microns	This is more than double the total diameter of a large human oocyte. This allows for comfortable tolerancing when positioning the oocyte during CPA loading and unloading.
Width of HMW slot	125 microns	To increase the rate at which CPAs are delivered to the oocyte, HMWs should be as thin as possible without compromising their structural integrity. One may then think that this dictates that the width of the HMW slot should also be minimized. However, as is detailed in chapter 3, fabrication of high aspect ratio microfluidic structures is challenging. Moreover, the width of the HMW slot is simply an upper bound for the HMW width, and HMWs smaller than the width of this slot can be fabricated. 125 microns describes a width that can be comfortably manufactured and is on the order of the expected HMW width.

A.3 Protocol for fabrication of SU-8 master mold

All processing parameters for SU-8 2010 were taken from [152] and all processing parameters for SU-8 2150 were taken from [110].

1. Enter class 10,000 cleanroom.

2. Clean a 4-inch diameter silicon wafer with acetone and isopropanol. Dry with compressed nitrogen gas.

3. Place wafer on a hot plate at 150 °C for 5 minutes to ensure complete dehydration at the wafer surface.

4. Align wafer center with the center of spin coater.

5. Turn on vacuum to secure wafer in place.

6. Pour SU-8 2010 (Microchem) onto the center of the wafer, and set the speed of the spin coater to 500 rpm. Wait ~5 seconds.

7. Gently increase the spin coater speed to 2500 rpm, and then wait 30 seconds. This corresponds to a film thickness of 12 microns.

8. Turn off the spin coater, and place the wafer onto a hot plate at 95 °C for 3 minutes to soft bake the SU-8 in order to thicken the photoresist by removing its solvents.

9. Transfer the wafer to a mask aligner device (MA6, Karl Suss), and expose the wafer to 9 $\frac{\text{mW}}{\text{cm}^2}$ on the UV400 setting (350 nm-450 nm) for 15 seconds. Note that this SU-8 layer has no pattern, and is fabricated solely as a base layer meant to improve adhesion between the wafer and the thicker SU-8 layer to be fabricated.

10. Remove the wafer from the mask aligner and place it on to a hot plate at 95 °C for 4 minutes to hard bake the wafer to strengthen the bonds in the newly polymerized photoresist.

11. Repeat steps 4 and 5.

12. Pour SU-8 2150 onto the center of the wafer, and set the speed of the spin coater to 500 rpm. Wait ~5 seconds.

13. Gently increase the spin coater speed to 2150 rpm, and then wait 30 seconds. This corresponds to a film thickness of 250 microns.

14. Turn off the spin coater, and soft bake the wafer by putting it on a hot plate at 65 °C for 7 minutes, followed by leaving it at 95 °C for 60 minutes. This, again, is done to evaporate solvents from the photoresist to thicken it.

15. When finished soft baking, transfer the wafer to the mask aligner, and insert the desired Mylar mask (Mylar masks were designed in AutoCAD, and were manufactured by FineLine Imaging, Colorado Spring, CO). A sample Mylar mask design can be found in **Figure A-1**. Set the mask aligner to "hard contact mode".

16. Expose the wafer to 9 $\frac{\text{mW}}{\text{cm}^2}$ on the UV400 setting (350 nm-450 nm) for 42 seconds.

17. Hard bake the wafer by putting on a hot plate at 65 °C for 5 minutes, followed by leaving it at 95 °C for 20 minutes. This, again, is done to strengthen the bonds in the newly polymerized photoresist.

18. Align the wafer center with the center of the spin coater, and secure the wafer by turning on the vacuum. Set the wafer speed to 1000 rpm.

19. Generously spray SU-8 developer solution into the center of the wafer while it spins. Continue until the developer solution flung off from the spin coater is clear as opposed to milky white.

20. Clean the wafer with isopropanol, and dry with compressed nitrogen gas.

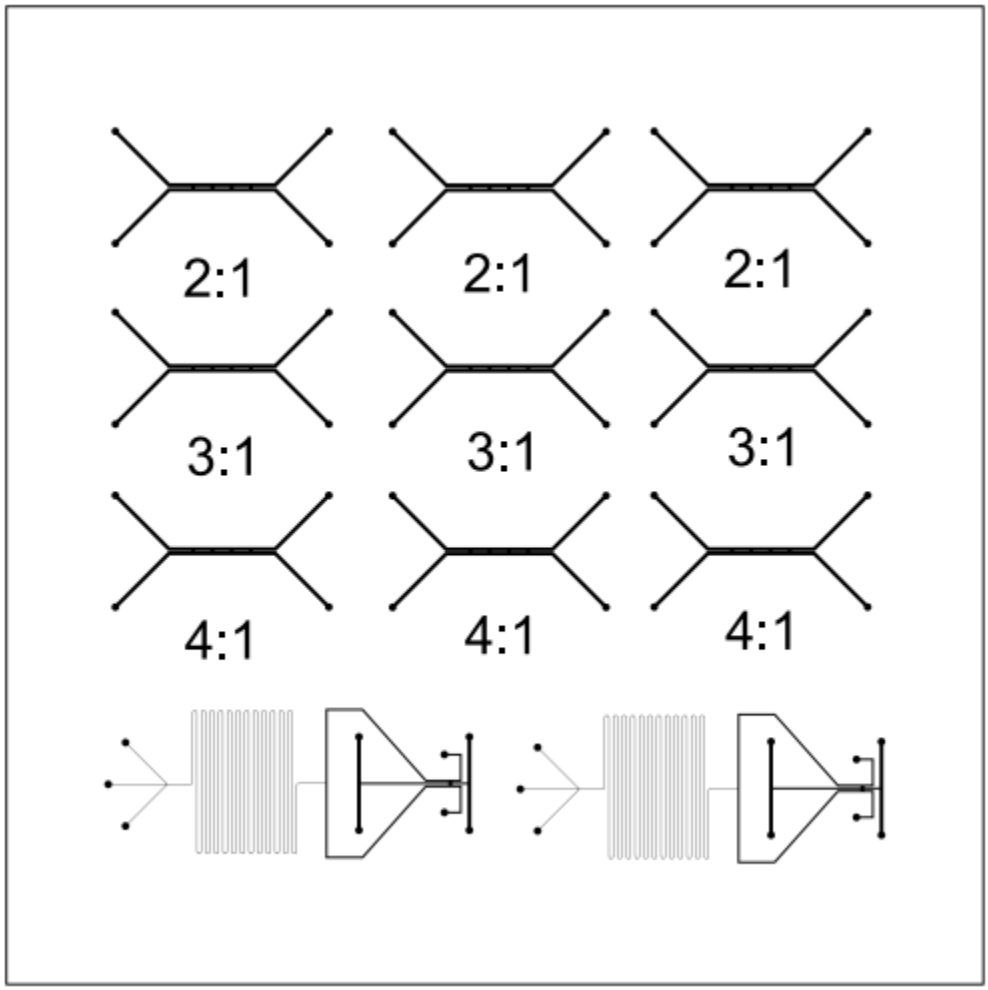

Figure A-1: Sample photomask used for SU-8 master mold development. The top three rows of designs were used to fabricate HMW fabrication test devices with differing aspect ratios for the HMW slots. The bottom row of designs was used to fabricate sample CPA loading and unloading devices similar to the one described in **Figure 3-1**. Areas shaded in black indicate where the SU-8 2150 was not polymerized, and areas shaded in white indicate where the SU-8 2150 was polymerized. The total photomask size was 5" x 5".

A.4 Design of sample acrylic tube holder for microfluidic world to chip connection

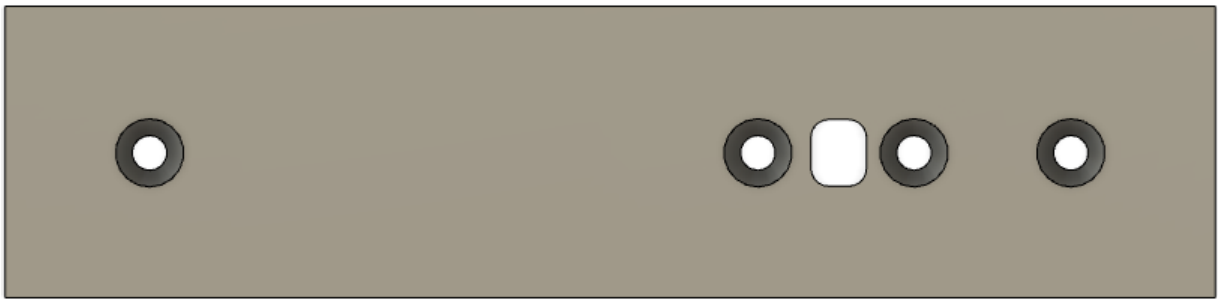

Figure A-2: Design of a sample acrylic tube holder for microfluidic world to chip connection. This tube holder was used for an HMW test fabrication device. The four chamfered holes are used to provide locations for leak-free tubing connections, and the slot in the middle is designed as a window for CPA concentration measurements.

A.5 Digital Micromirror Device Geometry of PRO4500

Schematics of the PRO4500's DMD can be found below.

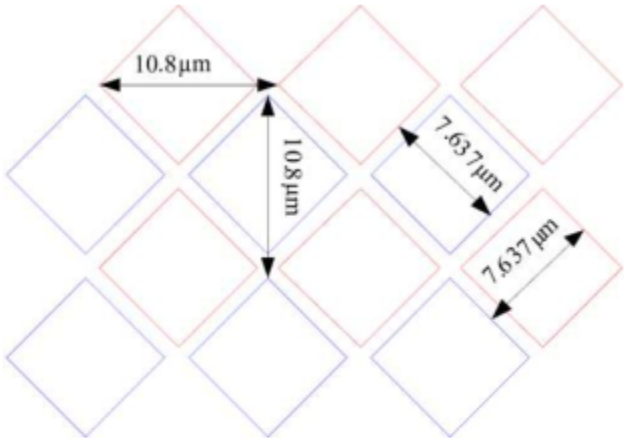

Figure 1-3. 0.45-Inch DMD Diamond Pixel Geometry

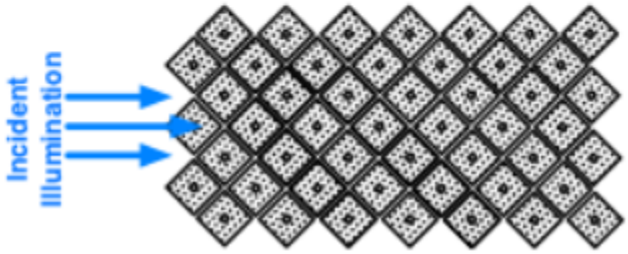

Figure A-3: Geometrical specifications of the PRO4500's DMD.

Bibliography

[1] "What is Assisted Reproductive Technology? | Reproductive Health | CDC." [Online]. Available: https://www.cdc.gov/art/whatis.html

[2] P. C. Steptoe and R. G. Edwards, "Birth after the reimplantation of a human embryo," *The Lancet*, vol. 312, no. 8085, p. 366, 1978.

[3] A. Trounson and L. Mohr, "Human pregnancy following cryopreservation, thawing and transfer of an eight-cell embryo," *Nature*, vol. 305, no. 5936, pp. 707–709, 1983.

[4] W. Ombelet and J. Van Robays, "Artificial insemination history: hurdles and milestones." *Facts, views & vision in ObGyn*, vol. 7, no. 2, pp. 137–43, 2015. [Online]. Available: http://www.ncbi.nlm.nih.gov/pubmed/26175891

[5] S. Blakeslee, "INFERTILE WOMAN HAS BABY THROUGH EMBRYO TRANSFER - The New York Times," New York, NY, p. 6, feb 1984. [Online]. Available: https://www.nytimes.com/1984/02/04/us/infertile-woman-has-baby-through-embryo-transfer.html

[6] C. Chen, "Pregnancy after human oocyte cryopreservation," *The Lancet*, vol. 327, no. 8486, pp. 884–886, 1986.

[7] W. F. Rall and G. M. Fahy, "Ice-free cryopreservation of mouse embryos at -196 C by vitrification," *Nature*, vol. 313, no. 6003, pp. 573–575, 1985.

[8] L. Kuleshova, L. Gianaroli, C. Magli, A. Ferraretti, and A. Trounson, "Birth following vitrification of a small number of human oocytes," *Human Reproduction*, vol. 14, no. 12, pp. 3077–3079, 1999.

[9] W. Würfel, M. Schleyer, G. Krüsmann, I. V. Hertwig, and K. Fiedler, "Fertilization of cryopreserved and thawed human oocytes (cryo-Oo) by injection of spermatozoa (ICSI)–medical management of sterility and case report of a twin pregnancy," *Zentralblatt fur Gynakologie*, vol. 121, no. 9, pp. 444–448, 1999.

[10] M. Kuwayama, G. Vajta, O. Kato, and S. P. Leibo, "Highly efficient vitrification method for cryopreservation of human oocytes," *Reproductive BioMedicine Online*, vol. 11, no. 3, pp. 300–308, 2005. [Online]. Available: https://www.rbmojournal.com/article/S1472-6483(10)60837-1/pdf

[11] G. D. Smith, P. C. Serafini, J. Fioravanti, I. Yadid, M. Coslovsky, P. Hassun, J. R. Alegretti, and E. L. Motta, "Prospective randomized comparison of human oocyte cryopreservation with slow-rate freezing or vitrification," *Fertility and Sterility*, vol. 94, no. 6, pp. 2088–2095, 2010.

[12] J. Saragusty and A. Arav, "Current progress in oocyte and embryo cryopreservation by slow freezing and vitrification," *Reproduction*, vol. 141, no. 1, pp. 1–19, jan 2011. [Online]. Available: http://www.ncbi.nlm.nih.gov/pubmed/20974741

[13] Practice Committees of the American Society for Reproductive Medicine and the Society for Assisted Reproductive Technology, "Mature oocyte cryopreservation: a guideline," *Fertility and Sterility*, vol. 99, pp. 37–43, 2013. [Online]. Available: http://dx.doi.org/10.1016/j.fertnstert.2012.09.028

[14] A. M. Quaas, A. Melamed, K. Chung, K. A. Bendikson, and R. J. Paulson, "Egg banking in the United States: Current status of commercially available cryopreserved oocytes," *Fertility and Sterility*, vol. 99, no. 3, pp. 827–831, 2013.

[15] A. M. Quaas and G. Pennings, "The current status of oocyte banks: domestic and international perspectives," *Fertility and Sterility*, vol. 110, no. 7, pp. 1203–1208, 2018. [Online]. Available: https://doi.org/10.1016/j.fertnstert.2018.07.013

[16] J. A. Robertson Baker, "Ethical and legal issues in cryopreservation of human embryos," *Fertility and Sterility*, vol. 47, no. 3, pp. 371–381, 1987.

[17] D. Mihai, E. Brătilă, C. Mehedințu, C. Berceanu, and S. M. Pițuru, "The ethical aspects regarding cryopreserved embryos," *Romanian Journal of Legal Medicine*, vol. 25, no. 3, pp. 317–321, 2017.

[18] J. Carpenter, "The Economics of Freezing Your Eggs," New York, NY, feb 2020. [Online]. Available: https://www.wsj.com/articles/the-economics-of-freezing-your-eggs-11581786000

[19] C. Weller, "What you need to know about egg-freezing, the hot new perk at Google, Apple, and Facebook," *Business Insider*, sep 2017. [Online]. Available: https://www.businessinsider.com/egg-freezing-at-facebook-apple-google-hot-new-perk-2017-9

[20] The Society for Assisted Reproductive Technology, "National Summary Report," Tech. Rep. [Online]. Available: https://www.sartcorsonline.com/rptCSR_PublicMultYear.aspx?ClinicPKID=0

[21] "Simplified Embryo Vitrification Protocols | Irvine Scientific." [Online]. Available: http://www.irvinesci.com/simplified-embryo-vitrification-protocols

[22] "Protocols - Cryotech." [Online]. Available: https://www.cryotechlab.com/protocols/

[23] "SAGE Vitrification Kit | CooperSurgical Fertility Companies." [Online]. Available: https://fertility.coopersurgical.com/products/sage-vitrification-kit/

[24] "CRYOTOP® Open System | Kitazato, pioneers in vitrification." [Online]. Available: https://www.kitazato-dibimed.com/cryotop-vitrification/cryotop-open-system/

[25] M. A. Khalili, A. Shahedi, S. Ashourzadeh, S. A. Nottola, G. Macchiarelli, and M. G. Palmerini, "Vitrification of human immature oocytes before and after in vitro maturation: a review," *Journal of Assisted Reproduction and Genetics*, vol. 34, no. 11, pp. 1413–1426, nov 2017.

[26] M. Grynberg, A. Mayeur Le Bras, L. Hesters, V. Gallot, and N. Frydman, "First birth achieved after fertility preservation using vitrification of in vitro matured oocytes in a woman with breast cancer," *Annals of Oncology*, vol. 31, no. 4, pp. 541–542, feb 2020.

[27] S. J. Paynter and B. J. Fuller, "Cryopreservation of Mammalian Oocytes," in *Cryopreservation and Freeze-Drying Protocols*, 2nd ed., J. Day and G. N. Stacey, Eds. Totowa, NJ: Humana Press Inc., 2007, ch. 22, pp. 313–324.

[28] S. Abe, Y. Koyanagi, M. Nakano, M. Sasaki, A. Matsuzawa, K. Yoshida, Y. Tokunaga, K. Momozawa, and T. Miyake, "Usefulness of vitrification device having vitrification solution absorber for cryopreservation of mouse embryos at the blastocyst stage," *Japanese Journal of Veterinary Research*, vol. 68, no. 1, pp. 63–68, 2020.

[29] L. Parmegiani, G. E. Cognigni, S. Bernardi, S. Cuomo, W. Ciampaglia, F. E. Infante, C. Tabarelli De Fatis, A. Arnone, A. M. MacCarini, and M. Filicori, "Efficiency of aseptic open vitrification and hermetical cryostorage of human oocytes," *Reproductive BioMedicine Online*, vol. 23, no. 4, pp. 505–512, 2011. [Online]. Available: http://dx.doi.org/10.1016/j.rbmo.2011.07.003

[30] M. Solé, J. Santaló, M. Boada, E. Clua, I. Rodríguez, F. Martínez, B. Coroleu, P. N. Barri, and A. Veiga, "How does vitrification affect oocyte viability in oocyte donation cycles? A prospective study to compare outcomes achieved with fresh versus vitrified sibling oocytes," *Human Reproduction*, vol. 28, no. 8, pp. 2087–2092, 2013.

[31] S. Tannus, M.-H. Dahan, J. Tan, and S.-L. Tan, "Issues related to human oocyte vitrification: a consideration of the facts," *Journal of Assisted Reproduction and Genetics*, vol. 35, no. 7, pp. 1157–1158, 2018.

[32] R. H. Goldman, C. Racowsky, L. V. Farland, S. Munné, L. Ribustello, and J. H. Fox, "Predicting the likelihood of live birth for elective oocyte cryopreservation: a counseling tool for physicians and patients," *Human Reproduction*, vol. 32, no. 4, pp. 853–859, 2017. [Online]. Available: https://academic.oup.com/humrep/article-abstract/32/4/853/2968357

[33] "ReproTech - Embryo, Sperm, Oocyte Storage | Oocyte Storage Costs." [Online]. Available: https://www.reprotech.com/oocyte-storage-costs.html

[34] E. C. Kaye, "One in four—the importance of comprehensive fertility benefits for the medical workforce," *New England Journal of Medicine*, vol. 382, no. 16, pp. 1491–1493, 2020.

[35] D. E. Pegg, "Principles of cryopreservation." in *Cryopreservation and Freeze-Drying Protocols*, 2nd ed., J. G. Day and G. N. Stacey, Eds. Totowa, NJ: Humana Press Inc., 2007, ch. 3, pp. 39–57.

[36] G. M. Fahy and B. Wowk, "Principles of Cryopreservation by Vitrification," in *Cryopreservation and Freeze-Drying Protocols*, 3rd ed., H. Oldenhof and W. F. Wolkers, Eds. Humana Press, 2015, ch. 2, pp. 21–82.

[37] M. Sakurai, T. Furuki, K. I. Akao, D. Tanaka, Y. Nakahara, T. Kikawada, M. Watanabe, and T. Okuda, "Vitrification is essential for anhydrobiosis in an African chironomid, *Polypedilum vanderplanki*," *Proceedings of the National Academy of Sciences of the United States of America*, vol. 105, no. 13, pp. 5093–5098, apr 2008.

[38] J. F. Povey, N. Perez-Moral, T. R. Noel, R. Parker, M. J. Howard, and C. M. Smales, "Investigating variables and mechanisms that influence protein integrity in low water content amorphous carbohydrate matrices," *Biotechnology Progress*, vol. 25, no. 5, pp. 1217–1227, sep 2009. [Online]. Available: http://www.ncbi.nlm.nih.gov/pubmed/19691119

[39] N. J. Yang and M. J. Hinner, "Getting across the cell membrane: an overview for small molecules, peptides, and proteins," in *Site-Specifi c Protein Labeling: Methods and Protocols*, 1st ed., M. J. Hinner and A. Gautier, Eds. New York, NY: Humana Press Inc., 2015, ch. 3, pp. 29–53.

[40] "DMSO Physical Properties | Gaylord Chemical." [Online]. Available: https://www.gaylordchemical.com/literature/dmso-physical-properties/

[41] "Mono Ethylene Glycol - antifreeze." [Online]. Available: http://www.veximchem.com/productsM/monoethyleneglycol-antifreeze.html

[42] B. P. Best, "Cryoprotectant Toxicity: Facts, Issues, and Questions," *Rejuvenation Research*, vol. 18, no. 5, pp. 422–436, oct 2015.

[43] G. Zhao and J. Fu, "Microfluidics for cryopreservation," *Biotechnology Advances*, vol. 35, no. 2, pp. 323–336, 2017.

[44] G. M. Fahy, "Overview of biological vitrification," in *Vitrification in Assisted Reproduction*, 2nd ed., M. J. Tucker and J. Liebermann, Eds. Boca Raton, FL: Taylor and Francis Group, LLC, 2016, ch. 1, pp. 1–22.

[45] P. Vanderzwalmen, D. Connan, L. Grobet, B. Wirleitner, B. Remy, S. Vanderzwalmen, N. Zech, and F. J. Ectors, "Lower intracellular concentration of cryoprotectants after vitrification than after slow freezing despite exposure to higher concentration of cryoprotectant solutions," *Human Reproduction*, vol. 28, no. 8, pp. 2101–2110, 2013. [Online]. Available: https://academic.oup.com/humrep/article-abstract/28/8/2101/659258

[46] J. Mandelbaum, O. Anastasiou, R. Lévy, J. F. Guérin, V. De Larouzière, and J. M. Antoine, "Effects of cryopreservation on the meiotic spindle of human oocytes," *European Journal of Obstetrics and Gynecology and Reproductive Biology*, vol. 113, no. SUPPL., pp. 17–23, 2004.

[47] M. Martínez-Burgos, L. Herrero, D. Megías, R. Salvanes, M. C. Montoya, A. C. Cobo, and J. A. Garcia-Velasco, "Vitrification versus slow freezing of oocytes: Effects on morphologic appearance, meiotic spindle configuration, and DNA damage," *Fertility and Sterility*, vol. 95, no. 1, pp. 374–377, 2011.

[48] E. Van den Abbeel, U. Schneider, J. Liu, Y. Agca, J. K. Critser, and A. Van Steirteghem, "Osmotic responses and tolerance limits to changes in external osmolalities, and oolemma permeability characteristics, of human in vitro matured MII oocytes," *Human Reproduction*, vol. 22, no. 7, pp. 1959–1972, 2007.

[49] S. F. Mullen, Y. Agca, D. C. Broermann, C. L. Jenkins, C. A. Johnson, and J. K. Critser, "The effect of osmotic stress on the metaphase II spindle of human oocytes, and the relevance to cryopreservation," *Human Reproduction*, vol. 19, no. 5, pp. 1148–1154, 2004. [Online]. Available: https://www.ncbi.nlm.nih.gov/pubmed/15070883

[50] J. O. M. Karlsson, E. A. Szurek, A. Z. Higgins, S. R. Lee, and A. Eroglu, "Optimization of cryoprotectant loading into murine and human oocytes," *Cryobiology*, vol. 68, no. 1, pp. 18–28, 2014. [Online]. Available: http://dx.doi.org/10.1016/j.cryobiol.2013.11.002

[51] H. Newton, D. E. Pegg, R. Barrass, and R. G. Gosden, "Osmotically inactive volume, hydraulic conductivity, and permeability to dimethyl sulphoxide of human mature oocytes," *Journal of Reproduction and Fertility*, vol. 117, no. 1, pp. 27–33, 1999.

[52] S. J. Paynter, L. O'Neil, B. J. Fuller, and R. W. Shaw, "Membrane permeability of human oocytes in the presence of the cryoprotectant propane-1,2-diol," *Fertility and Sterility*, vol. 75, no. 3, pp. 532–538, mar 2001.

[53] S. J. Paynter, A. Borini, V. Bianchi, L. De Santis, C. Flamigni, and G. Coticchio, "Volume changes of mature human oocytes on exposure to cryoprotectant solutions used in slow cooling procedures," *Human Reproduction*, vol. 20, no. 5, pp. 1194–1199, 2005. [Online]. Available: https://academic.oup.com/humrep/article-abstract/20/5/1194/2356638

[54] D. Lai, J. Ding, G. W. Smith, G. D. Smith, and S. Takayama, "Slow and steady cell shrinkage reduces osmotic stress in bovine and murine oocyte and zygote vitrification," *Human Reproduction*, vol. 30, no. 1, pp. 37–45, 2015.

[55] L. Rienzi, S. Romano, L. Albricci, R. Maggiulli, A. Capalbo, E. Baroni, S. Colamaria, F. Sapienza, and F. Ubaldi, "Embryo development of fresh 'versus' vitrified metaphase II oocytes after ICSI: a prospective randomized sibling-oocyte study," *Human Reproduction*, vol. 25, no. 1, pp. 66–73, 2010. [Online]. Available: https://www.ncbi.nlm.nih.gov/pmc/articles/PMC2794665/

[56] S. Crawford, S. L. Boulet, J. F. Kawwass, D. J. Jamieson, and D. M. Kissin, "Cryopreserved oocyte versus fresh oocyte assisted reproductive technology cycles, United States, 2013," *Fertility and Sterility*, vol. 107, no. 1, pp. 110–118, 2017. [Online]. Available: http://dx.doi.org/10.1016/j.fertnstert.2016.10.002

[57] Y. S. Heo, H. J. Lee, B. A. Hassell, D. Irimia, T. L. Toth, H. Elmoazzen, and M. Toner, "Controlled loading of cryoprotectants (CPAs) to oocyte with linear and complex CPA profiles on a microfluidic platform," *Lab on a Chip*, vol. 11, no. 20, pp. 3530–3537, 2011.

[58] M. G. Larman and P. Vanderzwalmen, "Open versus closed systems," in *Vitrification in Assisted Reproduction*, 2nd ed., M. J. Tucker and J. Liebermann, Eds. Boca Raton, FL: CRC Press, 2016, ch. 6, pp. 55–59.

[59] T. Takahashi, A. Hirsh, E. Erbe, and R. J. Williams, "Mechanism of Cryoprotection by Extracellular Polymeric Solutes," *Biophysical Journal*, vol. 54, no. 3, pp. 509–518, 1988. [Online]. Available: http://dx.doi.org/10.1016/S0006-3495(88)82983-7

[60] S. Seki and P. Mazur, "Ultra-Rapid Warming Yields High Survival of Mouse Oocytes Cooled to -196 C in Dilutions of a Standard Vitrification Solution," *PLoS ONE*, vol. 7, no. 4, p. e36058, 2012.

[61] Y. Rabin, P. S. Steif, K. C. Hess, J. L. Jimenez-Rios, and M. C. Palastro, "Fracture formation in vitrified thin films of cryoprotectants," *Cryobiology*, vol. 53, no. 1, pp. 75–95, aug 2006.

[62] P. S. Steif, M. C. Palastro, and Y. Rabin, "Continuum mechanics analysis of fracture progression in the vitrified cryoprotective agent DP6," *Journal of Biomechanical Engineering*, vol. 130, pp. 1–7, apr 2008.

[63] A. Arav, S. Yavin, Y. Zeron, D. Natan, I. Dekel, and H. Gacitua, "New trends in gamete's cryopreservation," *Molecular and Cellular Endocrinology*, vol. 187, pp. 77–81, 2002.

[64] I. I. Katkov and F. Levine, "Prediction of the glass transition temperature of water solutions: Comparison of different models," *Cryobiology*, vol. 49, no. 1, pp. 62–82, aug 2004.

[65] T. K. Roy, S. Brandi, C. K. Bradley, and T. T. Peura, "Automatic vitrification: Development of the Gavi system," in *Vitrification in Assisted Reproduction*, 2nd ed., M. J. Tucker and J. Liebermann, Eds. Boca Raton, FL: CRC Press, 2016, ch. 7, pp. 61–68.

[66] "Gavi- Automated Vitrification." [Online]. Available: https://www.geneabiomedx.com/Products/Gavi

[67] "Assessment of the New Automated Vitrification System "GAVI" for Early Cleaved Embryos Cryopreservation." [Online]. Available: https://clinicaltrials.gov/ct2/show/NCT03478592

[68] T. K. Roy, S. Brandi, N. M. Tappe, C. K. Bradley, E. Vom, C. Henderson, C. Lewis, K. Battista, B. Hobbs, S. Hobbs, J. Syer, S. R. Lanyon, S. M. Dopheide, T. T. Peura, S. J. Mcarthur, M. C. Bowman, and T. Stojanov, "Embryo vitrification using a novel semi-automated closed system yields in vitro outcomes equivalent to the manual Cryotop method," *Human Reproduction*, vol. 29, no. 11, pp. 2431–2438, 2014. [Online]. Available: https://academic.oup.com/humrep/article-abstract/29/11/2431/2427120

[69] M. Sole, N. Polyzos, C. G. Llagostera, B. Carrasco, B. Coroleu, A. Veiga, and M. Boada, "Automatic vs manual vitrification of human oocytes. preliminary results of the first randomised controlled trial using sibling oocytes," *Fertility and Sterility*, vol. 108, no. 3, p. e57, 2017. [Online]. Available: http://dx.doi.org/10.1016/j.fertnstert.2017.07.180

[70] K. Edashige and M. Kasai, "The movement of water and cryoprotectants in mammalian oocytes and embryos: Membrane permeability and aquaporins," in *Vitrification in Assisted Reproduction*, 2nd ed., M. J. Tucker and J. Lieberman, Eds. Boca Raton, FL: CRC Press, 2016, ch. 4, pp. 47–54.

[71] A. Dhali, A. P. Kolte, A. Mishra, S. C. Roy, and R. Bhatta, "Cryopreservation of Oocytes and Embryos: Current Status and Opportunities," in *Infertility, Assisted Reproductive Technologies and Hormone Assays*. IntechOpen, jan 2019, pp. 1–16.

[72] A. Arav, Y. Natan, D. Kalo, A. Komsky-Elbaz, Z. Roth, P. E. Levi-Setti, M. Leong, and P. Patrizio, "A new, simple, automatic vitrification device: preliminary results with murine and bovine oocytes and embryos," *Journal of Assisted Reproduction and Genetics*, vol. 35, no. 7, pp. 1161–1168, 2018.

[73] C. Valeri, S. Pappalardo, M. De Felici, and C. Manna, "Correlation of oocyte morphometry parameters with woman's age," *Journal of Assisted Reproduction and Genetics*, vol. 28, no. 6, pp. 545–552, 2011.

[74] J. Liu, C. Shi, J. Wen, D. Pyne, H. Liu, C. Ru, J. Luo, S. Xie, and Y. Sun, "Automated Vitrification of Embryos," *IEEE Robotics & Automation Magazine*, pp. 33–40, jun 2015.

[75] A. C. Varghese and C. S. Siristatidis, "Automation in Vitrification," in *In Vitro Fertilization: A Textbook of Current and Emerging Methods and Devices*, 2nd ed., Z. P. Nagy, A. C. Varghese, and A. Agarwal, Eds. Cham, Switzerland: Springer Nature Switzerland AG, 2019, ch. 71.2.4, pp. 852–853.

[76] Y. Zou, T. Yin, S. Chen, J. Yang, and W. Huang, "On-Chip Cryopreservation: A Novel Method for Ultra-Rapid Cryoprotectant-Free Cryopreservation of Small Amounts of Human Spermatozoa," *PLoS ONE*, vol. 8, no. 4, p. e61593, apr 2013. [Online]. Available: https://dx.plos.org/10.1371/journal.pone.0061593

[77] H. Huang, J. K. Choi, W. Rao, S. Zhao, P. Agarwal, G. Zhao, and X. He, "Alginate Hydrogel Microencapsulation Inhibits Devitrification and Enables Large-Volume Low-CPA Cell Vitrification," *Advanced Functional Materials*, vol. 25, no. 44, pp. 6839–6850, 2015.

[78] D. G. Pyne, J. Liu, M. Abdelgawad, and Y. Sun, "Digital microfluidic processing of mammalian embryos for vitrification," *PLoS ONE*, vol. 9, no. 9, p. e108128, 2014.

[79] W. H. Tan and S. Takeuchi, "A trap-and-release integrated microfluidic system for dynamic microarray applications," *Proceedings of the National Academy of Sciences of the United States of America*, vol. 104, no. 4, pp. 1146–1151, jan 2007.

[80] Y. S. Song, S. Moon, L. Hulli, S. K. Hasan, E. Kayaalp, and U. Demirci, "Microfluidics for cryopreservation," *Lab on a Chip*, vol. 9, pp. 1874–1881, 2009.

[81] T. Scherr, S. Pursley, W. T. Monroe, and K. Nandakumar, "A numerical study on distributions during cryoprotectant loading caused by laminar flow in a microchannel," *Biomicrofluidics*, vol. 7, p. 021410, 2013.

[82] J. S. Paustian, R. N. Azevedo, S. T. B. Lundin, M. J. Gilkey, and T. M. Squires, "Microfluidic microdialysis: Spatiotemporal control over solution microenvironments using integrated hydrogel membrane microwindows," *Physical Review X*, vol. 3, no. 4, pp. 1–13, 2014.

[83] R. J. Kimmerling, G. Lee Szeto, J. W. Li, A. S. Genshaft, S. W. Kazer, K. R. Payer, J. De Riba Borrajo, P. C. Blainey, D. J. Irvine, A. K. Shalek, and S. R. Manalis, "A microfluidic platform enabling single-cell RNA-seq of multigenerational lineages," *Nature Communications*, vol. 7, pp. 1–7, 2016. [Online]. Available: http://dx.doi.org/10.1038/ncomms10220

[84] N. L. Calistri, R. J. Kimmerling, S. W. Malinowski, M. Touat, M. M. Stevens, S. Olcum, K. L. Ligon, and S. R. Manalis, "Microfluidic active loading of single cells enables analysis of complex clinical specimens," *Nature Communications*, vol. 9, pp. 1–7, 2018. [Online]. Available: http://dx.doi.org/10.1038/s41467-018-07283-x

[85] G. Ternstrom, A. Sjorstrand, G. Aly, and A. Jernqvist, "Mutual Diffusion Coefficients of Water+Ethylene Glycol and Water+ Glycerol Mixtures," *Journal of Chemical and Engineering Data*, vol. 41, no. 4, pp. 876–879, 1996.

[86] A. Vishnyakov, A. P. Lyubartsev, and A. Laaksonen, "Molecular Dynamics Simulations of Dimethyl Sulfoxide and Dimethyl Sulfoxide - Water Mixture," *Journal of Physical Chemistry A*, vol. 105, no. 10, pp. 1702–1710, 2001.

[87] N. Zhang, W. Li, C. Chen, J. Zuo, and L. Weng, "Molecular dynamics study on water self-diffusion in aqueous mixtures of methanol, ethylene glycol and glycerol : investigations from the point of view of hydrogen bonding," *Molecular Physics*, vol. 111, no. 7, pp. 939–949, 2013.

[88] A. Ymeti, J. S. Kanger, R. Wijn, P. V. Lambeck, and J. Greve, "Development of a multichannel integrated interferometer immunosensor," *Sensors and Actuators B*, vol. 83, pp. 1–7, 2002.

[89] R. Wijn, G. Besselink, A. Ymeti, R. Heideman, J. Kanger, J. Greve, and P. Lambeck, "Integration of microfluidics with a four-channel integrated optical Young interferometer immunosensor," *Biosensors and Bioelectronics*, vol. 20, no. 7, pp. 1417–1421, 2004.

[90] H. Shao, D. Kumar, S. A. Feld, and K. L. Lear, "Fabrication of a Fabry-Pérot cavity in a microfluidic channel using thermocompressive gold bonding of glass substrates," *Journal of Microelectromechanical Systems*, vol. 14, no. 4, pp. 756–762, 2005.

[91] J. C. T. Eijkel, K. M. van Delft, T. S. Druzhinina, A. van den Berg, H. Rathgen, F. Mugele, N. R. Tas, and D. Mijatovic, "Micromachined Fabry-Pérot Interferometer with Embedded Nanochannels for Nanoscale Fluid Dynamics," *Nano Letters*, vol. 7, no. 2, pp. 345–350, 2006.

[92] C. Dongre, R. Ramponi, H. J. W. M. Hoekstra, P. Watts, R. Osellame, M. Pollnau, Y. Gu, H. H. van den Vlekkert, B. Ngamsom, A. Crespi, and G. Cerullo, "Three-dimensional Mach-Zehnder interferometer in a microfluidic chip for spatially-resolved label-free detection," *Lab on a Chip*, vol. 10, pp. 1167–1173, 2010.

[93] R. Buividas, E. Scheer, G. Gervinskas, D. J. Day, S. Juodkazis, P. Leiderer, and P. Trocha, "Fabry-Pérot sensors: microfluidic channels and transparent membranes," in *Proceedings of SPIE*, S. Juodkazis, Ed., vol. 8204, no. December 2011, 2011, p. 82043Q.

[94] J. Tian, Y. Lu, Q. Zhang, and M. Han, "Microfluidic refractive index sensor based on an all-silica in-line Fabry–Perot interferometer fabricated with microstructured fibers," *Optics Express*, vol. 21, no. 5, pp. 6633–6639, 2013.

[95] D. R. Vogus, V. Mansard, M. V. Rapp, and T. M. Squires, "Measuring concentration fields in microfluidic channels in situ with a Fabry-Perot interferometer," *Lab on a Chip*, vol. 15, no. 7, pp. 1689–1696, 2015. [Online]. Available: http://dx.doi.org/10.1039/C5LC00095E

[96] D. J. Bornhop, J. C. Latham, A. Kussrow, D. A. Markov, R. D. Jones, and H. S. Sørensen, "Free-Solution, Label-Free Molecular Interactions Studied by Back-Scattering Interferometry," *Science*, vol. 317, no. September, pp. 1732–1736, 2007. [Online]. Available: http://www.sciencemag.org/cgi/doi/10.1126/science.1146559

[97] T. M. Jørgensen, S. T. Jepsen, H. S. Sørensen, A. K. Di Gennaro, and S. R. Kristensen, "Back scattering interferometry revisited - A theoretical and experimental investigation," *Sensors and Actuators B: Chemical*, vol. 220, pp. 1328–1337, 2015. [Online]. Available: http://dx.doi.org/10.1016/j.snb.2015.06.121

[98] E. M. Ahmed, "Hydrogel: Preparation, characterization, and applications: A review," *Journal of Advanced Research*, vol. 6, no. 2, pp. 105–121, mar 2015.

[99] S. Rezvani, N. Shi, T. M. Squires, and C. F. Schmidt, "Microfluidic device for chemical and mechanical manipulation of suspended cells," *Journal of Physics D: Applied Physics*, vol. 51, no. 4, pp. 1–9, 2018.

[100] D. Dendukuri, S. S. Gu, D. C. Pregibon, T. A. Hatton, and P. S. Doyle, "Stop-flow lithography in a microfluidic device," *Lab on a Chip*, vol. 7, no. 7, pp. 818–828, 2007.

[101] D. Dendukuri, P. Panda, R. Haghgooie, J. M. Kim, T. A. Hatton, and P. S. Doyle, "Modeling of oxygen-inhibited free radical photopolymerization in a PDMS microfluidic device," *Macromolecules*, vol. 41, no. 22, pp. 8547–8556, 2008.

[102] B. Xia, K. Krutkramelis, and J. Oakey, "Oxygen-Purged Microfluidic Device to Enhance Cell Viability in Photopolymerized PEG Hydrogel Microparticles," *Biomacromolecules*, vol. 17, no. 7, pp. 2459–2465, 2016.

[103] D. Debroy, J. Oakey, and D. Li, "Interfacially-mediated oxygen inhibition for precise and continuous poly(ethylene glycol) diacrylate (PEGDA) particle fabrication," *Journal of Colloid and Interface Science*, vol. 510, pp. 334–344, 2018. [Online]. Available: https://doi.org/10.1016/j.jcis.2017.09.081

[104] "NOA81." [Online]. Available: https://www.norlandprod.com/adhesives/NOA81.html

[105] D. Bartolo, G. Degré, P. Nghe, and V. Studer, "Microfluidic stickers," *Lab on a Chip*, vol. 8, no. 2, pp. 274–279, 2008.

[106] P. Wägli, A. Homsy, and N. F. De Rooij, "Norland optical adhesive (NOA81) microchannels with adjustable surface properties and high chemical resistance against IR-transparent organic solvents," *Procedia Engineering*, vol. 5, pp. 460–463, 2010. [Online]. Available: http://dx.doi.org/10.1016/j.proeng.2010.09.146

[107] S. Silvestrini, D. Ferraro, T. Tóth, M. Pierno, T. Carofiglio, G. Mistura, and M. Maggini, "Tailoring the wetting properties of thiolene microfluidic materials," *Lab on a Chip*, vol. 12, no. 20, pp. 4041–4043, sep 2012.

[108] J. S. Paustian, C. D. Angulo, R. Nery-Azevedo, N. Shi, A. I. Abdel-Fattah, and T. M. Squires, "Direct measurements of colloidal solvophoresis under imposed solvent and solute gradients," *Langmuir*, vol. 31, no. 15, pp. 4402–4410, 2015.

[109] M. Morel, D. Bartolo, J. C. Galas, M. Dahan, and V. Studer, "Microfluidic stickers for cell- and tissue-based assays in microchannels," *Lab on a Chip*, vol. 9, no. 7, pp. 1011–1013, 2009.

[110] "SU-8 2000 Permanent Epoxy Negative Photoresist PROCESSING GUIDELINES FOR: SU-8 2100 and SU-8 2150." [Online]. Available: https://cleanroom.byu.edu/sites/cleanroom.byu.edu/files/pdf/SU-82000DataSheet2100and2150Ver5-1.pdf

[111] P. S. Nunes, P. D. Ohlsson, O. Ordeig, and J. P. Kutter, "Cyclic olefin polymers: emerging materials for lab-on-a-chip applications," *Microfluidics and Nanofluidics*, vol. 9, pp. 145–161, 2010.

[112] "TOPAS COC Polymers | TOPAS." [Online]. Available: https://topas.com/products/topas-coc-polymers

[113] P. M. Van Midwoud, A. Janse, M. T. Merema, G. M. M. Groothuis, and E. Verpoorte, "Comparison of Biocompatibility and Adsorption Properties of Different Plastics for Advanced Microfluidic Cell and Tissue Culture Models," *Analytical Chemistry*, vol. 84, pp. 3938–3944, 2012. [Online]. Available: https://pubs.acs.org/doi/10.1021/ac300771z

[114] M. Berenguel-Alonso, M. Sabés-Alsina, R. Morató, O. Ymbern, L. Rodríguez-Vázquez, O. Talló-Parra, J. Alonso-Chamarro, M. Puyol, and M. López-Béjar, "Rapid Prototyping of a Cyclic Olefin Copolymer Microfluidic Device for Automated Oocyte Culturing." *SLAS technology*, vol. 22, no. 5, pp. 507–517, oct 2017. [Online]. Available: http://www.ncbi.nlm.nih.gov/pubmed/28944724

[115] D. Sun, "Characterization of medical grade poly-dimethylsiloxane as encapsulation materials for implantable microelectromechanical systems," Ph.D. dissertation, Case Western Reserve University, 2014.

[116] "Polyplastics TOPAS 6013F-04 Cyclic Olefin Copolymer (COC)." [Online]. Available: http://www.matweb.com/search/datasheet.aspx?matguid=cccd92518f0d49eeaf5841a1a645795b&ckck=1

[117] S. J. Hwang, M. C. Tseng, J. R. Shu, and H. Her Yu, "Surface modification of cyclic olefin copolymer substrate by oxygen plasma treatment," *Surface and Coatings Technology*, vol. 202, no. 15, pp. 3669–3674, apr 2008.

[118] S. A. Aghvami, A. Opathalage, Z. K. Zhang, M. Ludwig, M. Heymann, M. Norton, N. Wilkins, and S. Fraden, "Rapid prototyping of cyclic olefin copolymer (COC) microfluidic devices," *Sensors and Actuators B: Chemical*, vol. 247, pp. 940–949, 2017. [Online]. Available: http://dx.doi.org/10.1016/j.snb.2017.03.023

[119] D. J. Guckenberger, T. E. De Groot, A. M. Wan, D. J. Beebe, and E. W. Young, "Micromilling: A method for ultra-rapid prototyping of plastic microfluidic devices," *Lab on a Chip*, vol. 15, no. 11, pp. 2364–2378, jun 2015.

[120] S. Roy, C. Y. Yue, Z. Y. Wang, and L. Anand, "Thermal bonding of microfluidic devices: Factors that affect interfacial strength of similar and dissimilar cyclic olefin copolymers," *Sensors and Actuators B: Chemical*, vol. 161, no. 1, pp. 1067–1073, jan 2012.

[121] M. Serra, I. Pereiro, A. Yamada, J. L. Viovy, S. Descroix, and D. Ferraro, "A simple and low-cost chip bonding solution for high pressure, high temperature and biological applications," *Lab on a Chip*, vol. 17, no. 4, pp. 629–634, feb 2017.

[122] N. Keller, T. M. Nargang, M. Runck, F. Kotz, A. Striegel, K. Sachsenheimer, D. Klemm, K. Länge, M. Worgull, C. Richter, D. Helmer, and B. E. Rapp, "Tacky cyclic olefin copolymer: A biocompatible bonding technique for the fabrication of microfluidic channels in COC," *Lab on a Chip*, vol. 16, no. 9, pp. 1561–1564, apr 2016.

[123] "COC elastomer cleared for use in medical, food and pharma applications | PlasticsToday." [Online]. Available: https://www.plasticstoday.com/content/coc-elastomer-cleared-use-medical-food-and-pharma-applications/12783415916506

[124] "TOPAS ELASTOMER E-140: Technical Data Sheet." [Online]. Available: https://topas.com/sites/default/files/TDS_ElastomerE-140_e.pdf

[125] "Harrick Plasma Product Information." [Online]. Available: https://harrickplasma.b-cdn.net/wp-content/uploads/2019/04/Harrick-Plasma-Product-Information-web.pdf

[126] N. Convery and N. Gadegaard, "30 years of microfluidics," *Micro and Nano Engineering*, vol. 2, pp. 76–91, mar 2019.

[127] A. Bertsch and P. Renaud, "Microstereolithography," in *Three-Dimensional Microfabrication Using Two-Photon Polymerization: Fundamentals, Technology, and Applications*. Elsevier Inc., jan 2016, pp. 20–44.

[128] C. Sun, N. Fang, D. M. Wu, and X. Zhang, "Projection micro-stereolithography using digital micro-mirror dynamic mask," *Sensors and Actuators A: Physical*, vol. 121, no. 1, pp. 113–120, 2005.

[129] G. Kaushik, D. A. Gil, E. Torr, E. S. Berge, C. Soref, P. Uhl, G. Fontana, J. Antosiewicz-Bourget, C. Edington, M. P. Schwartz, L. G. Griffith, J. A. Thomson, M. C. Skala, W. T. Daly, and W. L. Murphy, "Quantitative Label-Free Imaging of 3D Vascular Networks Self-Assembled in Synthetic Hydrogels," *Advanced Healthcare Materials*, vol. 8, no. 2, p. 1801186, jan 2019. [Online]. Available: http://doi.wiley.com/10.1002/adhm.201801186

[130] H. He, M. Sofman, A. J. Wang, C. C. Ahrens, W. Wang, L. G. Griffith, and P. T. Hammond, "Engineering Helical Modular Polypeptide-Based Hydrogels as Synthetic Extracellular Matrices for Cell Culture," *Biomacromolecules*, vol. 21, no. 2, pp. 566–580, feb 2020.

[131] A. Brown, H. He, E. Trumper, J. Valdez, P. Hammond, and L. G. Griffith, "Engineering PEG-based hydrogels to foster efficient endothelial network formation in free-swelling and confined microenvironments," *Biomaterials*, vol. 243, p. 119921, jun 2020.

[132] J. L. West and J. A. Hubbell, "Photopolymerized hydrogel materials for drug delivery applications," *Reactive Polymers*, vol. 25, pp. 139–147, jun 1995.

[133] G. Iwona and H. Janik, "Review: Synthetic polymer hydrogels for biomedical application," *Chemistry and Chemical Technology*, vol. 4, no. 4, pp. 297–304, 2010.

[134] C. C. Lin, C. S. Ki, and H. Shih, "Thiol-norbornene photoclick hydrogels for tissue engineering applications," *Journal of Applied Polymer Science*, vol. 132, no. 8, p. 41563, feb 2015.

[135] M. Chen *et al.*, "Stop-flow lithography and its application to graphical encoding," Master's thesis, Massachusetts Institute of Technology, 2015.

[136] N. A. Stocke, X. Zhang, J. Z. Hilt, and J. E. DeRouchey, "Transport in PEG-Based Hydrogels: Role of Water Content at Synthesis and Crosslinker Molecular Weight," *Macromolecular Chemistry and Physics*, vol. 218, no. 3, p. 1600340, feb 2017. [Online]. Available: http://doi.wiley.com/10.1002/macp.201600340

[137] B. D. Fairbanks, M. P. Schwartz, C. N. Bowman, and K. S. Anseth, "Photoinitiated polymerization of PEG-diacrylate with lithium phenyl-2,4,6-trimethylbenzoylphosphinate: polymerization rate and cytocompatibility," *Biomaterials*, vol. 30, no. 35, pp. 6702–6707, 2009. [Online]. Available: http://dx.doi.org/10.1016/j.biomaterials.2009.08.055

[138] N. Fang, C. Sun, and X. Zhang, "Diffusion-limited photopolymerization in scanning micro-stereolithography," *Applied Physics A: Materials Science and Processing*, vol. 79, no. 8, pp. 1839–1842, 2004.

[139] P. F. Jacobs, "Fundamentals of stereolithography," in *1992 International Solid Freeform Fabrication Symposium*, 1992.

[140] A. S. Kewitsch and A. Yariv, "Nonlinear optical properties of photoresists for projection lithography," *Applied Physics Letters*, vol. 68, no. 4, pp. 455–457, 1995.

[141] A. J. Jacobsen, W. Barvosa-Carter, and S. Nutt, "Micro-scale truss structures formed from self-propagating photopolymer waveguides," *Advanced Materials*, vol. 19, no. 22, pp. 3892–3896, 2007.

[142] M. Choi, J. W. Choi, S. Kim, S. Nizamoglu, S. K. Hahn, and S. H. Yun, "Light-guiding hydrogels for cell-based sensing and optogenetic synthesis in vivo," *Nature Photonics*, vol. 7, no. 12, pp. 987–994, 2013.

[143] "Depth of Field Calculator | Nikon's MicroscopyU." [Online]. Available: https://www.microscopyu.com/tutorials/depthoffield

[144] M. V. Santos, M. Sansinena, N. Zaritzky, and J. Chirife, "Assessment of external heat transfer coefficient during oocyte vitrification in liquid and slush nitrogen using numerical simulations to determine cooling rates." *Cryo letters*, vol. 33, no. 1, pp. 31–40, 2012. [Online]. Available: http://www.ncbi.nlm.nih.gov/pubmed/22434120

[145] Y. Li, G. Zhao, S. M. C. Hossain, F. Panhwar, W. Sun, F. Kong, C. Zang, and Z. Jiang, "Measurement of Thermal Conductivities of Two Cryoprotective Agent Solutions for Vitreous Cryopreservation of Organs at the Temperature Range of 77 K–300 K Using a Thermal Sensor Made of Microscale Enamel Copper Wire," *Biopreservation and Biobanking*, vol. 15, no. 3, pp. 228–233, jun 2017. [Online]. Available: http://www.liebertpub.com/doi/10.1089/bio.2016.0047

[146] X. He, E. Y. Park, A. Fowler, M. L. Yarmush, and M. Toner, "Vitrification by ultra-fast cooling at a low concentration of cryoprotectants in a quartz micro-capillary: A study using murine embryonic stem cells," *Cryobiology*, vol. 56, no. 3, pp. 223–232, jun 2008.

[147] "Refractive index of C2H6OS (Dimethyl sulfoxide, DMSO) - Kozma." [Online]. Available: https://refractiveindex.info/?shelf=organic&book=dimethyl_sulfoxide&page=Kozma

[148] "Refractive index of C2H4(OH)2 (Ethylene glycol) - El-Kashef." [Online]. Available: https://refractiveindex.info/?shelf=organic&book=ethylene_glycol&page=El-Kashef

[149] "Sucrose | C12H22O11 - PubChem." [Online]. Available: https://pubchem.ncbi.nlm.nih.gov/compound/Sucrose#section=Refractive-Index

[150] "Refractive index of H2O, D2O (Water, heavy water, ice) - Hale." [Online]. Available: https://refractiveindex.info/?shelf=main&book=H2O&page=Hale

[151] D. Arago and J. Biot, "Refractive properties of binary mixtures," *Mem Acad Fr*, vol. 15, pp. 7–11, 1806.

[152] "SU-8 2000 Permanent Epoxy Negative Photoresist PROCESSING GUIDELINES FOR: SU-8 2000.5, SU-8 2002, SU-8 2005, SU-8 2007, SU-8 2010 and SU-8 2015." [Online]. Available: https://cleanroom.byu.edu/sites/cleanroom.byu.edu/files/pdf/SU-82000DataSheet2000_5thru2015Ver4-2.pdf